Investigation of Parametric Instabilities in Femtosecond Laser-Produced Plasmas

Dissertation

zur Erlangung des akademischen Grades
doctor rerum naturalium (Dr. rer. nat.)

vorgelegt dem Rat der Physikalisch-Astronomischen Fakultät
der Friedrich–Schiller–Universität Jena

von Diplom-Physiker *László Veisz*
geboren am 20. März 1974 in Budapest, Ungarn

Gutachter

1. Prof. Dr. Roland Sauerbrey
2. Prof. Dr. Peter Mulser
3. Prof. Dr. Georg Pretzler

Tag der letzten Rigorosumsprüfung : 1.8.2003

Tag der öffentlichen Verteidigung : 28.8.2003

Contents

Chapter 1

Introduction

Ultrahigh-intensity lasers are fundamental tools in modern physics. Their fast evolution over the last 15 years [1] started with the invention of chirped pulse amplification (CPA) [2]. This technique opened a new window to the investigation of light-matter interactions. The CPA technique made it possible to generate much shorter laser pulses down to the femtosecond regime with laser peak powers reaching the 1–1000 terawatt level. Nowadays the most of the ultrahigh intensity lasers in the world are applying this method. One of these lasers is the Jena 12 TW laser [3]. These lasers can be focussed down to a few micrometers and enormous intensities up to 10^{21} W/cm^2 can be reached. At these intensities the electric field exceeds many times the binding energy of electrons in an atom. After a plasma is formed, the electrons oscillate at relativistic velocities in these fields [4]. The interaction of ultrahigh-intensity laser pulses with plasmas became a central point of the investigations [5]. There is a great variety of applications of these plasmas from particle acceleration, generation of electromagnetic waves to inertial confinement fusion.

There is a large body of work about laser-plasma based electron acceleration [6]. It was suggested originally in underdense plasmas by Tajima and Dawson [7]. One type of these accelerators, the laser wakefield accelerator, is based on the generation of electron plasma waves and the electrostatic fields of these waves accelerates the electrons [7]. The other type is the direct laser acceleration, which is similar to inverse free electron laser. The electrons are transversally oscillating in the self-generated electric and magnetic fields of a plasma channel generated by the self-focused laser pulse. When this betatron oscillation frequency coincides with the Doppler shifted laser frequency, a resonant energy transfer occurs and the electrons gain energy from the laser [8]. The advantage of these accelerators is the small size due to the large static electric fields in plasmas (about 100 GV/m) compared to the rf accelerator fields (less than 100 MV/m). The highest

electron energy observed from plasma electron accelerator is 200 MeV [9]. Hot electrons produced by lasers in dense plasmas on solid targets are also investigated in detail [5, 10]. The plasma waves generated by resonance absorption or the ponderomotive force of the laser can increase the electron energy.

The electron acceleration mechanisms are studied in detail, because most of the applications involve these fast electrons. For example as the fast electrons leave the plasma, large longitudinal static electric fields are generated due to charge separation. Ions can be accelerated in laser produced plasmas by these fields [11, 12, 13]. Another challenging field is the generation of electromagnetic emission in plasmas such as high order harmonics [5, 14] for example from steep plasma surface, EUV radiation from atomic transitions [15, 16] or incoherent x-ray generation [17, 18]. The fast electrons generate bremsstrahlung in material and this can trigger nuclear reactions for example (γ,n) reactions [10, 19] and photo-fission of actinides [20].

An important topic of laser produced plasmas involves inertial confinenement fusion (ICF) [21]. A small capsule including the fuel is irradiated with a short laser, x-ray or ion beam pulse, which ablates the outer layer of the capsule and implodes the inner part generating shock waves. The compression of the target ignites the fuel. A fast ignitor concept was suggested to reduce the energy requirements of ICF [22, 23]. The precompressed fuel is ignited by an additional high power laser. Some new alternative concepts were also proposed such as coronal ignition [24].

Parametric instabilities have an important impact on ICF, laser absorption, hot electron generation and propagation of light in plasmas, therefore, they were investigated in detail [25, 26] in the long pulse regime (> 100 ps). Relevant instabilities involving the decay of the incident laser radiation, are stimulated Raman and Brillouin scattering (SRS and SBS) and two-plasmon decay (TPD). SRS (SBS) in plasmas is the decay of the laser electromagnetic wave into an electron plasma wave (ion acoustic wave) and another electromagnetic wave. TPD is the decay of an electromagnetic wave into two electron plasma waves and takes place in the vicinity of the quarter critical density. These plasma waves can couple with the incident laser light to generate $3\omega_0/2$ radiation, which was studied experimentally [27, 28, 29] and theoretically [30]–[31].

After the introduction of CPA the laser based fusion and especially the fast ignitor concept led to a reinvestigation of some of the instabilities at higher intensities and shorter pulses [32, 33]. Particular attention was paid to SRS of ultrashort laser pulses, because SRS can affect the laser-based electron acceleration as well as drive the self-modulated laser wakefield acceleration [6]. Processes that involve ion acoustic waves are generally

suppressed due to the short time scales. Very little attention was paid to TPD although this instability is often present in fs-laser-plasma experiments. It appears as bright colored light originating from the plasma. Using a Ti:Sapphire laser with 800 nm central wavelength first blue radiation is observed from the plasma, which is the second harmonic radiation. This turns into green radiation as the intensity on target is increased and into white light at the highest intensity. Although, several laboratories made similar observations [34] so far this phenomenon has not yet been analyzed.

The objective of this work is to generate, characterize and explain the origin of three-halves harmonic radiation from femtosecond laser-produced plasmas. Furthermore, it is intended to obtain information about parametric laser-plasma instabilities and to search for possible applications of this emission. The Jena laser without the last amplifier stage, producing 3 TW power was used for the experiments described in this work.

Chapter 2

Theoretical background

When a high intensity laser pulse impinges on solids a great variety of laser matter interactions can take place depending on the laser intensity. At low intensities reversible processes are induced in the material such as the generation of optical and acoustic phonons. At higher intensities irreversible processes are invoked such as nonthermal and thermal melting [35], ablation and the generation of shock waves and plasma. On the 100 femtosecond - 1 picosecond time scale, at higher intensities (above $\sim 10^{13}$ W/cm^2) the dominant process is ionization [36]. The electron shell of the atoms is responsible for binding the atoms into the solid. Therefore after ionization not only the electron is liberated and ejected into vacuum, but the ions will also be freed. This is reinforced by the space charge effect between the electron and the ion. This effect is the so called *Coulomb explosion*. As a result of ionization from the solid a large number of electrons and ions will escape forming a plasma [25, 37]. Due to their origin and the space charge these plasmas are quasi neutral and contain two (or more) components, the ions and the electrons. The particles interact with one another via their electric and magnetic fields.

The two component plasmas form the center of the investigations in this work. The method of description of a two-component plasma will be discussed and the relevant plasma parameters will be defined in the next section.

2.1 Plasma characterization and description

For further discussion some general plasma parameters are defined. The *electron and ion plasma density* are the number of electrons and ions respectively per unit volume, n_e and $n_i = n_e/Z$, where Z is the ionization stage. The dimension of the densities is cm^{-3}. The

electron plasma temperature $T_e = 2E_{\text{kin}}/3$, where E_{kin} is the average kinetic energy of the particles, T_e is typically expressed in keV. The energy of a free particle in one degree of freedom is $T_e/2$ and the number of the degrees of freedom is three. It is connected to the temperature in Kelvin ($\widetilde{T}$) by k_B, the Boltzmann's constant $T_e = k_B\widetilde{T}$. The *electron thermal velocity* is defined as [38]

$$v_e = \sqrt{T_e/m_e} \tag{2.1}$$

where m_e is the electron mass [1]. This definition is valid if $T_e \ll m_e c^2$, where c is the speed of light in vacuum. Using normalized parameters $v_e/c = \sqrt{T_e(\text{keV})/511}$. At 1 keV temperature the electrons have a thermal speed of $\sim 10^7$ m/s, i.e. $v_e/c \approx 0.04$. The ion temperature is denoted T_i and T is the temperature generally without specifying the plasma component, i.e. it can be T_e and T_i also depending on the discussion.

Inserting a charge q into a plasma, the electric field and the potential of this charge will be modified. The plasma electrons shield out the Coulomb potential of the charge as $\phi(r) = q\exp(-r/\lambda_{De})/(4\pi\varepsilon_0 r)$, where r is the distance, $\lambda_{De} = \sqrt{\varepsilon_0 T_e/(e^2 n_e)}$ is the electron *Debye length*, ε_0 is the vacuum permittivity and e is the electron charge. The Debye length is practically the range of the inserted charge, i.e. only particles within a distance of λ_{De} will interact strongly with the charge. The charge is screened for distances longer than λ_{De}. The Debye length has a value of 10 nm at $n_e = 4 \times 10^{20}$ cm^{-3} density and $T_e = 1$ keV temperature. These are relevant parameters in the experiments described later on. If the number of particles in a sphere with a radius of λ_{De} is much higher than one, the average of the microfields inserted by particles in the Debye sphere tends to zero and the plasma behaves collectively. The number of electrons in the Debye sphere is 2600 in the present experiments, which is high enough to consider only the collective behavior of the plasma.

2.1.1 The phase space distribution

The kinetic theory of plasmas will be briefly introduced in this section, which is important to obtain the basic equations of plasma models. The collective regime can be investigated by solving the equation of motion with fields originating from the collective movement of the charges in the plasma. Since these fields vary slowly in space, many particles will have similar trajectories and the situation can be simplified with the introduction of the two-fluid description. This is based on the electron and ion *phase space distribution functions*

---

[1] The kinetic energy of the electron is $E_{\text{kin}} = 3m_e v_e^2/2$ with this definition of the electron thermal velocity. There exist different definitions for v_e, but the electron temperature is always the same.

$f_{e,i}(\mathbf{x}, \mathbf{v}, t)$, which characterize the particle density at given $\mathbf{x}$ and $\mathbf{v}$ as a function of time [2]. The distribution functions can be determined experimentally only in some specific cases, but measurable quantities as the density, the temperature or the pressure are connected to them. The density can be obtained from the distribution function as

$$n_{e,i}(\mathbf{x}, t) = \iiint f_{e,i}(\mathbf{x}, \mathbf{v}, t)d\mathbf{v}. \tag{2.2}$$

The indices e and i for the electrons and ions will now be dropped for simplicity. The first velocity moment [3] of the distribution function is connected to the mean velocity ($\mathbf{u}$),

$$n\mathbf{u} = \iiint \mathbf{v}f(\mathbf{x}, \mathbf{v}, t)d\mathbf{v} \tag{2.3}$$

where the dependencies are not shown. This velocity characterizes the average speed of the fluid at a given position and time. The next moment is connected to the pressure,

$$\hat{P} = m \iiint (\mathbf{v} - \mathbf{u}) \circ (\mathbf{v} - \mathbf{u})f(\mathbf{x}, \mathbf{v}, t)d\mathbf{v} \tag{2.4}$$

where $\hat{P}$ is the pressure tensor. Isotropic plasma will be assumed, i.e. $\hat{P} = \hat{I}p$, where $\hat{I}$ is the unit tensor and p is the scalar pressure. In other words, the viscosity of the plasma is neglected. The plasma temperature can be expressed with the second velocity moment,

$$T_e = \frac{2E_{\text{kin}}}{3} = \frac{m}{3n(\mathbf{x}, t)} \iiint v^2 f(\mathbf{x}, \mathbf{v}, t)d\mathbf{v}. \tag{2.5}$$

Particles are neither created nor destroyed and the collisions are also neglected. From these facts it follows that the phase space distribution function is constant along a trajectory, which can be expressed mathematically by the Vlasov equation [4]:

$$\frac{\partial f}{\partial t} + \mathbf{v}\frac{\partial f}{\partial \mathbf{x}} + \frac{q}{m}\left(\mathbf{E} + \frac{\mathbf{v} \times \mathbf{B}}{c}\right)\frac{\partial f}{\partial \mathbf{v}} = 0 \tag{2.6}$$

where q and m are the electron or ion charge and mass, respectively. This is an equation for noncolliding particles in electric and magnetic fields. The fields depend on the distribution and motion of the particles and therefore they can be determined by the Maxwell equations. That is, the plasma is completely described by the Vlasov and the Maxwell equations. To account for collisions the Vlasov equation must be completed with a collision term on the RHS [25].

---

[2]The probability of finding a particular particle at time t between $\mathbf{x}$ and $\mathbf{x} + d\mathbf{x}$ with a velocity in the range $\mathbf{v}$ and $\mathbf{v} + d\mathbf{v}$ is $f_{e,i}(\mathbf{x}, \mathbf{v}, t)d\mathbf{x}d\mathbf{v}/N_{e,i}$, where $N_{e,i}$ is the number of electrons or ions.

[3]The definition of the zeroth, first and second velocity moments of a scalar function $g(\mathbf{v})$ is $\int g(\mathbf{v})d\mathbf{v}$, $\int \mathbf{v}g(\mathbf{v})d\mathbf{v}$, and $\int \mathbf{v} \circ \mathbf{v}g(\mathbf{v})d\mathbf{v}$, where $a_{ij} = b_i \circ b_j$ is the dyadic product.

[4]This is obtained from the collisionless Boltzmann's equation, which is well known in the kinetic theory of gases [39], by inserting $\dot{\mathbf{x}} = \mathbf{v}$ and $\dot{\mathbf{v}} = F_{Lorentz}/m_{e,i}$

2.1.2　The two-fluid description of the plasma

The basic equations of a collective plasma will now be derived. To obtain equations for the measurable quantities, the velocity moments of the Vlasov equation are taken for electrons and ions also, indices are dropped. The zeroth moment yields the well known *continuity equation*,

$$\frac{\partial n}{\partial t} + \frac{\partial}{\partial \mathbf{x}}(n\mathbf{u}) = 0 \tag{2.7}$$

The first moment is the *force equation* or *fluid equation of motion*,

$$n\left(\frac{\partial \mathbf{u}}{\partial t} + (\mathbf{u}\nabla)\mathbf{u}\right) = \frac{nq}{m}\left(\mathbf{E} + \frac{\mathbf{u}\times\mathbf{B}}{c}\right) - \frac{1}{m}\nabla p. \tag{2.8}$$

As the number of moment equations is infinite, the series must be truncated with an approximation. This is typically done by the second moment that includes the heat flow – proportional to $\sim v^3$. The heat flow is approximated in different parameter regimes leading to various *equations of state*. Plasma collective behavior takes the form of different types of waves, characterized by angular frequency ω – it will be called shortly as frequency – and wavevector $\mathbf{k}$. Depending on the phase velocity compared to the thermal velocity of the media (v_{th}), for electrons Eq. 2.1 and for ions analogous, diverse equation of states must be applied leading to various waves.

When $\omega/k \ll v_{\text{th}}$ the particles have enough time to thermalize the plasma causing a constant temperature and validating the isothermal equation of state

$$p = nT. \tag{2.9}$$

It is clear from Eqs. 2.3, 2.4 and 2.5 that in the case of a plasma with Maxwellian velocity distribution the isothermal equation of state is valid. In the opposite limit $\omega/k \gg v_{\text{th}}$ the particle movement – and so the heat flow – is negligible during the characteristic time of the wave ($\sim 1/\omega$) compared to the wavelength of the actual wave. In this case the adiabatic equation of state is applicable

$$\frac{p}{n^\gamma} = \text{constant} \tag{2.10}$$

where $\gamma = (d+2)/d$ in d dimension, i.e. $\gamma = 5/3$ for plasmas in three-dimension.

The Maxwell equations complete the previous description

$$\nabla \mathbf{E} = \rho/\varepsilon_0 \tag{2.11}$$

$$\nabla \mathbf{B} = 0 \tag{2.12}$$

$$\nabla \times \mathbf{E} = -\frac{\partial \mathbf{B}}{\partial t} \tag{2.13}$$

$$\nabla \times \mathbf{B} = \mu_0 \mathbf{J} + \frac{1}{c^2}\frac{\partial \mathbf{E}}{\partial t} \tag{2.14}$$

where μ_0 is the vacuum permeability and Eqs. 2.11, 2.13 and 2.14 are known as the Poisson, Faraday and Ampere Laws respectively. The connections between the number density defined earlier and the density and current used here are

$$\rho \;=\; \sum_l q_l n_l \tag{2.15}$$

$$\mathbf{J} \;=\; \sum_l n_l q_l \mathbf{u}_l \tag{2.16}$$

where the l index runs over the components of the plasma, i.e. electrons and ions in the present case.

The Eqs. 2.7, 2.8, 2.9 or 2.10, 2.11–2.16 together provide a complete description of the plasma collective behavior. This is the so called *two-fluid description of the plasma.*

A very important classification of plasmas is supplied by the Coulomb coupling parameter $\sim |\langle U_c \rangle| / \langle K \rangle$, where $\langle U_c \rangle$ is the average Coulomb energy and $\langle K \rangle$ is the average kinetic energy. In the case of classical systems the average distance between two particles $\bar{r} \sim n^{-1/3}$ is much larger than the de Broglie wavelength $\Lambda = h/(2\pi\sqrt{mT})$. This condition is most critical for the electrons due to the smaller mass and higher particle density. The previous parameters in the present case ($n_e = 10^{21}$ cm^{-3} and $T_e = 1$ keV) are $\bar{r} \approx 1$ nm and $\Lambda \approx 0.02$ nm confirming that the classical treatment of the plasma is appropriate. The classical coupling parameter is defined as $\Gamma \equiv |\langle U_c \rangle|/T$, where $\langle U_c \rangle = e^2/(4\pi\varepsilon_0 \bar{r})$ is the average Coulomb energy. This coupling parameter characterizes the basic properties of the plasma. If the coupling parameter $\Gamma \ll 1$ the plasma contains weakly interacting quasi-free particles and the Vlasov equation gives a correct description, on the other hand in the $\Gamma \gg 1$ coupling regime the plasma is strongly coupled and the Vlasov equation is not adequate. In fact this classification of plasmas is practically equivalent with the previously used one associated with the number of particles in the Debye sphere ($N_D \sim \Gamma^{-3/2}$). As expected, the coupling parameter $\Gamma \sim 0.01$ at $n_e = 10^{21}$ cm^{-3} and $T_e = 1$ keV.

2.2 Waves in plasmas

An introduction to wave propagation is now presented within the two-fluid description in the absence of large magnetic fields. First the longitudinal electron and ion plasma waves associated with the collective density fluctuations and subsequently the electromagnetic waves will be considered.

2.2.1 Electron plasma waves

Taking high frequency oscillations, the heavy ions are regarded as a homogeneous background with a density of $n_{i0} = n_{e0}/Z$ and the adiabatic equation of state Eq. 2.10 is used for the electrons in one dimension. In addition the continuity (Eq. 2.7) and force (Eq. 2.8) equations are applied for the electron fluid and the Poisson's equation (Eq. 2.11) for the field to establish an equation for the electron density. It is assumed that the mean velocity, pressure, electron density and the electric field deviate from the steady state values only slightly. The equations can be linearized with respect to these deviations – neglecting the second and higher order terms – leading to the wave equation of the electron plasma wave

$$\left(\frac{\partial^2}{\partial t^2} - 3v_e^2\frac{\partial^2}{\partial x^2} + \omega_{pe}^2\right)\widetilde{n} = 0 \tag{2.17}$$

where $\widetilde{n} = n_e - n_{e0}$ is the density perturbation and $\omega_{pe} = \sqrt{e^2 n_{e0}/(\varepsilon_0 m_e)}$ is the electron plasma frequency depending only on the electron density as parameter. Searching the amplitude in the form $\widetilde{n} = \widetilde{n}_0 \exp(i\mathbf{k}_e\mathbf{x} - i\omega_e t)$ where $\widetilde{n}_0$ is slowly varying (normal mode analysis) the *electron plasma wave* dispersion relation [5] is obtained,

$$\omega_e^2 = \omega_{pe}^2 + 3v_e^2 k_e^2 \tag{2.18}$$

This is known as the Bohm-Gross dispersion relation [40]. Sometimes this wave is called *Langmuir wave* and its quantum is the plasmon. Eq. 2.18 is the short wavevector limit of the exact dispersion relation and the dominant term is ω_{pe}^2 with a small thermal correction $3v_e^2 k_e^2$, i.e. $\omega_e \approx \omega_{pe}$. For this reason the electron plasma wave frequency depends dominantly on the electron density in the plasma and weakly on its wavevector and on the temperature. The value of the plasma wave frequency can reach the frequency of the incident radiation at high densities.

2.2.2 Ion-acoustic waves

The low frequency ion-acoustic wave is investigated next. The electron and ion fluids must now be considered together. The one-dimensional problem is treated in the same way as before, but this time for the ions. The force equation for the electrons is rather simplified – the LHS of Eq. 2.8 is neglected. This approximation is valid because the electrons move together with the ions leading to similar mean velocities and densities, but their mass is much smaller. Assuming $v_i \ll \omega/k \ll v_e$, the isothermal equation of

---

[5]The $\omega = \omega(\mathbf{k})$ function, that is the dependence of a wave's frequency on its wavevector is termed generally as *dispersion relation*.

state is used for the electrons and the adiabatic for the ions. As in the previous case the equations are linearized to get the following wave equation

$$\left(\frac{\partial^2}{\partial t^2} - \frac{ZT_e + 3T_i}{m_i}\frac{\partial^2}{\partial x^2}\right)\widetilde{n}_i = 0 \tag{2.19}$$

where m_i is the ion mass and $\widetilde{n}_i$ is the ion density perturbation. The dispersion relation of *ion-acoustic waves* obtained by normal mode analyzing the previous wave equation

$$\omega_i = \pm v_s k_i \tag{2.20}$$

where $v_s = \sqrt{(ZT_e + 3T_i)/m_i}$ is the ion sound velocity, ω_i and k_i are the frequency and wavevector of the ion-acoustic wave. The quantum of an ion-acoustic wave is analogous to a phonon in fluids or solids. As one can see from the dispersion relation, this wave is similar to a sound wave. Consequently, these waves are also known as ion sound waves. The ion-acoustic wave frequency is small compared to the incident light frequency. A damping mechanism exists also for these waves, which is significant if $ZT_e \approx T_i$ as in this case the condition $v_i \ll \omega_i/k_i$ is not fulfilled. The frequency of the wave satisfies the relation: $\omega_i \ll \omega_e \leq \omega_l$, where ω_l is the frequency of the incident light.

The electron plasma and ion-acoustic waves are longitudinal waves caused by electron and ion density oscillations. They are referred to as electrostatic waves, because the electric field is generated purely by charge displacement and not the temporally oscillating magnetic field. Since a clear charge separation is present between electrons and ions, this electric field can be very high for electron plasma waves. It exceeds 1 GV/cm maximal values, providing an ideal medium for various phenomenons such as electron acceleration [6]. The electric field is much smaller for ion-acoustic waves, because there is no large charge separation.

2.2.3   Electromagnetic waves

In laser-plasma interactions a very important issue is the behavior of the incident laser light in the plasma. As the light is a high frequency wave, the ions can again be treated as a neutralizing background. A relation between $\mathbf{J}$ and $\mathbf{E}$ can be established with the linearized force equation – neglecting terms of the order of E^2 such as $(\mathbf{u}\nabla)\mathbf{u}$ and $\mathbf{u} \times \mathbf{B}$. Using this connection, Faraday's and Ampere's equations the following wave or Helmholtz equation is obtained for $\mathbf{E}$

$$\nabla^2\mathbf{E} - \nabla(\nabla\mathbf{E}) + \frac{\omega_0^2}{c^2}\epsilon\mathbf{E} = 0 \tag{2.21}$$

where $\epsilon = 1 - \omega_{pe}^2/\omega_0^2$ is the dielectric function of the plasma [6] and ω_0 (k_0) is the frequency (wave number) of the electromagnetic radiation. Taking the electromagnetic wave in the form $\mathbf{E}_0 e^{i(\mathbf{k}_0\mathbf{x}-\omega_0 t)}$ the dispersion relation in a homogeneous plasma [7] is readily obtained

$$\omega_0^2 = \omega_{pe}^2 + c^2 k^2. \tag{2.22}$$

The quantum of the electromagnetic radiation is the photon. There are important consequences of this dispersion relation. An electromagnetic wave with frequency $\omega_0 < \omega_{pe}$ can not propagate in the plasma, because the characteristic time of the plasma electrons to shield out the field of the light wave is $\sim \omega_{pe}^{-1}$. The electron plasma density at which the plasma frequency equals the frequency of the light is the *critical density*

$$n_c = \omega_0^2 m_e \varepsilon_0/e^2. \tag{2.23}$$

This has a value of 1.7×10^{21} cm^{-3} at $\lambda = 800$ nm laser wavelength. The phase velocity of an electromagnetic wave in plasma is $v_{\mathrm{ph}} = \omega_0/k = c/\sqrt{1 - \omega_{pe}^2/\omega_0^2}$. Consequently, the index of refraction

$$N = \sqrt{1 - \frac{\omega_{pe}^2}{\omega_0^2}} = \sqrt{1 - \frac{n_e}{n_c}} \tag{2.24}$$

is smaller than one. The group velocity of the electromagnetic waves is $v_g = c\sqrt{1 - \omega_{pe}^2/\omega_0^2}$.

For the experiments described in this work it is important to consider electromagnetic wave propagation in an inhomogeneous plasma. Two different cases must be distinguished, depending on whether the characteristic length on which the plasma density changes is longer or shorter than the laser wavelength. This characteristic length is the *electron plasma density scale length*

$$L = \left| n_e \left(\frac{dn_e}{dx} \right)^{-1} \right|_{x_0} \tag{2.25}$$

which is generally taken at the critical density $(x_0 = x_{cr})$. $L \gg \lambda$ is the typical experimental condition for the long laser pulse regime with a FWHM pulse duration in the range 100 ps - 10 ns. On the other hand, a 100 fs laser with a good prepulse and pedestal contrast will not generate preplasma before the arrival of the main pulse and this leads to scale lengths $L \ll \lambda$. Certainly, the plasma will be expanded with short pulse lasers

---

[6]There are two alternative methods to discuss the plasma processes. The first that is applied here, to regard the charged particles as external to the plasma, not part of the matter. In this case $\mathbf{D} = \varepsilon_0\mathbf{E}$ and the material equations Eqs. 2.15 and 2.16 for the density and the current are valid. The other method is to view the particles as internal to the plasma and $\mathbf{D} = \epsilon\varepsilon_0\mathbf{E}$, but $\rho = 0$ and $\mathbf{J} = 0$. The two procedures are equivalent, but they should not be mixed – i.e. here ϵ is not the relation between $\mathbf{D}$ and $\mathbf{E}$.

[7]In a homogeneous plasma $\rho = 0$ (Eq. 2.15) and from Poisson's equation (Eq. 2.11) $\nabla\mathbf{E} = 0$.

also if there are deliberately introduced or internal – due to the amplification process – prepulses.

The long scale length case, $L \gg \lambda$, i.e. the plasma expanded to a size much higher than the laser wavelength. Using Eq. 2.21 with a linear plasma density profile ($n_e = n_c * x/L$) and perpendicular incidence an analytic solution, the well known Airy function, is obtained [25]. After matching the electric field at the vacuum plasma interface and expecting that it does not penetrate into overdense regions (where $n_e > n_c$) with significant amplitudes, the solution is the Airy A function

$$E\left[\left(\frac{\omega_0^2}{c^2 L}\right)^{1/3}(x - L)\right] = 2\sqrt{\pi}\left(\frac{\omega_0 L}{c}\right)^{1/6} E_{\text{vac}} e^{-i\varphi/2} A\left[\left(\frac{\omega_0^2}{c^2 L}\right)^{1/3}(x - L)\right]$$

where E_{vac} is the electric field in vacuum and $\varphi = 4\omega_0 L/(3c) - \pi/2$ is the phase of the wave reflected from the critical density – the first term in φ is due to propagation from vacuum to the critical density and back and the second is the shift caused by reflection. The following important facts follow from this result: (1) light at perpendicular incidence is reflected from the critical density; (2) beyond the critical density the electric field is evanescent in space; (3) the dispersion relation Eq. 2.22 is valid with ω_{pe} taking the local electron plasma frequency value; and (4) the electric field and the wavelength increases as the reflection point is approached according to this dispersion relation.

At oblique incidence and s-polarization – the electric field is perpendicular to the plane of incidence – the wave equation Eq. 2.21 has a similar solution as for perpendicular incidence. The wavevector component perpendicular to the density gradient, $k_y = \omega_0 \sin(\alpha)/c$ is constant during propagation, where α is the angle of incidence in vacuum. In the case of normal incidence the laser penetrates into the plasma and the turning point is at the critical density. For oblique incidence the reflection of light occurs when k_x, the parallel component, becomes zero. This is at lower density, when $\epsilon(x) = \sin^2(\alpha)$, which means $n_e = n_c \cos^2(\alpha)$ at the reflection point. In a plasma with a given density, the angle of refraction β is calculated using the dispersion relation (Eq. 2.22) and keeping the perpendicular component of the wavevector constant.

$$\sin \beta = \frac{\sin \alpha}{\sqrt{\varepsilon}} = \frac{\sin \alpha}{\sqrt{1 - \frac{\omega_{pe}^2}{\omega^2}}} \tag{2.26}$$

where ω is the angular frequency of the light wave. When the light wave is the incident laser $\omega_{pe}^2/\omega_0^2 = n_e/n_c$ is found. Light generated in the plasma will be subject to refraction so its propagation direction will change as it reaches the vacuum.

If the obliquely incident wave is p-polarized – the electric field lies in the plane of incidence – the propagation is similar but the electric field vector has a component per-

pendicular to the plasma surface, which leads to a new absorption mechanism, resonance absorption.

The short scale length case, $L \ll \lambda$, i.e. the light collides with a plasma wall. This situation has been analyzed by different groups [41, 42]. The electric field decays exponentially in the high density plasma as earlier with a skin depth of about c/ω_{pe}, where the local plasma frequency is higher than the laser frequency ($\omega_{pe} > \omega_0$), i.e. the plasma is overdense. The intensity is higher for ultrashort pulses that can create short scale length, than for long ones. Furthermore, the field decreases much faster due to the short scale length at the reflection point. Therefore the light pressure gradient, the so called ponderomotive force becomes much higher than for long scale lengths, in fact it can push the plasma wall inwards. There is an extraordinary absorption of the incident radiation in the p-polarized case, the Brunel mechanism, which is the complementary effect to the resonance absorption.

There are many other types of waves, for example electron-acoustic wave [43], which is also an eigenmode of the nonmagnetized plasma. The dispersion relation of this mode looks similar to that of the ion-acoustic wave ($\omega \sim k$). Whereas, it has 3 - 4 orders of magnitude lower amplitude than electron plasma waves. In magnetized plasmas are numerous types of oscillations as the shear Alfvén or the magnetosonic waves. Nevertheless, the dominant modes in the nonmagnetic laser produced plasmas are discussed, which will be important for the analysis of the experimental results.

2.3   Effects in laser plasma physics

The topics discussed in this chapter include the ionization caused changes on the laser, the effect of light pressure on the plasma, absorption of laser light in the plasma and loss mechanisms of different plasma waves.

2.3.1   Effects of ionization

Even for a solid target, the situation can be similar to a gas target when a very long pedestal is present or a prepulse arrives much earlier than the main laser pulse. This prepulse or pedestal generates a preplasma that expands and depending on the delay time recombines, forming a gas-like medium in front of the solid target. Therefore some effects of high power lasers on a gas will be discussed.

When a high intensity laser pulse propagates in a gas it will ionize the atoms partially or fully. Ionization leads to a continuous change in the electron density during the laser pulse. Since the index of refraction depends on the electron density (Eq. 2.24), various processes are invoked. One important phenomenon is caused by the radial profile of the focused laser beam. Due to the beam profile, typically Gaussian, a similar electron density profile will be generated, i.e. the index of refraction will vary radially as in the case of a defocusing graded-index lens [44]. Since the intensity is maximal along the propagation axis, this will lead to the defocusing of the laser beam, so called *ionization defocusing* first demonstrated by Auguste, *et al.* [45]. Fill [46] described this mechanism and established an equation for the beam radius as a function of the position taking into account refraction and ionization for homogeneous gas. A very important consequence of this defocusing there exists a maximum intensity that can be reached when focusing a high intensity laser in low pressure gas, for example air. This intensity depends strongly on the pressure of the air and takes the value $\sim 10^{18}$ W/cm^2 at 5 mbar pressure. Certainly, this defocusing can also take place in a partially ionized preplasma and could decrease the maximal attainable intensity. It is important to note that not only ionization changes the beam profile but electron mass increase due to relativistic oscillation velocity, also can induce self-focusing [47].

Another important effect is related to the temporal variation of the electron density, i.e. the temporal variation of the index of refraction. Similarly to self-phase modulation in nonlinear optics, the temporal change of the refractive index causes a temporal variation in the phase of the electromagnetic wave, φ. Because the frequency is the temporal derivative of the phase, this temporal evolution of the phase acts as a frequency shift of the radiation [48]

$$\omega_b = \frac{d\varphi}{dt} = \omega_0 + \frac{k_0 s}{2n_c} \frac{dn_e}{dt} \tag{2.27}$$

where ω_b is the (blue) shifted laser frequency, ω_0 and k_0 is the original frequency and wavevector of the laser as before and s is the propagation length in the plasma. Ionization ($dn_e/dt > 0$) generates a blue shift of the spectrum [48] as can be seen from the previous equation. As the blue shift varies during the pulse, interference can appear between the different temporal components and the interference modulates the spectrum. Ionization induced spectral blue shift is accompanied by ionization defocusing, which makes the interpretation more complicated.

2.3.2   Ponderomotive force

If an electromagnetic wave propagates in a plasma, the plasma electrons are oscillating in the electric field and the time-averaged force inserted by the light on the electrons is zero [37]. This picture changes if the light electric field is not homogeneous. Assuming a radially decreasing intensity from the optical axis the transversally oscillating electrons are moving to areas with smaller electric field and will not return to their original position after one oscillation. The electrons will continue this cycle, leading to a lateral movement and a nonzero time-averaged force acting on them. This *ponderomotive force* is found to be

$$F_{\text{Pond}} = -\frac{e^2}{4 m_e \omega_0^2} \nabla \mathbf{E}^2 \tag{2.28}$$

and is directed opposite to the gradient of the intensity for electrons. This force is not always transversal, it can be longitudinal also as the laser pulse has longitudinal gradients. The ponderomotive force density $f_{\text{Pond}} = n_e F_{\text{Pond}} = -n_e m_e \nabla(v_{\text{osc}}^2)/4$, here is

$$v_{\text{osc}} = e E_0/(m_e \omega_0) \tag{2.29}$$

the *oscillation* or *quiver velocity* of an electron in an electromagnetic field with frequency ω_0 and electric field amplitude E_0. The quiver velocity in practical units is $v_{\text{osc}} = \sqrt{I\lambda^2/(1.37 \times 10^{18} \text{ Wcm}^{-2} \mu\text{m}^2)}$. The ponderomotive force density has a similar form to the thermal pressure force $-\nabla p = -\nabla n_e m_e v_e^2$, showing that the light pressure becomes dominant over thermal pressure when $v_{\text{osc}} \sim v_e$. In the case of lasers with 1 μm wavelength this condition is satisfied at about 3×10^{15} W/cm^2 laser intensity [41], so above this intensity the light pressure inhibits plasma expansion. The ponderomotive force is responsible for many effects such as the ponderomotive self-focusing, hole boring and parametric instabilities [42, 47, 49].

The time averaged longitudinal ponderomotive force, i.e. the gradient of the light pressure, can lead to *hole boring* into the overdense plasma at ultrahigh intensities in steep density profiles. The plasma surface move inwards with an intensity dependent velocity. The momentum and number conservation yields for the front, recession or hole boring velocity the following equation [42, 50]

$$\frac{u}{c} = \sqrt{\frac{\Delta p}{p_{\text{tot}}} \frac{n_c}{2 n_e} \frac{Z m_e}{m_i} \frac{I\lambda_\mu}{1.37 \times 10^{18} \text{W/cm}^2}} \tag{2.30}$$

where λ_μ is the wavelength of the laser in μm, $p_{\text{tot}} = 2I/c$ and $\Delta p = (2-a)\cos(\alpha)I/c$ is the transferred momentum density taking account of absorption (a) and angle of incidence (α), which decrease the front velocity. A recession velocity of $0.015c$ has been measured

at 10^{19} W/cm^2 intensity, producing a measurable Doppler shift [50]. The consequences of hole boring besides a curved critical surface are a red shift in the reflected light and increased absorption.

The radial ponderomotive force can expel all electrons within a core radial region leading to a decreased electron density, i.e. *electron cavitation*. That leads to a channel with radially decreasing index of refraction. Due to this channel the tail of the laser pulse will be self-focused [47], this is called *ponderomotive self-focusing*.

2.3.3 Absorption of laser light in plasmas

There are a great number of processes in plasmas that absorb the laser energy, for example the previously discussed plasma waves gain their energy also from the laser. The most important absorption mechanisms that can absorb a significant amount of laser energy are collisional and resonance absorption, Brunel mechanism, and $\mathbf{j} \times \mathbf{B}$ heating [5].

Collisions have been neglected in the previous descriptions of the collective effects. The electrons oscillating in the field of an s-polarized laser can lose their energy in collisions with ions. This means an effective loss for the laser energy. To describe the collisional absorption – also called inverse bremsstrahlung – in the case when a lot of particles are in the Debye sphere, the Vlasov equation must be completed with a collisional term [25]. This term $(\partial f_{ei}/\partial t)_C$ inserted on the RHS of Eq. 2.6 is responsible for the electron-ion collisions, but will not alter the number of particles and so the zeroth moment, i.e. the continuity equation stays unchanged. The first velocity moment of the collision term in the electron and ion plasma can be expressed with averaged quantities $\int \mathbf{v}(\partial f_{ei}/\partial t)_C d\mathbf{v} = (\partial n_e \mathbf{u}_e/\partial t)_i$, where this new form is the change of the electron momentum by collisions with ions. The momentum transfer further simplified $(\partial n_e \mathbf{u}_e/\partial t)_i = \nu_{ei} n_e \mathbf{u}_e$ where ν_{ei} is the electron-ion collision frequency. The *electron-ion collision frequency* expressing the rate of encounters between the two species [25]

$$\nu_{ei} = \frac{1}{3(2\pi)^{3/2}} \frac{Z\omega_{pe}^4}{n_e v_e^3} \ln \Lambda \tag{2.31}$$

where Z is the ionization charge state and $\ln \Lambda = 9N_D/Z$ is the Coulomb logarithm, here Λ the ratio of the maximum and minimum impact parameter in the collisions. It depends weakly on the plasma parameters, therefore the constant value $\ln \Lambda = 8$ will be used. The linearized force equation has a slightly different form $\partial \mathbf{u}_e/\partial t = -e\mathbf{E}/m_e - \nu_{ei}\mathbf{u}_e$ calculated from the first moment with the collision term [8]. The same steps must be applied as before

---

[8]As the electron-ion collisions will decrease the momentum of the electron, this modified form of the fluid equation of motion is expected.

(Eq. 2.21) to obtain the wave equation with collisions. It is not surprising that the new wave equation looks like the Eq. 2.21 assuming $\nu_{ei} \ll \omega_0$, only the dielectric function of the plasma is different

$$\epsilon = 1 - \frac{\omega_{pe}^2}{\omega_0(\omega_0 + i\nu_{ei})}. \tag{2.32}$$

Taking the plane wave solution of Eq. 2.21 with this ϵ gives the dispersion relation

$$\omega_0^2 = k^2 c^2 + \omega_{pe}^2 \left(1 - \frac{i\nu_{ei}}{\omega_0} \right) \tag{2.33}$$

To calculate the temporal energy damping rate (ν) $\omega_0 = \omega_r + i\nu/2$ is substituted yielding

$$\nu = \frac{\omega_{pe}^2}{\omega_r^2} \nu_{ei} \tag{2.34}$$

and ω_r satisfies the usual dispersion relation Eq. 2.22. Note that the spatial absorption coefficient is $k_i = \nu/v_g$, where v_g is the group velocity of the light in the plasma. To calculate the collisional absorption fraction (f_C) the Helmholtz equation (Eq. 2.21) must be solved [51]. This can be done in an inhomogeneous plasma with obliquely incident s-polarized light by determining the spatial absorption coefficient from the dispersion relation and integrating over the path of the light. Using density dependent local quantities the following result is observed for $L \gg \lambda$ and an exponential electron density profile

$$f_C = 1 - \exp\left(-\frac{8\nu_{ei}^* L}{3c} \cos^3(\alpha) \right) \tag{2.35}$$

where ν_{ei}^* is the electron-ion collision frequency at the critical density and α is the angel of incidence in vacuum as before. In the $L \ll \lambda$ limit the Fresnel results for metal surface are obtained [52, 53], where the transmitted wave is absorbed due to the nonzero conductivity.

The electron-electron collisions will thermalize the electrons and make the electron distribution function Maxwellian. This thermalization takes place on a time scale inversely proportional to the electron-electron collision frequency, which at 1 keV electron temperature is typically longer than the pulse duration of ultrashort lasers (100 fs). That is the electrons are heated by the laser, but do not have enough time to thermalize, i.e. their velocity distribution function does not remain Maxwellian. The energy of the electrons is absorbed by inverse bremsstrahlung, whose rate depends on this distribution function. Nonthermal distributions have less slower electrons that dominate the collisional absorption (Eq. 2.31) and lead to a decrease of the collisional absorption rate [54].

The significance of collisional absorption is diminished in high intensity laser-plasma interactions by the following facts: (a) the electron-ion collision frequency decreases rapidly with the intensity when the electron oscillation velocity exceeds its thermal velocity,

$\nu_{ei} \sim 1/(v_e^2 + v_{osc}^2)^{3/2}$, (b) in moderate scale-length plasmas ($L \sim \lambda$) – typical for high intensity lasers – the size of the plasma to propagate through is small and the density is underdense ($\leq n_c$), (c) the electron temperature increases rapidly decreasing the electron-ion collision frequency and switching out the collisional absorption during the most of the interaction. Consequently, above $\sim 10^{15}$ W/cm^2 other absorption mechanisms will dominate over collisional absorption with s-polarized light. In the p-polarized case the absorption has a considerable contribution that will be discussed next.

Resonance absorption is an important process that can couple laser energy to the plasma significantly in the case of p-polarized and obliquely incident waves onto an inhomogeneous plasma [25]. This is a direct generation of an electron plasma wave at the critical density by an electromagnetic wave, which then tunnels from the reflection point to the critical density to fulfil the matching conditions. A longitudinal plasma wave is generated by the light electric field component perpendicular to the plasma surface, which favors large incidence angles. On the other hand the longer the tunnelling distance the lower the electric field amplitude at the critical density, so the mechanism works best at some intermediate incidence angle. The description of resonance absorption differs from the previous for the perpendicular electric field component, because the term $\nabla(\nabla\mathbf{E})$ in the wave equation is not zero [9]. Working in terms of the magnetic field the perpendicular electric field can be expressed as $E_x = B(x)\sin(\alpha)/\epsilon(x)$, which has a resonance at the critical density – where $\epsilon = 0$. Taking the magnetic field at the reflection point as a function of the vacuum electric field and considering its decay beyond the turning point in a linear profile one obtains for the absorbed fraction of the intensity by resonance absorption $f_R = 2.6\zeta^2 \exp(-4\zeta^3/3)$, where $\zeta = (\omega_0 L/c)^{1/3}\sin(\alpha)$. This expression has a maximum absorption about 50% at the angle

$$\sin(\alpha_{ra}) = \frac{0.8}{(2\pi L/\lambda)^{(1/3)}} \tag{2.36}$$

where α_{ra} is the angle of incidence in vacuum at which the resonance absorption maximized. The absorption is sizeable in the $\Delta\alpha_{ra} \sim \alpha_{ra}$ incidence angle range.

Resonance absorption takes place in plasmas when their scale length is longer than the amplitude of the longitudinal oscillations of the electrons in the laser field, $v_{osc}/\omega_0 < L$. When this oscillation amplitude is larger than the scale length, the electrons are pulled away from the resonant point. After a half optical cycle the laser electric field reverses its direction and the accelerated electrons penetrate into the plasma much deeper than

---

[9]The $\nabla(\epsilon\mathbf{E}) = 0$ is deduced from Eqs. 2.7, 2.8, and 2.11 [55], and it is not simply the Poisson equation as discussed in footnote 6. In inhomogeneous plasmas it implies that $\nabla\mathbf{E} \neq 0$ and there is an electrostatic perpendicular field component.

the skin depth of the electromagnetic wave. These electrons are absorbed in the plasma and take a large amount of energy with themselves, which is effectively a loss of the laser energy. This is the *vacuum heating* or *Brunel mechanism* [56]. Vacuum heating becomes dominant over resonance absorption below $L/\lambda \approx 0.1$ [57].

Electrons oscillating in the electric field of the laser also experience the laser's perpendicular magnetic field leading to a longitudinal Lorentz force $\sim \partial v_{\mathrm{osc}}^2 / \partial x (1 - \cos(2\omega_0 t))$. The first part is the well known longitudinal ponderomotive force and the second is a oscillating part of the ponderomotive force, which is averaged out in long scale length plasmas. In steep plasmas and relativistic intensities this oscillating force is high enough to accelerate electrons deeper into the plasma than the skin depth during a half laser period [42, 52]. These electrons, similarly to Brunel effect, absorb energy from the laser. This so called *relativistic* $\mathbf{j} \times \mathbf{B}$ *heating* is most efficient at perpendicular incidence.

It is important to note at the end of this Section that the absorption also depends on the from of the solid target [42, 58]. In the case of a curved target due to for example hole boring the absorption increases with the depth of the hole and can reach 80%.

2.3.4 Damping of plasma waves

In laser-plasma interaction the incident electromagnetic radiation can generate various longitudinal plasma waves. These waves are damped and heat the plasma.

Since electron plasma waves are longitudinal oscillations of electrons, the electron and ion collisions play an important role in the damping. Collisions will turn the coherent oscillation of the electrons into thermal motion, diminishing the energy of the wave. Balancing the loss in the wave energy with change in the electrons kinetic energy, $\nu_e \varepsilon_0 E_0^2 / 2 = \nu_{ei} n_e m_e v_{\mathrm{osc}}^2 / 2$ yields $\nu_e = \nu_{ei} \omega_{pe}^2 / \omega_e^2$, where ν_e is the energy damping rate and v_{osc} is the oscillation velocity in the electric field of the electron plasma wave. This result is similar to that obtained for collisional absorption of light waves with the difference $\omega_e \approx \omega_{pe}$ and therefore $\nu_e \approx \nu_{ei}$. That is electron plasma waves are damped stronger in an underdense plasma than electromagnetic waves. Typically this damping mechanism leads to a threshold for instabilities in the long pulse regime.

Electrons moving parallel with the wave oscillate in its longitudinal electric field. The wave-electron energy exchange is zero if an electron moves slower or faster than the wave's phase velocity. Although, when an electron moves with approximately the same speed as the wave ($v = \omega_e / k_e$), i.e. the electron is in phase with the wave it is exposed to a stationary electric field, therefore the energy exchange is not zero. A slightly slower

electron will gain energy from the wave and a slightly faster will lose energy. Depending on whether there are more slower or faster particles the wave will be damped or amplified. This process called *Landau damping* [39]. Landau damping can be described by the kinetic equation [39] or directly from the equation of motion of the electron and the energy balance [25]. A hint is given about the latter. A small perturbation in the coordinate and speed of an electron around the free streaming quantities due to the plasma electric field is assumed. The damping rate can be obtained by first calculating the change of the energy of a particle moving in an electric field, after that averaging over the possible particle positions and velocities in the wave and at the end using energy conservation between the particles and the wave. The following wave amplitude damping rate is obtained assuming a Maxwellian velocity distribution [25]

$$\gamma_L = \sqrt{\frac{\pi}{8}} \frac{\omega_{pe}^2 \omega_e^2}{k_e^3 v_e^3} \exp\left(-\frac{\omega_e^2}{2 k_e^2 v_e^2}\right) \tag{2.37}$$

where the energy damping rate is $2\gamma_L$. For a Maxwellian distribution this leads to damping, because the number of particles falls exponentially with the velocity. Generally, the sign of the first velocity derivative of the velocity distribution function at ω_e/k_e determines whether there is damping or amplification. Keeping in mind that the wave amplitude is damped as $\exp(-\gamma_L t)$, the exponential function in the damping rate makes it a very strong function of the exponent. Practically, the damping is negligible when the exponential part is smaller than 0.01, that is $3v_e \leq \omega_e/k_e$ or equivalently $k_e \lambda_{De} \leq 0.3$, if the phase velocity is lower there are enough electrons with about ω_e/k_e velocity to damp the wave.

For ultrahigh intensity lasers the generated electron plasma waves can reach very large amplitudes. The linear theory applied for Landau damping with the small perturbative expansion in these waves is then no longer valid. Not only electrons with approximately ω_e/k_e velocity can interact with the wave, because the large electric field accelerates during a half period of the electron plasma wave slower particles to the phase velocity also. The larger the velocity range of interacting electrons, the faster the damping of the wave. The electrons run with the plasma wave and are fixed in a potential well of this wave, i.e. are *trapped*. When the oscillation velocity of the electrons in the plasma field reaches the phase velocity, $eE_e/(m_e\omega_e) \approx \omega_e/k_e$ initially cold electrons are also brought into resonance and a strong nonlinear damping is evolved. The absorption of the wave takes place on the same time scale as the time of period of this wave, i.e. the wave amplitude is decreased radically within a few periods [59]. This leads to the loss of periodicity in at least one macroscopically observable quantity (for example electron density or longitudinal electric field), which is called *wavebreaking* [60] and can be expected at amplitudes $eE_e/(m_e\omega_{pe}v_{ph}) \approx 1$. Thermal corrections reduce this amplitude. Wavebreaking can play an important role in ultrashort pulse generated instabilities as a saturation mechanism.

Chapter 3

Parametric instabilities and $3\,\omega_0/2$ generation

The generations of different plasma waves are essential processes in laser plasma physics. Resonance absorption was already discussed. Other important kinds are parametric instabilities [37, 61]. First the general description of parametric instabilities and a physical picture will be given. After that some particular cases will be discussed as SRS and TPD that are relevant for this work and the generation of $3\,\omega_0/2$ radiation.

3.1 General considerations

An *instability* is a process in which a pump produces in the first linear stage exponentially growing daughter waves in time – in some cases in space. Parametric instability is a wave amplification due to the periodic variation of a "parameter"that characterizes the oscillation. The source or pump is typically the laser light, but it can also be a plasma wave. The daughter waves can be electromagnetic as well as plasma waves. Phase and frequency matching must be satisfied in the process. An instability starts generally when the amplitude of the source exceeds a threshold value and grows with a rate dependent on this amplitude. Certainly, the exponential growth does not last long before saturation appears. There are various saturation mechanisms, but typically pump depletion is not important because the conversion from the incident laser energy is moderate.

At first a single-mode parametric instability will be considered – the pump generates one type of oscillation – and the wavevectors will be neglected. It is described by the

equation

$$\frac{d^2}{dt^2}X(t) + 2\Gamma\frac{d}{dt}X(t) + \Omega^2 X(t) = 0 \tag{3.1}$$

where Γ is the damping, Ω is the frequency and $X(t)$ is the amplitude of the oscillation. The frequency can be written $\Omega^2 = \Omega_0^2 (1 - 2\varrho\cos(\omega_{\mathrm{f}}t))$ for a forced oscillator, where Ω_0 is the natural frequency of the oscillation and ϱ and ω_{f} is the amplitude and frequency of the modulating pump with sinusoidal variation. A small damping and pump perturbation is assumed, $\Gamma \ll \Omega_0$ and $\varrho \ll 1$, so the terms containing Γ^2 are neglected. The influence of the pump is contained in the temporally dependent frequency, Ω. In practice the variation of the frequency is achieved by periodically changing a physical parameter that determines the natural frequency. The parametric name originates from here. After Fourier transformation

$$D(\omega)X(\omega) = \varrho\Omega_0^2 \left[X(\omega - \omega_{\mathrm{f}}) + X(\omega + \omega_{\mathrm{f}}) \right] \tag{3.2}$$

and $D(\omega) = -\omega^2 - 2i\Gamma\omega + \Omega_0^2$ supplying the dispersion relation without pump. A very important issue of the previous equation is the coupling of $X(\omega)$ with $X(\omega - \omega_{\mathrm{f}})$ and $X(\omega + \omega_{\mathrm{f}})$ due to the pump. Parametric amplification takes place when two of the involved modes $[X(\omega)$ and $X(\omega \pm \omega_{\mathrm{f}})]$ are natural modes, i.e. having Ω_0 frequency, as can be seen from Eq. 3.2. There are two possibilities to satisfy this: (a) $\omega_{\mathrm{f}} \approx 2\Omega_0$ and (b) $\omega_{\mathrm{f}} \approx \Omega_0$, which correspond to the frequency matching condition. In case (a) from Eq. 3.2 for $X(\omega)$ and $X(\omega - \omega_{\mathrm{f}})$ the *dispersion relation of the parametric instability* can be deduced

$$D(\omega)D(\omega - \omega_{\mathrm{f}}) = \varrho^2\Omega_0^4 \tag{3.3}$$

where the nonresonant $X(\omega + \omega_{\mathrm{f}})$ and $X(\omega - 2\omega_{\mathrm{f}})$ are neglected. The solution of this equation provides $\omega = \omega_{\mathrm{real}} + i\gamma$, which describes X temporally. The γ quantity is the growth rate and characterizes the instability. Waves with maximal growth rate, i.e. maximal amplitude dominate the process and determine its properties. If the detuning is large $(\Delta = \omega_{\mathrm{f}} - 2\Omega_0 \geq \varrho\Omega_0)$ an exponentially decreasing solution is obtained according to the damping, $X(t) \sim \exp(-\Gamma t)$ as expected without pumping. If the detuning is small the amplitude becomes unstable as $X(t) \sim \exp(\gamma t - i\omega_{\mathrm{f}}t/2)$, where $\gamma = \sqrt{\varrho^2\Omega_0^2 - \Delta^2}/2 - \Gamma$ is the temporal growth rate. It should be noted that the mode oscillates at a frequency $\omega_{\mathrm{f}}/2$ independently from its natural frequency, but if the detuning is not zero this will diminish the growth rate. To produce unstable oscillations the pump must have a threshold amplitude depending on the damping – and on Δ in detuned instance. In case (b) the $X(\Omega_0)$ and $X(-\Omega_0)$ are coupled via $X(0)$. A different instability dispersion relation holds, but similarly to case (a) a damped and an unstable solution is obtained. In distinctions to the (a) instable solution there is no growth at zero detuning and the three oscillations are

growing at three different frequencies, $\sim 0, \pm\omega_{\mathrm{f}}$. An example for single-mode parametric instability is a child's swing or a pendulum with periodically varying length. If the length of the swing or pendulum changes with twice the natural frequency of the swing, parametric instability occurs.

When the two modes that couple are different, i.e. have unequal natural frequency and damping rate, the process is the coupled-mode parametric instability. Similarly to Eq. 3.1, the modes are characterized without pump with different equations

$$\mathcal{D}_1 X(t) = \frac{d^2}{dt^2}X(t) + 2\Gamma_1\frac{d}{dt}X(t) + \omega_1^2 X(t) = 0 \qquad (3.4)$$

$$\mathcal{D}_2 Y(t) = \frac{d^2}{dt^2}Y(t) + 2\Gamma_2\frac{d}{dt}Y(t) + \omega_2^2 Y(t) = 0 \qquad (3.5)$$

where $\omega_{1,2}$ are the natural frequencies and $\Gamma_{1,2}$ are the damping rates, $X(t)$ and $Y(t)$ are the amplitudes of the oscillations. In the presence of a pump in the form $Z(t) = Z_0\cos(\omega_0 t)$ the coupled equations are

$$\mathcal{D}_1 X(t) = \varrho_{12}Z(t)Y(t) \qquad (3.6)$$

$$\mathcal{D}_2 Y(t) = \varrho_{21}Z(t)X(t) \qquad (3.7)$$

where ϱ_{12} and ϱ_{21} are the small coupling constants, $\varrho_{12}\varrho_{21}Z_0^2 \ll 1$. In these equations the source of X is the modulated $Y(t)$ by $Z(t)$ and for $Y(t)$ is the modulated $X(t)$. This is best seen by the Fourier transformed equations

$$D_1(\omega)X(\omega) = \varrho_{12}Z_0\left[Y(\omega - \omega_0) + Y(\omega + \omega_0)\right] \qquad (3.8)$$

$$D_2(\omega \pm \omega_0)Y(\omega \pm \omega_0) = \varrho_{21}Z_0\left[X(\omega) + X(\omega \pm 2\omega_0)\right] \qquad (3.9)$$

where $D_j(\omega) = -\omega^2 - 2i\Gamma_j\omega + \omega_j^2$ gives the dispersion relation of the waves without the pump $j = 1, 2$. There is resonant energy transfer – *resonant instability* – when these modes are natural oscillations, which implies

$$\omega_0 = \omega_1 + \omega_2. \qquad (3.10)$$

Neglecting $X(\omega \pm 2\omega_0)$ as off-resonant, i.e. $\omega \pm 2\omega_0$ is not a natural frequency, the instability dispersion relation

$$1 = \frac{\varrho_{12}\varrho_{21}Z_0^2}{D_1(\omega)}\left[\frac{1}{D_2(\omega + \omega_0)} + \frac{1}{D_2(\omega - \omega_0)}\right] \qquad (3.11)$$

for instability two from the previous three D must be zero. There are two types of solutions as for single-mode instabilities. For the first solution $\Re e(\omega) = 0$ leading to purely growing mode instability. It contains a zero frequency wave and two high frequency oscillations

with the frequency of the pump. The second solution corresponds to the decay instability. The pump decays into two daughter oscillations and both of them grow with the same growth rate. The threshold pump value vanishes if one of the damping rates Γ_1 and Γ_2 is zero. A more detailed analysis of this model problem leads to complicated results so only the differences to the previous discussion are emphasized.

Taking a finite wavevector the following points change: the "dispersion relation" $D(\omega)$ depends also on the wavevector $D(\omega, \mathbf{k})$; $\omega_j = \omega_j(\mathbf{k}_j)$ and $\Gamma_j = \Gamma_j(\mathbf{k}_j)$, that is the natural frequency and the damping rate become dependent on the wavevector also, for example see Eq. 2.33; similarly to the frequency matching the wavevector conservation is also fulfilled; generally for the first solution there is no purely growing mode solution; and in some cases only quasi modes are generated, which have different frequency than that from the dispersion relation.

In practice the spatial extent of a plasma wave is finite due to for example inhomogeneity, providing a new classification of instabilities. There are two types of spatially localized instabilities depending on their long-time behavior: absolute and convective. If the amplitudes of the generated waves in a parametric instability are growing in time and approach infinity at a given point in space without including the saturation effects, then the instability is labelled *absolute*. When these amplitudes in a given point eventually become zero, the instability is labelled *convective*. This type of instability is called convective, because the locally excited and growing wave packets propagate and pass through every point in space and only during a limited time period is the generated wave amplitude higher than the thermal background at a given point in the space. Consequently, there is only a spatial amplification of the daughter waves. Absolute instabilities are growing exponentially in time as $\exp(\gamma t)$ before they reach saturation.

An important remark is that the frequency of the daughter oscillations in general are ω and $\omega_0 \pm \omega$ according to the Stokes and anti-Stokes modes, correspondingly their wavevectors are $\mathbf{k}$ and $\mathbf{k}_0 \pm \mathbf{k}$. These frequencies satisfy the frequency and phase matching conditions or energy and momentum conservation and the daughter waves have maximal amplitude when their frequency coincide with the natural frequencies, but if they did not coincide the instability process can occur with a reduced growth and the conservation laws are satisfied with the real frequencies and not the natural ones. This *nonresonant* process is sizeable only at frequencies very near to the natural values.

The decay instability can be treated as an absorption of a pump or source quantum – for example a laser photon – and the simultaneous generation of one-one quantum from each daughter wave – for example another photon and a plasmon – in the quantum picture.
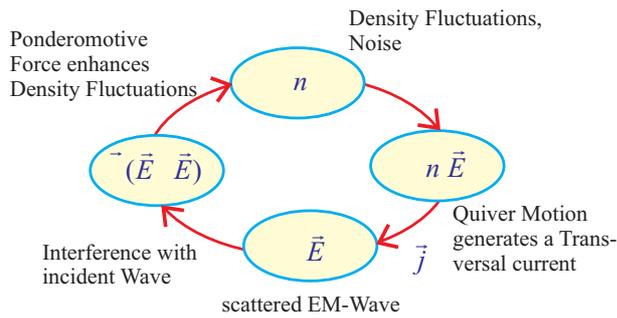
Figure 3.1: Scheme of the stimulated Raman scattering.

Now the generation of an instability in a particular situation, the stimulated Raman scattering, will be analyzed. The scheme of this process is depicted in Fig. 3.1. As mentioned, instabilities are growing exponentially from initial noise, which is provided for example by thermal fluctuations [1]. Assuming an electron plasma wave with small amplitude and a large amplitude laser light in a homogeneous ion background plasma. The electrons in the plasma oscillate in the field of the laser and therefore generate a transversal current that emit dipole radiation. These dipole radiations from various electrons add together and generate scattered light. Consequently, the properties of scattered emission as amplitude and propagation direction depend on the electron plasma wave, for example it moves in the direction of the laser and causes a phase velocity higher than the speed of the light in vacuum without plasma wave. The scattered radiation beats with the incident laser light and produces a standing wave pattern, which moves with the electron plasma wave. The standing wave pattern and the plasma wave are dephased by $\pi/2$ causing a resonance. Density rarefaction occurs at the low density points of the electron plasma wave due to the ponderomotive force and a density maximum is created at the high density points, thus the ponderomotive force further increases the plasma wave amplitude [49]. The increased electron wave amplitude generates more scattered radiation, which inserts larger ponderomotive force. This leads to an amplification cycle and exponential growth of the scattered and electron plasma wave amplitude. Nonlinear effects limit the achievable amplitude [2]. In the case of two-plasmon decay instability the beating of the p polarized laser field and the longitudinal electric field of the plasma waves generates a standing wave pattern and the associated ponderomotive force acts to enhance the plasma wave amplitudes [49]. The transversal currents from the electron oscillation and the dipole radiations cancels after superposition from the two plasma waves and the remaining part is the same as in a homogeneous plasma without plasma waves. The remaining transversal current generates a forward scattered emission, which adds up with the laser light to

---

[1]There will be generally some nonzero amplitude at any $\mathbf{k}_e$ after Fourier transforming spatially the electron density with thermal fluctuations.

[2]Saturation mechanisms generally limit the electron plasma wave and not the scattered wave amplitude.

satisfy its dispersion relation.

The key point in the laser-plasma instabilities is the variation of the electron density or the electron and ion density due to the ponderomotive force. A sinusoidal plasma wave changes the local density and thus the local plasma frequency, which is a periodic variation of the natural frequency of the other plasma waves. That is, the density is the parameter in laser-plasma parametric instabilities that controls the process.

3.2 Two-plasmon decay

The most relevant instability for this work is the two-plasmon decay (TPD), therefore a detailed analysis follows. First the description of TPD will be given in homogeneous plasmas. After that the instability in an inhomogeneous plasma will be discussed. In TPD the laser light decays resonantly into two electron plasma waves, or in quantum picture a laser photon decays into two plasmons as it was first theoretically suggested by Goldman [62]. The generated electron plasma waves are sources of hot electrons [27, 63, 64]. It can be shown that TPD is an absolute instability [30].

The TPD process must fulfil the frequency and phase matching conditions, i.e. the energy and momentum conservations

$$\omega_0 = \omega_{e_1} + \omega_{e_2}, \qquad \mathbf{k}_0 = \mathbf{k}_{e_1} + \mathbf{k}_{e_2} \tag{3.12}$$

where ω_0, $\mathbf{k}_0$ and ω_{e_i}, $\mathbf{k}_{e_i}$ $(i = 1, 2)$ are the frequency and wavevector of the laser light and the electron plasma waves in the plasma, respectively. Generally, the wavevector of the electron plasma waves are not parallel with the laser's wavevector therefore TPD is a two-dimensional instability and one-dimensional (1D) simulation codes for example a 1D particle-in-cell code cannot model it.

The description of this parametric instability aims the determination of the complex frequency of the plasma waves, i.e. not only the (real) frequency that can be obtained from Eqs. 3.12 in resonant case, but the complex part also, that is the growth rate. As $\omega_e \approx \omega_{pe}$ from the frequency matching follows that TPD takes place at the quarter critical density.

The TPD growth rate in a homogeneous plasma will be calculated [25]. The ions are treated as a homogeneous neutralizing background due to the high frequency waves and the plasma wave damping mechanisms are neglected. The quiver velocity is separated from the electron velocity $\mathbf{u}_e = \mathbf{v}_{\mathrm{osc}} + \widetilde{\mathbf{u}}_e$, similarly the background plasma density from the electron plasma density $n_e = n_0 + \widetilde{n}_e$ and the adiabatic equation of state is used for

the electron fluid [3]. Linearizing the continuity (Eq. 2.7) and the force equations (Eq. 2.8) for the electrons with respect to the small quantities $\widetilde{n}_e$ and $\widetilde{\mathbf{u}}_e$

$$\frac{\partial \widetilde{n}_e}{\partial t} + n_0 \nabla \widetilde{\mathbf{u}}_e + \mathbf{v}_{\text{osc}} \nabla \widetilde{n}_e = 0 \tag{3.13}$$

$$\frac{\partial \widetilde{\mathbf{u}}_e}{\partial t} = \frac{e}{m_e} \nabla \widetilde{\phi} - \frac{3v_e^2}{n_0} \nabla \widetilde{n}_e - \nabla(\mathbf{v}_{\text{osc}} \widetilde{\mathbf{u}}_e) \tag{3.14}$$

where $\mathbf{v}_{\text{osc}} = e\mathbf{t}E_0/(m_e\omega_0)$ is the quiver velocity as before, the laser electric field is $\mathbf{E}_0 = \mathbf{t}E_0 \cos(\mathbf{k}_0\mathbf{x} - \omega_0 t)$ showing in the transversal direction of the unit vector $\mathbf{t}$ (satisfying $\mathbf{t}\mathbf{k}_0 = 0$) and $\widetilde{\phi}$ is the electrostatic potential. The electric field of the electron plasma wave is $\mathbf{E} = -\nabla\widetilde{\phi}$, which is assumed to be small enough to neglect nonlinear processes. This is also labelled as *the linear theory* due to the previous linearized approach. Using Poisson's equation (Eq. 2.11) for the potential $\triangle\widetilde{\phi} = e\widetilde{n}_e/\varepsilon_0$, Eqs. 3.13, 3.14 and Fourier transforming the result

$$(-\omega^2 + \omega_{pe}^2 + 3v_e^2 k_e^2)\widetilde{n}_e(\omega;\mathbf{k}) + \frac{\omega}{2}\mathbf{k}_e\mathbf{v}_{\text{osc}}(\widetilde{n}_{e+} + \widetilde{n}_{e-}) + \frac{n_0 k^2}{2}\mathbf{v}_{\text{osc}}(\widetilde{\mathbf{u}}_{e+} + \widetilde{\mathbf{u}}_{e-}) = 0 \tag{3.15}$$

where $\widetilde{n}_{e\pm} = \widetilde{n}_e(\omega \pm \omega_0;\mathbf{k} \pm \mathbf{k}_0)$ and $\widetilde{\mathbf{u}}_{e\pm} = \widetilde{\mathbf{u}}_e(\omega \pm \omega_0;\mathbf{k} \pm \mathbf{k}_0)$. The electron velocity can be expressed from the continuity equation as $\widetilde{\mathbf{u}}_e = (\mathbf{k}/k^2)\omega\widetilde{n}_e/n_0$, if terms containing v_{osc}/c were neglected. Applying this equation together with Eq. 3.15 for $\widetilde{n}_e(\omega)$ and $\widetilde{n}_e(\omega - \omega_0)$ and ignoring nonresonant terms at $\omega + \omega_0$ and $\omega - 2\omega_0$ the following TPD instability dispersion relation is obtained

$$\left(\omega^2 - \omega_{pe}^2 - 3v_e^2 k_e^2\right)\left((\omega - \omega_0)^2 - \omega_{pe}^2 - 3v_e^2(\mathbf{k}_e - \mathbf{k}_0)^2\right)$$
$$= \left[\frac{\mathbf{k}_e\mathbf{v}_{\text{osc}}}{2}\omega_{pe}\frac{(\mathbf{k}_e - \mathbf{k}_0)^2 - k_e^2}{k_e|\mathbf{k}_e - \mathbf{k}_0|}\right]^2 \tag{3.16}$$

where $\omega = \omega_{\text{real}} + i\gamma_0$ here ω_{real} is the frequency of the plasma wave in the resonant case $\omega_{\text{real}} = \omega_e$, and γ_0 is the growth rate in a homogeneous plasma. This equation can be rewritten with the notations $D \equiv \omega^2 - \omega_{pe}^2 - 3v_e^2 k_e^2$ and $D_- \equiv (\omega - \omega_0)^2 - \omega_{pe}^2 - 3v_e^2(\mathbf{k}_e - \mathbf{k}_0)^2$ as $DD_- = E_0^2 f(\mathbf{k})$, which is similar to Eq.3.3. There is no deeper analogy between the general single-mode parametric instability and the TPD, because the wavevector was neglected and TPD does not exists in this case – the growth rate is zero. Assuming $\gamma_0 \ll \omega_e$ the dispersion relation yields the growth rate

$$\gamma_0 = \frac{\mathbf{k}_e\mathbf{v}_{\text{osc}}}{4}\left|\frac{(\mathbf{k}_e - \mathbf{k}_0)^2 - k_e^2}{k_e|\mathbf{k}_e - \mathbf{k}_0|}\right|. \tag{3.17}$$

The value and properties of the maximum growth rate is important to describe the instability as discussed. A plasmon wavevector component perpendicular to the $\mathbf{v}_{\text{osc}}$ and $\mathbf{k}_0$

---

[3]The 1D adiabatic equation of state $p_e/n_e^3 = p_0/n_0^3$, where $p_e = p_0 + \widetilde{p}$ and p_0, n_0 are the unperturbed quantities in a homogeneous plasma, satisfying $p_0 = n_0 m_e v_e^2$. Combining and linearizing these equations $\widetilde{p} = 3\widetilde{n}_e m_e v_e^2$.

plane will appear only in the denominator of Eq. 3.17 thus diminishing the growth rate. Therefore the case is investigated where $\mathbf{k}_e$ is in the plane of $\mathbf{v}_{\mathrm{osc}}$ and $\mathbf{k}_0$. The wavevectors of the plasmons having the maximum of this homogeneous TPD growth rate lie on the *maximum growth rate hyperbola*

$$k_{ey}^2 = k_{ex}(k_{ex} - k_0) \tag{3.18}$$

here the x direction is parallel to the wavevector of the laser. It can be obtained by searching the maximum of γ_0^2 as a function of k_{ey}^2. This hyperbola and the wavevectors of the fastest growing plasmons point in the 45° direction between $\mathbf{v}_{\mathrm{osc}}$ and $\mathbf{k}_0$ for large k_e's. The value of the maximum growth rate along this hyperbola is $\gamma_{\max} = k_0 v_{\mathrm{osc}}/4$. Alternatively, Eq. 3.16 must be solved numerically for the complex ω. The numerical solution has its maximum also along the hyperbola, but the maximum decreases with an increasing plasmon wavevector component perpendicular to $\mathbf{k}_0$ (k_{ey} in the following discussion) as shown in Fig. 3.2, where the electron density depends on the wavevector of the plasmon and is calculated by energy conservation and dispersion relation of the plasma waves.
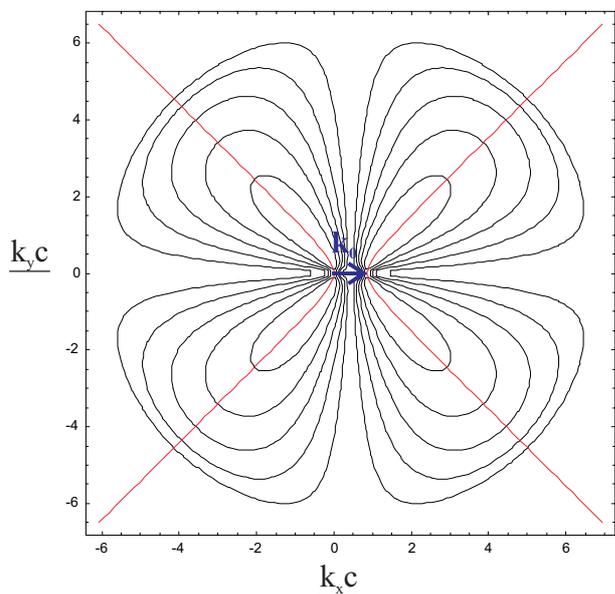
Figure 3.2: The homogeneous TPD growth rate as a function of the plasmon wavevector, obtained by numerically solving Eq. 3.16 at a laser intensity of 7×10^{16} W/cm^2. Landau damping is not included. The laser wavevector at the quarter critical density ($\mathbf{k}_0$) is also plotted as a blue arrow. The red curve is the maximum growth rate hyperbola.

There are several publications on the growth rate of TPD in an inhomogeneous plasma [30, 65, 66, 67]. Using the same equations as in the homogeneous case, but for a linear density profile the problem can be transformed to the form of the Schrödinger equation. The details are in the literature. This Schrödinger equation is solved in a perturbation expansion in powers of L^{-1}. Consequently, these results are valid in long electron density scale length plasmas ($L \gg 10\mu m$), a condition that is strictly speaking not always fulfilled in our experimental situations. Nevertheless, it is instructive to summarize the important

points and deduce the physical consequences. The aim of the theories is to calculate the maximum growth rate in the k space at given plasma parameters and the plasma wavevector at which this maximum is reached. Due to the homogeneous results this wave vector lies on the maximum growth rate hyperbola. This determines the x component of the plasmon wavevector, so the growth rate is only a function of the y component. Originally Liu and Rosenbluth [65] calculated the growth rate of TPD for an arbitrary k_e value in an inhomogeneous plasma using an elegant method based on the Fourier transformed quantities. They determined the growth rate along the maximum growth rate hyperbola as a function of k_{ey} for perpendicular incidence, i.e. expanded the previous homogeneous growth rate with an inhomogeneous part. They derived the correct form of the inhomogeneous part, only the homogeneous portion was oversimplified. As the inhomogeneous part reduces the growth rate for small k_{ey} values (see Eq. 3.23), there is no upper limit for the plasmon wavevector at the maximal growth rate on the hyperbola. This was noticed and corrected by Lasinski and Langdon [66]. In their work they performed numerical simulations and used them to correct the homogeneous growth rate by a term proportional to $-k_{ey}$ [4]

$$\widehat{\gamma}(k_{ey}) = \frac{k_0 v_{\text{osc}}}{4} \left(1 - 10.32 \frac{k_{ey} v_e^2}{v_{\text{osc}} \omega_0} \right) - \frac{\omega_0}{8 k_{ey} L} \tag{3.19}$$

where the $\widehat{\gamma}$ labels a simplified growth rate from the work of Lasinski and Langdon. This expression has a maximum growth rate value

$$\widehat{\gamma}_{\text{max}} = \frac{k_0 v_{\text{osc}}}{4} - \sqrt{\frac{0.65 k_0 v_e^2}{L}}. \tag{3.20}$$

The threshold of the TPD instability is reached when the maximum growth rate reaches zero. Using Langdon's result the threshold condition is

$$\frac{v_{\text{osc}}^2}{4 v_e^2} k_0 L = 0.0504 \frac{L_\mu \lambda_\mu I_{14}}{T_{\text{keV}}} > 2.6 \tag{3.21}$$

where $I_{14} = I/(10^{14} \text{ W/cm}^2)$, T_{keV} is the electron temperature in keV, i.e. $T_e(\text{keV})$ and λ_μ is the laser wavelength in μm. This model gives a maximum growth already at finite k_y, but the problem is that the new homogeneous part does not reflect the space reversal symmetry of the equations for k_{ey} [30]. A correct form of the growth rate was first calculated by Simon *et al.* [67] with the same technique as applied in [65]. They calculated and simulated the growth rate and the TPD threshold condition in different

---

[4]In their original report Lasinski and Langdon made a calculation error and used an unusual definition for the scale length, which is a factor of 4 smaller than the definition used here.

parameter regimes. Simon defined the parameter [5]

$$\beta_S \equiv \frac{36 v_e^4 k_0^2}{v_{\text{osc}}^2 \omega_0^2} = \frac{1.43 T_{\text{keV}}^2}{I_{14} \lambda_\mu^2} \tag{3.22}$$

The typical plasma parameters in the applied experiments in this work were $T_e = 1$ keV, $\lambda = 0.8$ μm and $I > 10^{15}$ W/cm^2 giving $\beta_S < 0.22$. Therefore, the parameter range $\beta_S \ll 1$ and $k_{ey} \sim k_0$ will be discussed here. The results with other parameters are in Ref. [67]. They obtained the TPD growth rate in inhomogeneous plasmas with linear density profile for perpendicular incidence as a function of k_{ey} along the maximum growth rate hyperbola (which determines k_{ex}),

$$\gamma(k_{ey}) = \frac{k_0 v_{\text{osc}}}{4} - \frac{18 v_e^4 k_0 k_{ey}^2}{v_{\text{osc}} \omega_0^2} - \frac{\omega_0}{8 k_{ey} L}. \tag{3.23}$$

This has a maximum value

$$\gamma_{\max} = \frac{k_0 v_{\text{osc}}}{4} - \left(\frac{243 v_e^4 k_0}{128 v_{\text{osc}} L^2} \right)^{1/3} \tag{3.24}$$

or in practical units

$$\gamma_{\max}(\text{fs}^{-1}) = 3.47 \times 10^{-3} \sqrt{I_{14}} - 5 \times 10^{-2} \frac{T_{\text{keV}}^{2/3}}{\lambda_\mu^{4/3} (L/\lambda)^{2/3} I_{14}^{1/6}}. \tag{3.25}$$

where L/λ is the density scale length normalized to the laser wavelength in vacuum. Although, the obtained k_{ey} dependent growth rate differs from that of Lasinski and Langdon, its maximal value and so the threshold condition is very similar. The following threshold is obtained numerically

$$\frac{v_{\text{osc}}^2}{4 v_e^2} k_0 L = 0.0504 \frac{L_\mu \lambda_\mu I_{14}}{T_{\text{keV}}} > 3.1 \tag{3.26}$$

where the constant 3.1 slightly deviates from the analytical value (2.8) derived from Eq. 3.25.

Afeyan and Williams [30] reinvestigated the problem exhaustively invoking the variational principle. They calculated the growth rate and the threshold not only for linear density profile, but for parabolic profiles also. Furthermore, they investigated oblique incidence with p and s polarization. They obtained the same results as Simon *et al.* under similar conditions. In the case of oblique incidence, s polarization and a linear density profile, the nominal scale length (L) is larger than the effective scale length in the $\mathbf{v}_{\text{osc}}$ and $\mathbf{k}_0$ plane, $L_{\text{eff}} = L/\cos(\beta)$. The increased scale length is compensated by the decreased

---

[5]There is a difference between the forms of the electric field here and in Ref. [67], which influences the definition of v_{osc}. Their definition expressed with the one used here is $v_{\text{osc Simon}} = v_{\text{osc}}/2$. There are some other works following the definition adopted by Simon.

intensity due to the enlarged focus spot in oblique incidence so the threshold will not change (Eq. 3.26), although above threshold this yields a slightly slower growth. The situation is more complex for p polarization. Here the effective scale length depends on the propagation direction of the plasmon, i.e., on the direction of the wave vector component perpendicular to $\mathbf{k}_0$. Thus, the threshold depends on the fact in which arm of the maximum growth rate hyperbola the plasma wave is located. It can be higher than for perpendicular incidence. The theory suggests that the growth rate far above threshold is not affected by the inhomogeneity and is slightly slower than for perpendicular incidence.

There are two important effects of the inhomogeneity on the TPD which are valid for small density scale length also and must be taken into account. Firstly, the propagation of the plasma wave leads to a rapid change of its wavevector due to the high dispersion. The interaction with the pump wave depends strongly on the wavevector and so does the instability growth rate. Therefore, the plasma wave propagates away from the maximum growth area in the k space and switches off the instability. Practically, the plasmon generated on the maximum growth rate hyperbola propagates and leaves the hyperbola. Secondly, the more the plasma density changes within a plasmon wavelength the harder the generation of a plasmon. This is suggested by the inhomogeneous part of the growth rate in Eq. 3.23, although this part does not contain it explicitly.

The electron plasma waves grow exponentially due to the instability, but this growth is limited by nonlinear processes. There are several nonlinear processes that play an important role in this saturation process depending on the laser pulse duration. In the long pulse regime (> 100 ps) the typical saturation mechanisms are provided by the ponderomotive force originating from the beating of the electric fields of the electron plasma waves [68]. It should be repeated that the TPD instability is based on the ponderomotive force from the beating of the plasma wave electric fields with the laser electric field. The electric fields of plasma waves can be represented as $\mathbf{E}_{e1,2} = \mathbf{E}_{1,2} \cos(\mathbf{k}_{e1,2}\mathbf{x} - \omega_{e1,2}t)$. The corresponding ponderomotive force

$$F_{\mathrm{pond}} \sim \nabla(\mathbf{E}_{e1} + \mathbf{E}_{e2})^2 = \nabla\{\mathbf{E}_1\mathbf{E}_2 \cos[(\mathbf{k}_{e1} - \mathbf{k}_{e2})\mathbf{x} - (\omega_{e1} - \omega_{e2})t] +$$
$$+ E_1^2 + E_2^2 + \mathbf{E}_1\mathbf{E}_2 \cos[(\mathbf{k}_{e1} + \mathbf{k}_{e2})\mathbf{x} - (\omega_{e1} + \omega_{e2})t]\}.$$

After cycle averaging this force, the first term has low frequency $\omega_{e1} - \omega_{e2} \approx 0$ and the periodicity is $\mathbf{k}_{e1} - \mathbf{k}_{e2} \sim 2\mathbf{k}_0$. Therefore this force can drive ion perturbations with $k_i \sim 2k_0$ leading to a decay of a plasma wave into an ion acoustic wave and another plasma wave (see Sec. 3.4 and Sec. 3.6). This is the main saturation mechanism of TPD with long pulses [69, 70]. The saturation is so severe in the long pulse regime that the linear theory does not apply for the measured results. Second and third terms are the usual ponderomotive force leading to density profile steepening on a longer time scale that

quenches the already saturated instability [71, 72]. The last term becomes zero due to cycle averaging. In the short pulse regime the expected dominant saturation mechanism is the trapping and wavebreaking, discussed in Sec. 2.3.4.

3.3 Stimulated Raman scattering

Another important parametric instability in laser-plasma interactions is the stimulated Raman scattering (SRS). This instability is a resonant decay of the laser light into a scattered light and an electron plasma wave. Therefore SRS is responsible for backscattering of laser radiation besides hot electron generation [73, 74].

The energy and momentum conservations are

$$\omega_0 = \omega_1 + \omega_e, \qquad \mathbf{k}_0 = \mathbf{k}_1 + \mathbf{k}_e \tag{3.27}$$

where the index $\omega_{0,1}$, ω_e and $\mathbf{k}_{0,1}$, $\mathbf{k}_e$ corresponds to the frequency and the wavevector of the laser light, the scattered electromagnetic wave and the electron plasma wave, respectively. SRS takes place in a wide range of densities up to quarter critical, which is seen from the energy conservation for resonant waves.

The SRS instability was thoroughly investigated theoretically in homogeneous [25, 75] and inhomogeneous plasmas [76, 77]. The growth rate has been calculated in different situations depending on the direction of the scattered electromagnetic radiation, i.e. in back, side, and forward direction. In order to obtain the instability dispersion relation first the electromagnetic wave and the plasma wave is described similarly to Eq. 2.21 and Eq. 3.15 [25]. The fields are expressed with potentials and the vector potential ($\mathbf{A}$) is associated with the transversal light waves and the scalar potential (ϕ) with the longitudinal electron plasma wave in the $\nabla \mathbf{A} = 0$ gauge. The current can also be split into transversal and longitudinal parts assuming $\mathbf{A}\nabla n_e = 0$, which results in two coupled equations. Using $\mathbf{A} = \mathbf{A}_0 + \widetilde{\mathbf{A}}$, where $\mathbf{A}_0$ ($\widetilde{\mathbf{A}}$) is the vector potential of the laser (scattered light). Linearizing with respect to $\widetilde{\mathbf{A}}$, Fourier transforming, and combining with Eq. 3.15 the SRS dispersion relation is received

$$\omega^2 - \omega_{pe}^2 - 3v_e^2 k_e^2 = \frac{\omega_{pe}^2 k_e^2 v_{\rm osc}^2}{4} \times$$
$$\left[\frac{1}{(\omega + \omega_0)^2 - \omega_{pe}^2 - c^2(\mathbf{k}_e + \mathbf{k}_0)^2} + \frac{1}{(\omega - \omega_0)^2 - \omega_{pe}^2 - c^2(\mathbf{k}_e - \mathbf{k}_0)^2} \right] \tag{3.28}$$

where $\omega = \omega_{\rm real} + i\gamma_{\rm SRS}$ is the complex frequency of the plasma wave as before, $\omega_{\rm real}$ is the real frequency and $\gamma_{\rm SRS}$ is the growth rate in homogeneous plasmas. Introducing the

notations $D \equiv \omega^2 - \omega_{pe}^2 - 3v_e^2 k_e^2$ and $D_{1\pm} \equiv (\omega \pm \omega_0)^2 - \omega_{pe}^2 - c^2(\mathbf{k}_e \pm \mathbf{k}_0)^2$ the dispersion relation can be transformed into the following form

$$1 = \frac{E_0^2 g(k_e)}{D}\left(\frac{1}{D_{1+}} + \frac{1}{D_{1-}}\right)$$

where E_0 is the laser electric field and $g(k_e)$ is a function determined from Eq. 3.28. The analogy between this equation and the general multi-mode dispersion relation (Eq. 3.11) is striking. Since the measurements were performed in the plane of polarization the investigations are restricted to scattering in this plane. The SRS backscattering growth rate with the resonant plasma wave ($\omega_{\mathrm{real}} = \omega_e$) in a homogeneous plasma neglecting the nonresonant D_{1+} part and assuming $\omega_e \gg \gamma_{\mathrm{SRS}}$ and $v_e \ll c$ is

$$\gamma_{\mathrm{SRS}} = \frac{k_e v_{\mathrm{osc}}}{4}\left[\frac{\omega_{pe}^2}{\omega_e(\omega_0 - \omega_e)}\right]^{1/2} \tag{3.29}$$

where the plasmon wavevector

$$k_e = k_0 + \frac{\omega_0}{c}\left(1 - \frac{2\omega_{pe}}{\omega_0}\right)^{1/2} \tag{3.30}$$

which reaches k_0 around quarter critical density, where the growth rate is maximal and has a value of $k_0 v_{\mathrm{osc}}/4$ similarly to TPD. Side scattering generally has a lower growth rate and vanishes in the plane of polarization, because the electric fields of the laser and the scattered light are perpendicular and thus their common ponderomotive force that drives the instability is zero (Fig. 3.1). Forward Raman scattering has a lower growth in underdense plasmas, but around the quarter critical density becomes comparable with the back scattering.

It should be noted that around the threshold SRS has somewhat different growth rate [75], but this is irrelevant for this work. When the laser is strong enough that $\gamma_{\mathrm{SRS}} \approx \omega_e$ the instability is *strongly coupled* and the previous results are invalid. In the strongly coupled regime the growth rate is proportional to $E_0^{2/3}$ and the $\Re e(\omega) \neq (\omega_{pe}^2 + 3v_e^2 k_e^2)^{1/2}$, but depends on the laser intensity and the generated waves are a strongly modified version of the natural ones [32]. This regime for SRS and TPD also requires relativistic intensity at the quarter critical density, where a completely new description is needed. Damping of the daughter waves or gradient in the plasma density cause a threshold laser intensity. Including a damping coefficient for the plasma wave (γ_e) that can be for example collisional damping as before in Eq. 2.33 and another coefficient for the scattered wave (γ_1) which is for example collisional absorption the following threshold condition is received $\gamma_{\mathrm{SRS}} \geq (\gamma_e \gamma_1)^{1/2}$. The actual growth rate is zero and γ_{SRS} is the growth rate in a homogeneous plasma without damping. Using this result the threshold caused by inhomogeneity can

also be determined. In an inhomogeneous plasma the phase matching ($\kappa \equiv k_0 - k_1 - k_e = 0$) depends on the density and can be approximately fulfilled only in a finite spatial range (l). This is taken into account as a damping term proportional to v_g/l, where v_g is the group velocity of the wave [25]. Expressing $\kappa(x) = \kappa(0) + \kappa' x$ and the phase matching is exactly satisfied in $x = 0$ ($\kappa(0) = 0$). Using the previous threshold condition $\gamma_{\mathrm{SRS}}^2/(\kappa' v_{g1} v_{ge}) \geq 1$ is obtained for the threshold due to density gradients. Much below $n_c/4$ the $v_{g1} \approx c$ and this threshold can be written as

$$\frac{v_{\mathrm{osc}}^2}{4c^2} k_0 L = 1.1 \times 10^{-4} L_\mu \lambda_\mu I_{14} > 0.5 \tag{3.31}$$

This threshold is higher than that for TPD. Near to the quarter critical density the scattered electromagnetic wave has a slower group velocity and therefore the threshold is lower by $(k_0 L)^{1/3}$ [26].

Rousseaux *et al.* have experimentally validated the linear theory of SRS using a laser with 500 fs pulse duration [33], because this regime is hardly accessible with long laser pulses. Meyer *et al.* showed that the exponential growth lasts approximately 1% of the pulse duration of a long laser pulse with 2 ns pulse duration [78].

It is important to mention that around the quarter critical density SRS and TPD can share the same plasma waves. The growth of the instabilities depends, among others, on the amplitude of the daughter waves. The amplitude of the shared wave is certainly higher in this case, which leads to a boost in the growth of both instabilities. Afeyan and Williams elaborated the previous situation and called this high frequency hybrid instability [79], but others have identified it at relativistic intensities also [80, 81]. This was first suggested based on experimental observations by Meyer [82]. As it will be shown, this effect can contribute to the presented results in this work due to the plasmon propagation.

3.4   Other parametric instabilities

Other parametric instabilities connected to laser-plasma interaction will be briefly discussed. Stimulated Brillouin scattering (SBS) is a resonant decay of a laser photon into a scattered photon and an ion-acoustic wave. The ion-acoustic waves have very low frequency, but a significant wavevector of the order of the laser's wavevector $\mathbf{k}_0$, therefore the scattered light has almost the same wavelength as the laser light. The growth rate is highest for backscattered light, in which case the reflection can reach large values as $10 - 50\%$ [26]. This fact made this instability an important concern in the long pulse

experiments. Nevertheless, this instability is not present in sub-ps laser-plasma interaction. This is due to the long time period of the ion-acoustic waves – typically some ps – which exceeds the laser pulse duration. 1.2 ps is the shortest FWHM laser pulse duration wherewith SBS was observed [83], whereas the pulse width at the SBS threshold intensity was much longer than the FWHM value and the period of the ion-acoustic wave [84]. It is much easier to reach the strongly coupled regime with SBS ($\omega_i \leq \gamma_{\text{SBS}}$) than with SRS due to the lower ion-acoustic frequency [85]. This regime is accessed already at an intensity about 10^{15} W/cm^2 at 1 μm laser wavelength. It was shown before that TPD saturation is caused by the ponderomotive force associated with the electron waves. There are no involved electron plasma waves in SBS only ion-acoustic waves having smaller electrostatic fields therefore saturation occurs at higher wave amplitudes and it is expected that these larger waves induce the large reflection.

Stimulated electron-acoustic decay instability (SEAS) is a resonant decay of a laser radiation into a scattered radiation and an electron-acoustic wave [43]. This process is similar to SRS, but the generated electron wave has an acoustic dispersion relation and for this reason a smaller phase velocity. Since the amplitude of the acoustic wave is three orders of magnitude smaller than that of the electron plasma wave the SEAS is not an important mechanism.

Certainly plasma waves can also decay resonantly. Langmuir wave decay instability (LDI) is a process by which a large amplitude electron plasma wave decays into a secondary plasma wave and an ion acoustic wave [86]. LDI plays a dominant role in the saturation of electron plasma waves generated by for example TPD or SRS [31, 86, 87]. The daughter Langmuir wave has the same frequency as the original, but an antiparallel wavevector. The previous coupling process of a plasmon to another plasmon and a phonon can repeat from the new plasmon leading to a LDI cascade [88].

The electromagnetic decay instability (EDI) involves the decay of an electron plasma wave into a scattered electromagnetic wave and an ion acoustic wave. This instability generates from the TPD plasmons at the quarter critical density electromagnetic waves with an efficiency $\omega_0/2$ [89] in long pulse experiments. Although SRS can produce directly light at $\omega_0/2$ frequency, but the observed double-peaked half harmonic spectrum refers to TPD origin.

It is interesting to note that a possible process in magnetized plasmas is the resonant decay of a plasma wave into two electromagnetic waves [90], which is not possible in unmagnetized plasmas.

3.5 $3\omega_0/2$ **generation**

To explain the origin of three-halves harmonic radiation several processes were suggested (see for example [91] and references therein). Nevertheless, the unusual frequency of this emission reduces the number and the sort of models, which generally contain two main stages. The production of plasmons with a frequency of about $\omega_0/2$ is the first step in the three-halves harmonic generation. The candidates for this step are the previously discussed parametric instabilities: TPD and SRS. In long pulse laser-plasma experiments SRS is rejected due to the higher threshold in inhomogeneous plasmas [92]. It will be shown in the present work that under certain circumstances SRS from fs-laser produced plasmas can lead to $3\omega_0/2$ generation. Barr proposed for the second step a combination of three plasmons or a combination of an incident or reflected laser photon with a plasmon [93, 94, 95]. The former is a higher order process having negligible probability. The basic conservation laws of the latter coupling process are

$$\omega_{3/2} = \omega_e + \omega_0, \qquad \mathbf{k}_{3/2} = \mathbf{k}_e + \mathbf{k}_0 \tag{3.32}$$

where $\omega_{3/2}$ and $\mathbf{k}_{3/2}$ are the frequency and wavevector of the three-halves harmonic radiation. In the long pulse regime TPD was identified experimentally as the source of $3\omega_0/2$ radiation using spectroscopy and Thomson scattering [72, 28]. This radiation is an indirect sign of TPD instability. The typical $3\omega_0/2$ spectra contains a pair of peaks, a stronger red and a weaker blue shifted component originating from slightly different electron densities below quarter critical [29]. These two peaks correspond to the forward and backward propagating plasmons in the TPD instability (Fig. 3.2). It was suggested to use the spectral splitting of the $3\omega_0/2$ radiation as an electron plasma temperature diagnostic [96, 97]. The problem is that the spectrum depends not only on the temperature, but on the experimental geometry also as the incident and the observation angles and therefore this radiation is not well suited for diagnostic purposes [98]. In fact, the original plasma waves cannot generate three-halves harmonic radiation without propagation, but collisional damping is so severe that these plasmons are damped before they could reach the point, where coupling is already possible. The amplitude of the TPD Langmuir waves is high enough to reach saturation governed by LDI and generate new electron plasma waves and ion acoustic waves. These daughter plasma waves from LDI are already capable of coupling to the laser in long pulse experiments [87]. This saturation process can explain the asymmetric spectra with double peaks in the same time [31, 99].

The situation changes at relativistic intensities higher order processes start to play a more and more dominant role [80, 81]. For example the simultaneous absorbtion of two laser photons at the quarter critical density can lead to a direct generation of the

$3\omega_0/2$ and a Langmuir wave. This processes is labelled as stimulated Raman harmonic scattering. These higher order effects will be briefly discussed later.

Three-halves harmonic radiation together with the second harmonic were used as plasma diagnostics. Imaging the target and filtering the plasma emission to get these two harmonics the position of the quarter critical and critical density surfaces were tracked [100, 101].

There is no systematic study about $3\omega_0/2$ radiation with sub-picosecond lasers, although it is regularly observed in ultrashort high intensity laser-plasma experiments [34]. A striking difference between the long and short pulse regimes is that the bandwidth of the three-halves harmonic emission is much broader with short high intensity lasers. The width is larger than the typical splitting of the spectral peaks with long less-intense lasers and therefore the spectrum contains only one broad spectral feature expanding to the red and blue side of the exact $3\omega_0/2$ wavelength. The present work involves a systematic experimental and theoretical investigation of parametric instabilities with sub-picosecond laser pulse durations through the characterization of the three-halves harmonic radiation.

3.6 Application to experiments

In this section the previously discussed theory (Chap. 2 and 3) will be applied and expanded for specific experiments. In the experiments described later (Chap. 5) the electron density scale length was below 10 μm, typically 2-3 μm, indicating that care must be taken in adopting the well known analytic models [30, 65, 66, 67] for the TPD.

The initial process in the $3\omega_0/2$ generation is the plasmon production with approximately $\omega_0/2$ frequency. The TPD and the SRS will be investigated as potential sources of these plasmons. Following these parametric instabilities, a coupling between a plasmon and a laser photon produces a new photon with $3\omega_0/2$ frequency. The theoretical description of the above mentioned processes is started with the frequency and phase matching conditions, i.e. energy and momentum conservation, in the k space using the dispersion relations of the generated waves, similarly to Meyer and Zhu [28]. One should keep in mind, however, that frequency and phase matching alone is not sufficient to determine whether a $3\omega_0/2$ wave with detectable amplitude is generated. To complete the analysis, the growth rates in k space of the instabilities have to be considered. The k space analysis yields the wavevector of the generated $3\omega_0/2$ radiation, which determines the propagation direction and with it the angular distribution. This analysis is a compact and illustrative form of the generation process. To start, the simplest model, i.e. resonant unsaturated parametric instabilities will be used. Later in Sec. 5.4 the picture will be completed by

discussing additional effects, such as plasmon propagation or saturation.

The laser beam is focused with an angle of incidence α onto an inhomogeneous plasma with a density scale length of $L = n_e/|dn_e/dx|$ at the quarter critical density. The direction of the density gradient is parallel to the x axis and the plane of incidence is the x-y plane. The momentum conservation (Eq. 3.12) restricts the TPD generated plasmon wavevectors to a circle in k space at given plasma parameters (temperature and density). The normalized wavevectors are introduced here as $\widetilde{k} = kc/\omega_0$. Using Eqs. 2.18, 2.22, and 3.12 the plasmon wavevector generated by TPD has to satisfy

$$\left(\widetilde{k}_{ex} - \frac{\sqrt{\cos^2(\alpha) - 1/4}}{2}\right)^2 + \left(\widetilde{k}_{ey} - \frac{\sin(\alpha)}{2}\right)^2 \\ = \frac{\sqrt{n_e/n_c} - 2n_e/n_c}{3T_{\mathrm{keV}}/511} - \frac{3}{16} \tag{3.33}$$

where the $\omega_{pe}^2 \gg 3v_e^2 k_e^2$, or using normalized quantities the $42 \gg T_{\mathrm{keV}}\widetilde{k}_e^2$ approximation was used in the dispersion relation and the laser wavevector is taken at $n_c/4$. It can be seen from this equation that in fact TPD takes place below $n_c/4$ due to the finite electron temperature. Eq. 3.33 is a circle centered at the normalized wavevector $\widetilde{\mathbf{k}}_0/2$ with a radius that depends on T_{keV} and n_e. The analytical expression obtained without these approximations deviates negligibly from this TPD circle, the difference is on the order of 1%. The plasmon wavevector is limited by the Landau damping in the case of TPD, as will be discussed later.

The k space analysis of the SRS is alike that of the TPD. However, similar assumption about the dispersion relations cannot be made, because the frequency of the scattered electromagnetic wave depends strongly on the wavevector. The SRS generated plasmon wavevectors satisfy

$$1 = \sqrt{\frac{n_e}{n_c} + \frac{3T_{\mathrm{keV}}}{511}\left(\widetilde{k}_{ex}^2 + \widetilde{k}_{ey}^2\right)} + \\ + \sqrt{\frac{n_e}{n_c} + \left(\widetilde{k}_{ex} - \sqrt{\cos^2(\alpha) - \frac{n_e}{n_c}}\right)^2 + \left(\widetilde{k}_{ey} - \sin(\alpha)\right)^2} \tag{3.34}$$

This analytical curve is approximately a circle centered at the normalized wavevector $\widetilde{\mathbf{k}}_0$. Around the quarter critical density the plasmon frequency dependency on its wavevector can be neglected and $[1 - 2(n_e/n_c)^{1/2}]^{1/2}$ is obtained for the radius. SRS causes the scattered light wavevector to be smaller than the incident laser wavevector and this ultimately limits the plasmon wavevector. The scattered wavevector is negligible ($k_1 \ll k_0$) around the quarter critical density and consequently $\mathbf{k}_e \approx \mathbf{k}_0$.

Plasmons in the k space that can generate $3\,\omega_0/2$ radiation, are determined basically by the momentum conservation of this process (Eqs. 3.32 and 2.22). The equation governing their wavevectors is

$$\left(\widetilde{k}_{ex} + \sqrt{\cos^2(\alpha) - \frac{1}{4}}\right)^2 + \left(\widetilde{k}_{ey} + \sin(\alpha)\right)^2 = 2. \tag{3.35}$$

This is the so called *'radiation circle'* centered at the normalized wavevector $-\widetilde{\mathbf{k}}_0$ and with a radius of $\widetilde{k}_{3/2} = \sqrt{2}$. Any deviation from the analytical expression is relative small. Only the radius covers a wide range of values corresponding to the three-halves harmonic bandwidth.

The propagation of the electromagnetic and plasma waves in inhomogeneous plasmas is easily illustrated in the k space. The perpendicular components of the wavevector with respect to the density gradient (y and z components) are conserved and only the parallel component (x) changes in order to satisfy the dispersion relation. Therefore, the propagation direction of the waves in k space is antiparallel to the direction of the density gradient. As the waves propagate inwards the electron density increases and the x component of the wavevector eventually vanishes. At this point the waves are reflected and the x component of their wavevector starts to grow again. Correspondingly the $3\,\omega_0/2$ radiation that is generated at the quarter critical density, will also be refracted and its direction of propagation will change slightly as it reaches the vacuum. The propagation of the laser light in the plasma is illustrated with the red curves in Fig. 3.3 in the normal space and also in the k space.
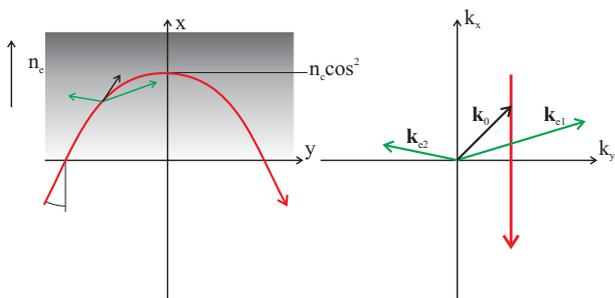
Figure 3.3: Propagation of the laser light in the plasma (red lines) and the TPD in the normal space and in the k space. The black arrow is the laser wavevector, and the green arrows correspond to the plasma waves.

The plasmons propagate with a group velocity of $v_g = 3v_e^2 k_e/\omega_e$, which using the normalized wavevector for plasmons and a frequency of $\omega_e \approx \omega_0/2$ has the value $v_g = c\widetilde{k}_e 6 T_{\mathrm{keV}}/511$. The maximal distance that a plasmon propagates is restricted either by the collisional damping of plasmons or by the maximal length of the wavevector, which in turn is limited by the Landau damping of plasma waves with long wavevector. The former is important in long pulse experiments and makes the plasma wave propagation and the change of the wavevector negligible, while the latter will be important in the ultrashort

pulse experiments. The plasmon propagation during the pulse duration is important, because $3\omega_0/2$ is generated only during this time. While the frequency of the plasmon remains constant during propagation, the parallel component of the wavevector changes according to Eq. 2.18

$$\Delta\widetilde{k}_{ex} = \widetilde{k}_{ex}\left(\sqrt{\frac{\omega_0\tau}{4\pi\widetilde{k}_{ex}L/\lambda} + 1} - 1\right) \tag{3.36}$$

where τ is the pulse duration. Here, a linear density profile is assumed, that is, the distance covered by the plasmons is smaller than the scale length. The calculation uses the WKB approximation, so it underestimates the wavevector change around $k_{ex} \approx 0$.

To conclude the theoretical analysis the formalism is applied to a specific example of three-halves harmonic generation in the k space. It is possible to predict the directions in which the $3\omega_0/2$ radiation is generated, and moreover, their spectra. As mentioned previously, this analysis will be far from complete without taking into account the evolution of the first step of the $3\omega_0/2$ production process, the parametric instabilities. The reason is that the initial exponential growth rates cause large variations in the amplitudes of plasma waves. Therefore, in some directions, which are in principle phase-matched, the three-halves harmonic radiation will have a negligible amplitude. Beyond that the spectral shape is even more sensitive to the details of the instabilities.

The value and properties of the maximum growth rate are only important as discussed. Restricting the analysis to the case where $\mathbf{k}_e$ is in the plane of $\mathbf{v}_{\mathrm{osc}}$ and $\mathbf{k}_0$ since these plasma waves grow faster. A plasmon wavevector component perpendicular to the $\mathbf{v}_{\mathrm{osc}}$ and $\mathbf{k}_0$ plane will appear only in the denominator of Eq. 3.17 thus diminishing the growth rate. As the coordinate system is fixed to the plasma density gradient the wavevectors of the plasmons having the maximum of this homogeneous TPD growth rate lie on the rotated hyperbola

$$\left(\widetilde{k}_{ex}\sin(\beta) + \widetilde{k}_{ey}\cos(\beta)\right)^2 = \left(\widetilde{k}_{ex}\cos(\beta) - \widetilde{k}_{ey}\sin(\beta)\right)$$
$$\times \left(\widetilde{k}_{ex}\cos(\beta) - \widetilde{k}_{ey}\sin(\beta) - \sqrt{3}/2\right) \tag{3.37}$$

here β is the previously calculated angle of incidence at the quarter critical density. This is the well known $k_{ey}^2 = k_{ex}(k_{ex} - k_0)$ maximum growth rate hyperbola for perpendicular incidence. This hyperbola and the wavevectors of the fastest growing plasmons point in the 45° direction between $\mathbf{v}_{\mathrm{osc}}$ and $\mathbf{k}_0$ for large values of k_e. The value of the maximum growth rate along this hyperbola is $\gamma_{\mathrm{max}} = k_0 v_{\mathrm{osc}}/4$. Eq. 3.16 has to be solved numerically to obtain the growth rate at an arbitrary plasmon wavevector. The numerical solution

also has its maximum along the hyperbola, but the maximum decreases with an increasing plasmon wavevector component perpendicular to $\mathbf{k}_0$ (k_{ey} in the following discussion). The TPD is illustrated in Fig. 3.3 in the normal and in the k space. The black arrow is the wavevector of the laser and the green ones correspond to the plasma waves. It should be noted that in this figure both the plasmons and the laser photons are plotted, later only the plasmon k space will be used.

Parametric instabilities certainly do not grow unlimited, because different processes such as coupling to other waves, pump depletion or plasma wavebreaking limit the amplitude of their daughter waves. LDI was identified as the nonlinear saturation mechanism of the TPD in the long pulse regime [31] (Sec. 3.4 and 3.2). In these experiments LDI had another very important role, it produced plasmons with 'new' wave vectors that were not produced by TPD and these plasmons could couple with the laser to generate $3\omega_0/2$. This is the main three-halves harmonic generation process in the ns regime. This process requires the generation of ion acoustic waves with some ps cycle time, which are generally suppressed in the fs regime. Consequently, the same or higher saturation amplitude is expected than for long pulses. An amplification of the plasma wave intensity of 7 - 9 e-foldings (10^3 - 10^4) was measured [69], which is a lower limit in the short pulse regime. Pump depletion does not play a role, because the three-halves harmonic energy is low enough to assume a negligible amount of energy in the plasma waves. Other processes involving only electromagnetic and plasma waves as well as wavebreaking are possible candidates as saturation mechanisms in short pulse experiments.

Now, the instabilities generated by a long and a short pulse laser with the same fluence will be compared. The amplification depends on the fluence ($F = I\tau$ in the case of a rectangular pulse) and the pulse duration (τ), in e-foldings $\gamma_{\max}\tau \sim \sqrt{I}\tau = \sqrt{F\tau}$. This estimate implies a factor of 100 less amplification with a 100 fs than with a 1 ns laser. Taking into account that the linear growth lasts 10 - 20 ps [28], approximately 1% of the pulse duration with ns lasers, it is expected a predominantly exponential growth for fs pulses. Consequently the instabilities have an absolute different behavior in the two pulse length regimes.

It is important to discuss briefly the plasma wave damping in the present experimental situation. The collisional and the Landau damping are considered as plasma wave damping mechanisms. In both cases the previously calculated instability growth rate is diminished by a corresponding term. The collisional damping similar to collisional absorption occurs due to the electron and ion collisions and the temporal damping rate at

the quarter critical is

$$\gamma_{coll} = \frac{\omega_{pe}^2}{2\omega_e^2}\nu_{ei} \approx 8.8 \times 10^{-5} \frac{Z}{\lambda_\mu^2 T_{keV}^{3/2}} \ \text{fs}^{-1} \tag{3.38}$$

where ν_{ei} is the electron ion collisional frequency and Z is the ionization charge state.

Electrons moving with approximately the phase velocity of a plasma wave are exposed to its electric field. These electrons are accelerated or decelerated depending on whether their speed is smaller or larger than the phase velocity of the wave. The laser plasma based electron acceleration and the Landau damping are utilizing this fact. In the case of a Maxwellian electron velocity distribution the number of electrons accelerated by the wave is higher than the decelerated ones, which leads to a net energy transfer from the wave to the particles. This loss mechanism, the Landau damping, is a very strong function of the phase velocity. Therefore, this is treated either as negligible or as dominant, in which case the plasmon is heavily damped. An easy estimation of the sizeable Landau damping $k_e\lambda_{De} \geq 0.3$ where $\lambda_{De} = \sqrt{\varepsilon_0 T_e/(n_e e^2)}$ is the Debye length, in useful units $\widetilde{k}_e \geq 3.4/\sqrt{T_{keV}}$. The complete Landau damping coefficient is:

$$\begin{aligned}\gamma_L &= \sqrt{\frac{\pi}{8}} \frac{\omega_{pe}^4}{k_e^3 v_e^3} \exp\left(-\frac{\omega_{pe}^2}{2k_e^2 v_e^2}\right) \\ &\approx \frac{857.3}{\lambda_\mu \widetilde{k}_e^3 T_{keV}^{3/2}} \exp\left(-\frac{63.88}{\widetilde{k}_e^2 T_{keV}}\right) \ \text{fs}^{-1}.\end{aligned} \tag{3.39}$$

Chapter 4

Validation of the linear theory

This chapter reports first experimental studies of high intensity fs-laser generated $3\omega_0/2$ radiation in inhomogeneous plasmas. It will be shown that measurements of the 3/2-harmonic yield as a function of the incident pulse duration are in excellent agreement with linear theory.

Parametric plasma instabilities contribute to the production of suprathermal electrons and also lead to the generation of large amplitude plasma waves which couple to the incident electromagnetic wave and result in new, frequency-shifted electromagnetic emission. An example of such a process is the generation of light with a frequency of 3/2 times the fundamental frequency. In the interaction of intense Ti:sapphire femtosecond laser pulses with solids, this manifests itself as a strong green emission [34], and is a signature of parametric instabilities operating close to quarter critical density $(n_c/4)$. It is important to study the $3\omega_0/2$ generation process since this radiation is generally observed in femtosecond, high intensity experiments. As there was no experimental study in this field, the first experiment with the three-halves harmonic radiation was performed to characterize its properties and identify the parametric instability that generates it with ultrashort laser pulses (in the 100 fs - 1 ps range) in a long density scale length plasma (L $\sim$ 100 μm). These experimental conditions are similar to that of the fast ignitor concept [22], which is another important issue in the presented results.

In long pulse laser-plasma interaction, the dominant production process for $3\omega_0/2$ radiation was found to be TPD, which occurs resonantly at $n_c/4$ [28]. With nanosecond and sub-nanosecond pulses, the instability reaches a nonlinear saturation caused by LDI [31]. Time-resolved Thompson scattering measurements in CO_2 laser-plasma interaction experiments at 3×10^{13} W/cm^2 (with 2 ns pulse length) revealed that for times up to 25 ps, TPD growth is within a linear regime; whereas after 50 ps, saturation occurs [28].

Temporal measurements of the plasma wave amplitude support these results [102]. However, the saturation timescale depends on the laser and plasma conditions and therefore will be different in other experiments. Typical TPD saturation levels of the enhanced electron plasma fluctuations for nanosecond laser-pulse experiments are a factor of 10^3 to 10^4 (7 to 9 e-foldings) above thermal noise levels [68].

In the femtosecond regime, however, the product of growth rate and pulse duration is much smaller as discussed in Sec. 3.6, so that one would expect analogous measurements to fall within the linear regime. In addition, almost no hydrodynamic motion occurs during the interaction time. Although several groups have reported SRS-backscatter measurements in underdense plasmas ($n_e < 0.01\ n_c$) [32, 33], no investigations of $3\,\omega_0/2$ generation by femtosecond lasers have been performed before this work [103].

The chapter starts with the description of the experimental setup, then the results are presented and it is followed by the discussion of the experimental results at the end.

4.1 Experimental setup

A 2-TW Titan:sapphire laser beam with 200 mJ pulse energy and with a repetition rate of 10 Hz was used for the experiment. The laser spectrum is centered around (790 ± 1) nm and has a bandwidth of about (11 ± 1) nm as shown in Fig. 4.1. The pulse duration directly after the pulse compressor was 100 fs. The beam propagated from the last compressor grating a distance of 4 m in air before entering a target chamber filled with air with a low ambient pressure of 5 mbar. This was chosen to reduce the debris from the target which tends to degrade the focusing optics especially when operating at 10 Hz. Nonlinear effects in air and in the 10 mm thick fused silica entrance window caused a pulse prolongation which resulted in an effective pulse duration of about 135 fs on target, but did not change the spectrum as can be seen in Fig. 4.1.
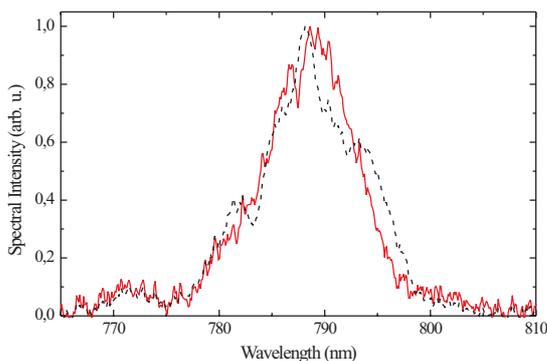
Figure 4.1: The spectrum of the Ti:sapphire laser directly after the compressor (black dashed line) and after a 10 mm thick fused silica window with full power (red solid line).

The experimental setup is shown in Fig. 4.2. The p-polarized laser was focused with
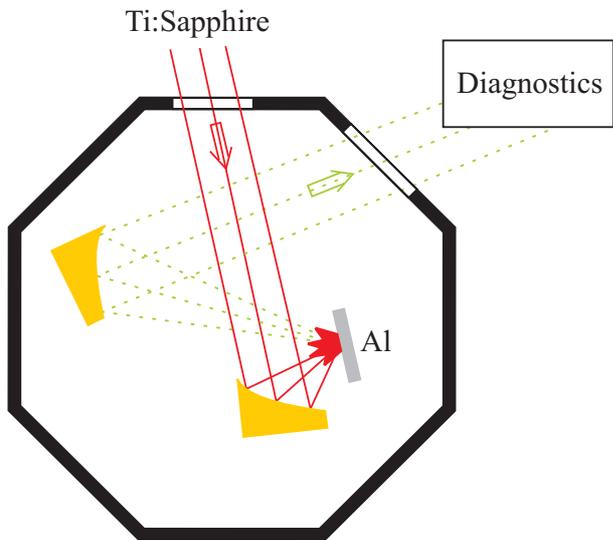
Figure 4.2: The experimental setup. The Ti:Sapphire laser was lead into the vacuum chamber through a quartz window and focussed at 45° with a gold off-axis mirror onto an aluminum target in an ambient pressure of 5 mbar. The averaged intensity in vacuum was 2.3×10^{17} W/cm^2. The specularly emitted $3\omega_0/2$ radiation was collimated with another off-axis mirror and sent through a BK7 window to the diagnostics.

a 122 mm focal length gold coated off-axis parabolic mirror onto a polished aluminum target. The measured spot size was (20 ± 5) μm by imaging the focus obtained with the attenuated beam, with a microscope objective onto a CCD. The spot size was the same with the attenuator placed after the laser compressor and in the vacuum chamber indicating that nonlinear phase front distortions in the air and in the window did not affect the focal intensity distribution. The angle of incidence was 45° and the aperture angle was 23°, which corresponds to an f number of f/2.5. For each laser shot a fresh surface was provided by shifting the target. Including reflection losses at the window and at a pellicle shield in front of the parabolic mirror an averaged intensity of $(2.3 \pm 1.1) \times 10^{17}$ W/cm^2 is obtained in vacuum, which is not reduced by ionization defocusing in air at a pressure of 5 mbar in the vacuum chamber as discussed in Section 2.3.1 [46].

The plasma is produced by a 100 fs long prepulse appearing 12.5 ns before the main pulse with a typical intensity of about 4×10^{14} W/cm^2. A slightly larger prepulse is shown in Fig. 4.3 with a contrast of 1:200. This prepulse was generated by allowing some leakage of a pulse through the extracavity Pockels cell. The pulse is a reflection from the output coupler thin film polarizer, in the regenerative amplifier, at the last but one round trip. In addition, a prepulse with 100 fs pulse duration was measured also at 4 ps before the intense main pulse with about the same intensity as the 12.5 ns prepulse by means of a third order autocorrelation shown in Fig. 4.4.

The generated $3\omega_0/2$ radiation was collimated in 45° observation angle with a second off-axis parabolic mirror and sent through a BK7 window to the diagnostics (Fig. 4.2) such as calibrated photodiode and spectrometer.
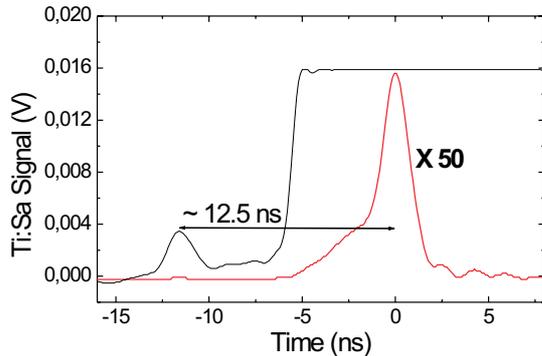
Figure 4.3: Measurement of the contrast of a prepulse coming 12.5 ns before the main pulse. The contrast is 1:200.
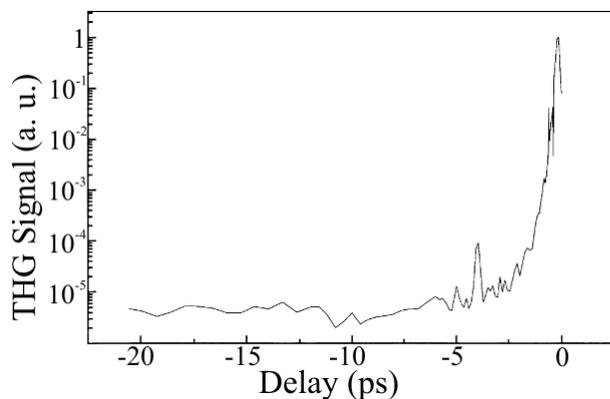
Figure 4.4: High dynamic range third harmonic autocorrelation. There is a short prepulse 4 ps before the main pulse.

4.2 Results

The energy of the $3\omega_0/2$ signal was measured carefully with a calibrated photodiode provided with an appropriate filtering and yielded approximately 100 nJ per pulse (average of ~ 50 pulses) into a solid angle of $\Delta\Omega \approx 2 \times 10^{-3}$ sr. Strong shot to shot energy fluctuations were observed. The conversion efficiency of the incident energy into 3/2-harmonic energy which was measured in specular direction is 5×10^{-7}. Assuming homogeneous angular distribution in the specular direction an efficiency of 3×10^{-5} is obtained. The second-harmonic emission from the plasma was measured also with a pulse energy of about 50 nJ.

Figure 4.5(a) shows 3 representative single shot $3\omega_0/2$ spectra, and in Fig. 4.5(b) an averaged spectrum is shown which was obtained over 15 shots. While the spectrum in Fig. 4.5(a) represented by the solid curve (#1) is similar to the averaged spectrum, the other two are examples show a larger discrepancy. Hence, the spectral details varied from shot to shot but the spectral width and the center wavelength were essentially conserved. The spectrum (b) with a center wavelength of (519 ± 1) nm, is blue shifted by about 8 nm with respect to the expected $3\omega_0/2$ center wavelength of (527 ± 1) nm, and has a

FWHM of (19 ± 1) nm. The measurement of the spectrum confirms that the observed radiation is due to 3/2-harmonic emission. In contrast to nanosecond laser experiments where typically well separated red and a blue shifted wings are observed [29, 98], only a broad spectral distribution was measured. For nanosecond laser experiments the 3/2-harmonic spectrum is explained by simulations including nonlinear TPD saturation and LDI [31]. Obviously, the 3/2-harmonic spectrum shown in Fig. 4.5 indicates that with femtosecond lasers a completely different coupling regime has to be applied. LDI develops on the time scale of the cycle time of ion acoustic waves, which is 3.5 ps determined from Eq. 2.20 for aluminum ($Z = 5$ $T_e = 1$ keV, $k_i = 2k_0$, $\lambda = 800$ nm). Hence LDI is excluded for the present experiment and electron plasma wave propagation is also insignificant as will be discussed later. Assuming a direct coupling of plasmons and laser photons, the spectral broadening is due to (1) the large bandwidth of the Ti:sapphire-laser (~ 11 nm), (2) the plasma electron temperature which leads to an electron density range where the $3\omega_0/2$ is generated, (3) non-resonant TPD (see Sec. 5.5), and (4) might be influenced by saturation which leads to an increased spectral broadening [104]. It should be noted that the broad bandwidth of the three-halves harmonic radiation supports the assumption that the pulse duration is equal with the interaction time. This is because if the bandwidth of $3\omega_0/2$ ($\Delta\lambda_{3/2}$) originated only from the laser bandwidth ($\Delta\lambda$), i.e. $\Delta\lambda_{3/2}/\lambda_{3/2} = \Delta\lambda/\lambda$, the different 3/2-harmonic wavelengths would be generated in different times during a chirped laser pulse. The amplitude of a plasma wave with a given wave vector would not be amplified during the whole incoherent laser pulse, only as long as the pulse is coherent (during the transform-limited pulse duration). As the bandwidth of $3\omega_0/2$ is much broader than the laser's bandwidth it is plausible that a given laser wavelength generates a very broad plasma wave and three-halves harmonic spectrum (this will be discussed in more detail in Sec. 5.5). Furthermore, the relative small change of the laser wavelength during the pulse – the small chirp – will almost not affect the produced spectrum and every spectral components will be amplified during the whole pulse. Figure 4.6 shows the measured signal of the fundamental (open squares), the second harmonic (crosses), and the 3/2-harmonic radiation (filled circles) as a function of the incident Ti:Sa laser pulse duration (τ) for a constant fluence. The pulse duration was varied in the range of 135 fs $-$ 900 fs by changing the distance between the compressor gratings. The measurement shows both directions from the optimal compressor position and therefore includes positive and negative chirp. The resulting signals were identical, consequently the generation process of the harmonics and the reflectivity do not depend on the sign of the chirp of the incoming laser pulse. Since the energy and the size of the focus were kept constant, the intensity is inversely proportional to the pulse length. The measurement shows that the ω_0-signal remained almost constant, indicating that the
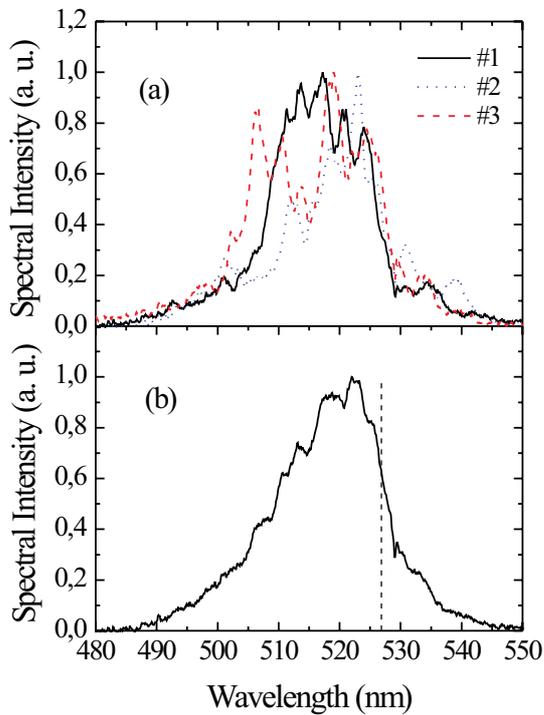
Figure 4.5: (a) Three measured $3\omega_0/2$ single shot spectra and (b) an averaged spectrum obtained over 15 laser shots. The dashed line shows the expected $3\omega_0/2$ wavelength.

reflectivity did not change in the applied intensity range. The second harmonic signal increases with shorter pulses, as found previously by others [105]. By contrast, the yield of the $3\omega_0/2$ radiation has a maximum at (350 ± 50) fs.

The spatial properties of the laser produced plasma are very important in the interpretation of the results. Therefore interferometric measurements were performed in order to characterize the preformed plasma with the second harmonic of the fs laser [106]. A Mach-Zehnder setup was used. Here the probe pulse is split into two parts, one propagates in vacuum and the other though the plasma. Then they are combined again and their two-dimensional interference image, the interferogram is recorded. As the index of refraction in vacuum is 1 and it differs from 1 in the plasma, the interferogram is characteristic to the spatial distribution of the plasma. Assuming radial symmetry the electron plasma density as a function of the position can be recovered with Abel-inversion technique [107].

The intensity of the preplasma generating laser pulse was varied in the range from 5×10^{14} W/cm^2 up to 10^{17} W/cm^2 and the delay between the pump pulse generating the plasma and the observing probe pulse was changed between 200 ps and 6 ns. An interferometric image with 2 ns delay and an intensity of about 10^{16} W/cm^2 is shown in Fig. 4.7 and the obtained density profile is in Fig. 4.8. The scale length (see Eq. 2.25) from an exponential fit is (65 ± 2) μm . After 2 ns the recombination of the plasma is significant.
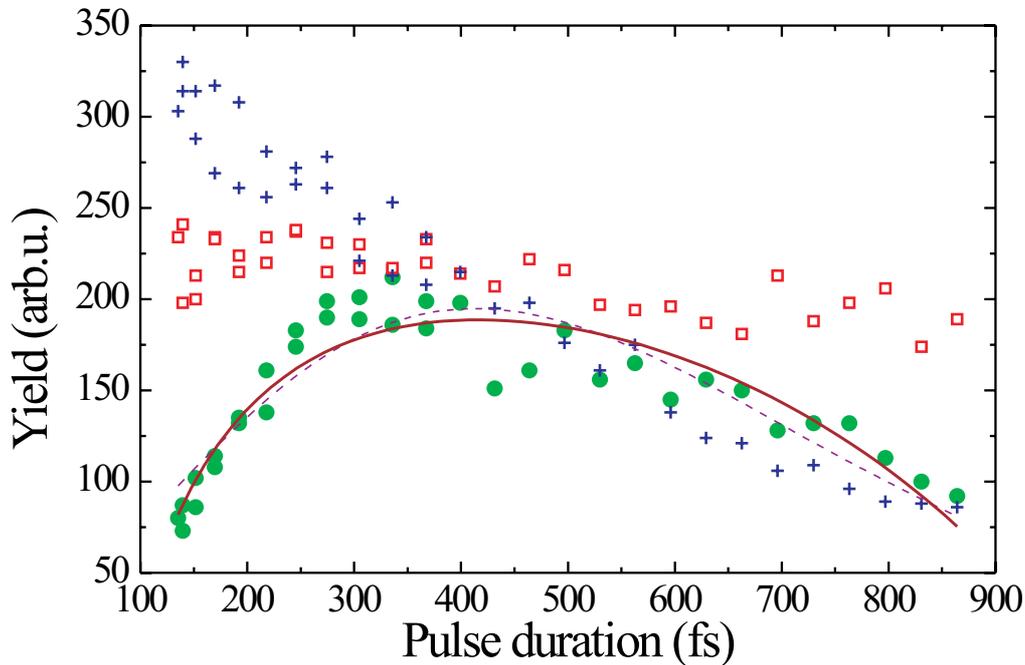
Figure 4.6: Yield of $3\omega_0/2$ (filled green circles), the $2\omega_0$ (blue crosses), and the reflected ω_0 signal (open red squares) as a function of the pulse duration of the incident Ti:Sa laser for *constant fluence*. The thick curve represents a theoretical fit with saturation, while the thin dashed curve is without saturation for the 3/2-harmonic signal.

A sign of the recombination in the interferometric images is that the interference lines start to bend into the other direction away from the target. This is due to that the refractive index of a gas is higher than 1, but of a plasma is smaller than 1. From the measurements a density scale length in the range of 100 μm $-$ 200 μm is inferred for the 12.5 ns time delay. For long delays (> 2 ns) the obtained scale length depends weakly on the time delay and much weaker on the intensity, because of the expansion that is accompanied by recombination and rapid cooling. The 4 ps prepulse produces plasma from the gas again. The discussion of the experimental results follows based on the detailed theoretical introduction.

4.3   Discussion

The key point in understanding the peculiar behavior of the 3/2-yield is that due to the prepulses, the linearly polarized intense laser pulses interacted with an extended inhomo-
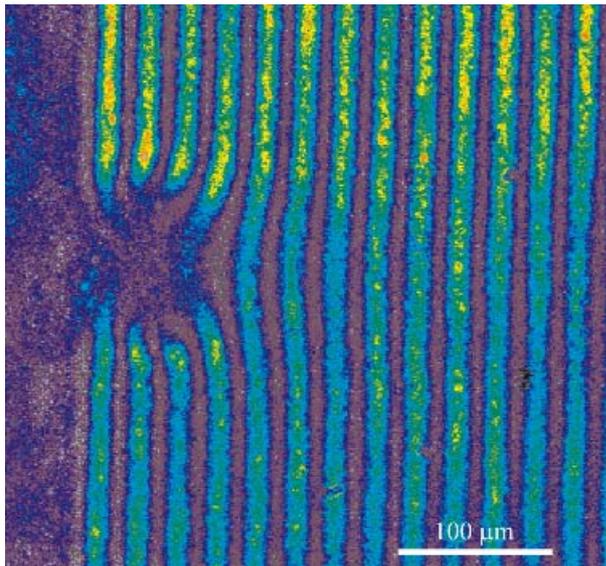
Figure 4.7: The obtained interferogram 2 ns after the generation of the plasma with a pump intensity of 10^{16} W/cm^2.
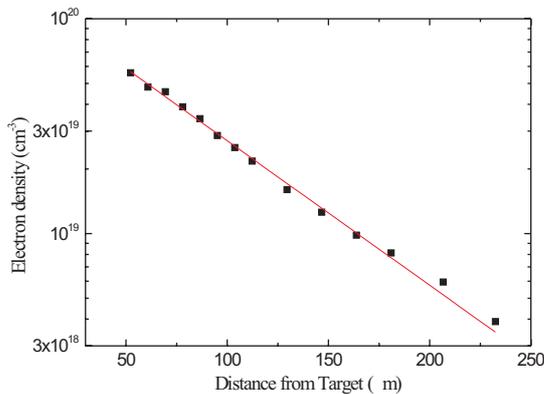
Figure 4.8: The electron density profile calculated with Abel-inversion technique from Fig. 4.7. The red line is an exponential fit to get the scale length, which is (65 ± 2) μm in this case.

geneous plasma with long density scale length to generate the $3\omega_0/2$. The mechanism for the $3\omega_0/2$ generation includes two steps as discussed in Sec. 3.5. First, a plasmon is generated with $\omega_0/2$ frequency by SRS or TPD just below the quarter-critical density [25]. Second, the $3\omega_0/2$ light is produced via a coupling of the plasmons and the laser photons. The effect of plasmon propagation in the inhomogeneous plasma or other effect changing the plasmon wavevector are generally important because in most cases the plasmons of significant growth generated by TPD do not satisfy the matching conditions – momentum and energy conservation, dispersion relations – of the 3/2-harmonic generation process [87]. A detailed theoretical analysis of the TPD process was made by Simon *et al.* [67] (see Sec. 3.2). Depending on the value of β_S (Eq. 3.22) different analytical solutions are valid. That means TPD generates plasmon pairs with different wave vectors and in some β_S range $3\omega_0/2$ can be generated without changing the plasmon wave vector, i.e. with a higher efficiency, as the wave vector matching needs always extra processes for example plasmon propagation or LDI. Direct coupling is not possible if $\beta_S > 1$, which is typically

the case for nanosecond, short wavelength (≤ 1 μm) laser-plasma interaction [67].

In the present case $\beta_S \approx 2 \times 10^{-3} - 2 \times 10^{-2}$ is estimated for $\lambda = 0.8$ μm , $T_e = 1$ keV, I $\sim 10^{16} - 10^{17}$ W/cm^2, which indicates that direct coupling is possible in this experiment. A detailed k-space analysis was performed for the applied experimental conditions (45° angle of incidence, 45° angle of observation) which shows also that coupling without changing the plasmon's wavevector can be established and plasmon propagation does not play an important role in $3\,\omega_0/2$ generation due to the short pulse duration and the long density scale length, Sec. 3.6. In the following, plasmon propagation is neglected in the analysis of the data.

The threshold intensity for SRS is in general higher than for TPD [68], but in this experiment the applied intensity is high enough to invoke both processes. It is readily shown for SRS that in the vicinity of $n_c/4$ the momentum of the incident light wave is almost completely transferred to the plasma wave. However, these plasmons do not fulfill the matching conditions for $3\,\omega_0/2$ (this will be discussed in more detail in Sec. 5.4). It is concluded that SRS is not the dominant production process for the 3/2-harmonic radiation observed under the described experimental conditions.

By contrast, TPD generates two plasmons with a frequency of about $\omega_0/2$ which take up the momentum of the incident photon. TPD provides a wide range of plasmon wave vectors, which allows the generation of 3/2-harmonic radiation in a large solid angle and also in the applied geometry. The observed 3/2-emission is therefore assumed to be due to the coupling of plasmons of $\omega_0/2$-frequency, which are generated by TPD in the vicinity of $n_c/4$ and incoming laser photons. The 3/2-intensity is proportional to the intensity of the laser beam at $n_c/4$ and to the square of the electron plasma wave amplitude.

In the linear regime, the plasma wave amplitude grows from thermal noise level (n_{th}) exponentially in time $n_{\text{TPD}}(t) = n_{\text{th}} \exp(\gamma t)$. To calculate the instantaneous amplitude, the maximum TPD growth rate γ is used in an inhomogeneous plasma, given by Eq. 3.20 extended with damping terms (Sec. 2.3.4) [25, 26]

$$\widehat{\gamma} = \frac{k_0 v_{\text{osc}}}{4} - \sqrt{\frac{0.65 k_0}{L}} v_e - 1.06 \times 10^{-2} \frac{Z \omega_{pe}^4 \ln \Lambda}{n_e v_e^3} - \gamma_L, \tag{4.1}$$

where $\widehat{\gamma}$ is a simplified growth rate as discussed in Sec. 3.2 obtained by Langdon, $k_0 \approx (\sqrt{3}/2)\omega_0/c$ is the light wavevector at $n_c/4$; c is the light speed in vacuum; $v_{\text{osc}}/c = \sqrt{I\lambda^2/(1.38 \times 10^{18} \text{Wcm}^{-2}\mu\text{m}^{\,2})}$ is the quiver velocity; Z is the ionization charge state; ω_{pe} is the local plasma frequency, and $\ln \Lambda \approx 8$ is the Coulomb-Logarithm. L is the electron density scale length defined by Eq. 3.2 at $n_c/4$. The first term on the right hand side is the maximum growth rate in homogeneous plasmas ($L = \infty$) without damping.
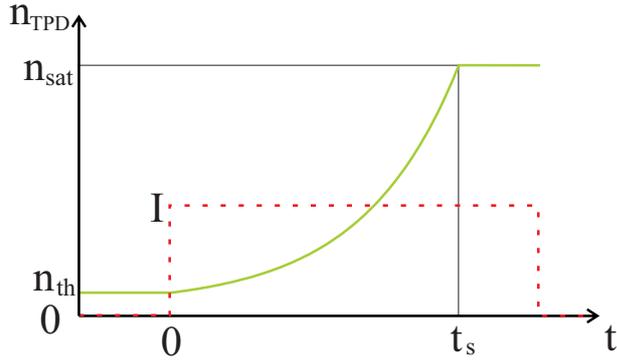
Figure 4.9: The electron plasma wave amplitude (n_{TPD}) and the laser intensity (I) as a function of time. The time t_s marks the point where saturation (n_{sat}) is reached from the initial thermal noise (n_{th}) and τ is the pulse duration.

The second term is due to a smaller interaction range in the inhomogeneous plasma, the third is the collisional damping and the fourth is the Landau damping, which is negligible if the plasmon wavevector satisfies $k_e < 4k_0 \approx 3.4\omega_0/c$ (Eq. 2.37) and dominant preventing the instability otherwise. The second and third terms introduce an intensity threshold. A preliminary estimate of the amplification using Eq. 4.1 assuming pure exponential growth ($\lambda = 790$ nm, $I = 2 \times 10^{17}$ W/cm^2, $T_e = 1$ keV, $L = 120$ μm , $Z = 4$, t $= 135$ fs) shows that for the experiment described here, 41 e-foldings are obtained, which corresponds to an amplification of 6×10^{17} and hence saturation has to be taken into account. In order to include saturation effects, a saturation value for the plasma wave amplitude (n_{sat}) is assumed which is reached at a time t_s as shown in Fig. 4.9.

For times $t < t_s$, the instability grows exponentially; for $t \geq t_s$, the amplitude is treated as constant. The interaction time is assumed to be equal to the laser pulse duration (τ). The measured $3\omega_0/2$ pulse energy for various pulse length is given by

$$E_{3/2} \sim \int_0^\tau I \, n_{\text{TPD}}^2(t)dt \tag{4.2}$$

with $I = I_0\tau_0/\tau$ where I_0 is the intensity at a pulse duration τ_0. The plasma wave 'intensity' appears in Eq. 4.2, which is the amplitude squared. Combining Eqs. 4.1 and 4.2, the following expressions for $E_{3/2}$ is readily obtained:

(a) without saturation

$$E_{3/2}(\tau) = A\frac{\exp[B\sqrt{\tau} - C\tau]}{B\sqrt{\tau} - C\tau} \tag{4.3}$$

(b) with saturation

$$E_{3/2}(\tau) = D\left[1 + \frac{1 - 2\ln(n_{\text{sat}}/n_{\text{th}})}{B\sqrt{\tau} - C\tau}\right] \tag{4.4}$$

where A,

$$B = 6.94 \times 10^{-10}\sqrt{I_0(\text{W/cm}^2)\tau_0(\text{fs})}\text{fs}^{-1/2}, \tag{4.5}$$

$$C = \{4.98 \times 10^{-2}\sqrt{T_{\text{keV}}/(L_{\text{eff}}(\mu\text{m})\lambda_\mu)} + 1.8 \times 10^{-4}Z/(T_{\text{keV}}^{3/2}\lambda_\mu^2)\}\text{fs}^{-1}, \tag{4.6}$$

and D are fitting parameters and T_{keV} is the electron temperature in keV. Henceforth, τ_0, $Z \approx 4$, L_{eff}, and λ_μ are treated as given and I_0 and T_{keV} as free parameters. From B the intensity at $n_c/4$ (I_0) is determined for a pulse duration of τ_0. This may differ from the nominal focused laser intensity in vacuum due to nonlinear propagation effects. L_{eff} is an effective scale length that takes the oblique incidence of the laser beam into account [30].

The thin dashed purple and thick solid brown curves shown in Fig. 4.6 are the result of respective fits using Eqs. 4.3 and 4.4 to the experimental data. A good agreement between measurement and theory is obtained in both cases. However, from these curves alone, it cannot be concluded whether saturation is reached or not. The first part in Eq. 4.1 is responsible for an increasing 3/2-signal with the pulse duration for incident pulses shorter than 350 fs, while for longer pulses the inhomogeneous and collisional parts lead to a decreasing signal. Since it is expected that LDI plays a minor role on femtosecond timescales, linear theory should apply to even higher e-foldings than for long laser pulses until the instability saturates through, for example wavebreaking. The deduced intensities using $\tau_0 = 135$ fs are without saturation: $(3.9 \pm 0.5) \times 10^{15}$ W/cm^2, with saturation assuming 10 e-foldings saturation level ($2\ln(n_{\text{sat}}/n_{\text{th}}) = 10$): $(2.4 \pm 0.1) \times 10^{16}$ W/cm^2, and 20 e-foldings: $(1.05 \pm 0.04) \times 10^{17}$ W/cm^2. There are more definite but much more complicated theories of TPD [30, 67] with slightly different maximum growth rates which essentially show the same behavior as the model of Ref. [26] and the experimental data.

The collisional absorption of the incident laser pulse was estimated for propagation up to the $n_c/4$ (Sec. 2.3.3) and found that it is between 5 % and 15 % so it is negligible, but ionization defocusing discussed in Sec. 2.3.1 in the preplasma is significant for the fundamental. Refraction of the three-halves harmonic in specular direction ($-45°$) by the laser generated density profile is negligible due to the perpendicular propagation to the laser direction. Estimates based on the theory of Fill [46] show that the intensity at $n_c/4$ is reduced by about one to two orders of magnitude due to ionization defocusing and therefore an intensity of $10^{15} - 10^{16}$ W/cm^2 is expected inside the plasma in agreement with the measurement. The spectral shift of the $3\omega_0/2$ radiation may be attributed to the ionization blue shift of the fundamental. The electron temperature obtained from the fit parameter C using Eq. 4.3 is on the order of ~ 230 eV. It should be stressed that even with saturation the duration of the exponential growth is in the present experiment at least 80% of the laser pulse length (see Fig. 4.9), in contrast to ns-laser experiments where it is approximately 1% [68]. Since most of the interaction time is within an exponential growth the fits with and without saturation are similar.

In this chapter the first experimental investigation of intense femtosecond laser gener-ated $3\omega_0/2$ radiation in dense long scale length plasmas was presented. The dominant

production process for the 3/2-harmonic radiation is the two plasmon decay. The good agreement of the theoretical models with the experimental data — in particular the occurrence of a maximum in the 3/2-yield as a function of τ (Fig. 4.6) provides a clear experimental verification of the TPD growth rate in an inhomogeneous plasma in the linear regime – Eq. 4.1.

Chapter 5

Angular distribution measurements

In this chapter detailed angular distribution and spectral measurements of the $3\omega_0/2$ radiation are presented in short scale length plasmas (0.8 - 7 μm) with intensities reaching the relativistic level (10^{16} - 6×10^{18} W/cm^2) [108]. The experimental results are in very good agreement with theoretical predictions based on two-plasmon decay and stimulated Raman scattering instabilities. New three-halves harmonic generation mechanisms are identified characteristic of femtosecond laser induced parametric instabilities. These are the joint interaction of incident and reflected laser beams as well as stimulated Raman scattering. It is shown both experimentally and theoretically that the three-halves harmonic radiation is a useful preplasma diagnostic tool.

Previously, the angular distribution was measured in the saturation dominated long laser pulse regime, which cannot be explained with the linear theory of unsaturated instability [28]. For ultrashort laser pulses, however, the situation is different. The instability remains in or near the unsaturated regime [103]. Therefore, it is expected that the experimental results are largely in agreement with the predictions of the linear model.

In Sec. 3.6 the theoretical description was outlined based on the theoretical analysis in the beginning of this work. The experimental setup is described in Sec. 5.1. The signal dependence and angular distribution results are presented in Sec. 5.2 and Sec. 5.3 and their detailed discussion is found in Sec. 5.4. The spectral measurements are discussed in Sec. 5.5.

5.1 Experimental setup

The generation mechanism can be identified with the previous theory by measuring the angular distribution and the dependencies of this distribution on various parameters. Now, these experimental observations will be discussed. The Ti:Sapphire laser had a central wavelength of 800 nm, a bandwidth of 14 nm, a pulse duration of 94 fs $\pm$ 5% (FWHM pulse duration assuming a Gaussian pulse), and p polarization. The energy on target varied between 155 and 175 mJ with a relative standard deviation of $\pm$ 4%. The pulse compressor was installed in a vacuum chamber to avoid nonlinear effects in the air. Two approximately 100 fs long prepulses were detected 10 ps and 4 ps before the main pulse. The intensity contrast with respect to the main pulse was measured to 2×10^{-4} using a third order, high dynamic range autocorrelator (see Fig. 5.1). An additional prepulse was introduced with the same pulse duration using a prepulse generator [109], which contained 2% of the energy of the main pulse. The delay of the prepulse was changed between 0 ps and 350 ps. A regular control of the focal intensity distribution indicated a FWHM focus diameter of 2.9 μm $\pm$ 0.3 μm (containing 43 % of the energy on target) and independently a Rayleigh range of 21 μm $\pm$ 3 μm by measuring the transverse intensity distribution in front of and after the focus in several positions. An angle of incidence of 45° leading to a slightly increased spot size in one dimension caused a decrease of the intensity on target. Experiments at different target focal positions, i.e. intensities were performed. The average intensity within the temporal and spatial FWHM on target including the previous effects was $(6.2 \pm 1.2) \times 10^{18}$ W/cm^2 in the focus. The temporal and spatial peak intensity is 1.72 times higher, that is $(1.1 \pm 0.2) \times 10^{19}$ W/cm^2. The average intensity was decreased by moving the target along the optical axis out of the focus, down to 10^{16} W/cm^2. As compared to decreasing the energy this method has the advantage that the signal to noise ratio of the detected $3\omega_0/2$ radiation was much larger. A disadvantage of changing the target position is that the angle of incidence will change to an angular range instead of a well defined value. It will be shown in this article that the power and the direction of the emission depends on, amongst other things, the angle of incidence therefore this angular range must be taken into account.

Aluminum targets on glass substrates were used in the experiments. The horizontal plane of the geometry is depicted in Fig. 5.2. The direction normal to the target surface in the horizontal plane is defined as 0°. The angle of incidence and the specular reflection angle were 45° and −45°, respectively. The angular range between 10° to −93° was scanned. The laser was focussed with an off-axis paraboloid gold mirror and the f/3.4 focusing yielded an angular width of 16° in the horizontal direction.
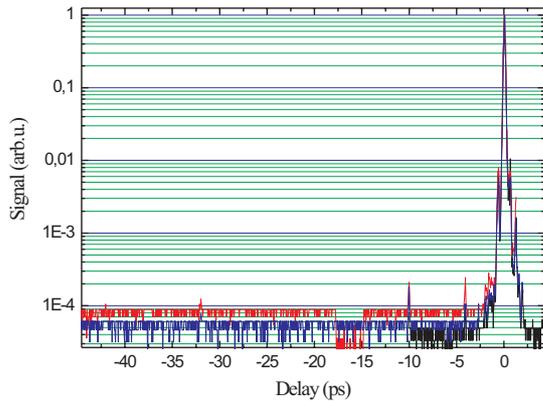
Figure 5.1: Three independent third harmonic generation autocorrelation traces with a dynamic range of better than 4 orders of magnitude. Two 100 fs-prepulses are detected at 10 and 4 ps.
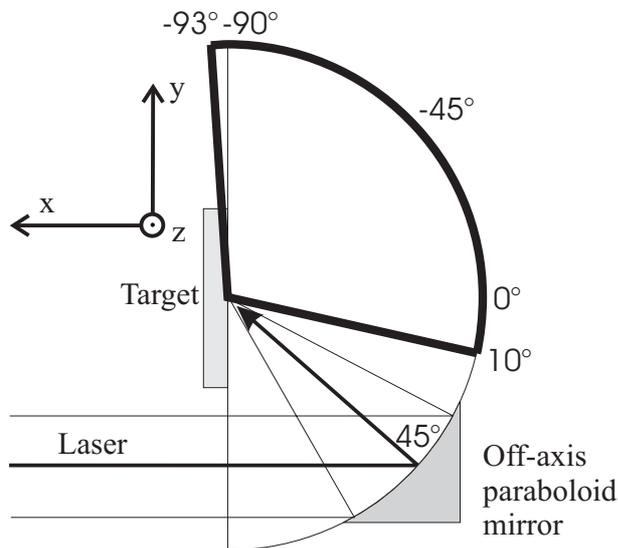

Figure 5.2: Geometry of the measurement and the definition of the angles.

X-ray spectral measurements [110] were performed at various intensities to determine the electron plasma temperature. The obtained spectra were simulated with known parameters. In the intensity regime used here the best fit yielded an electron temperature of 1.05 keV at 5×10^{23} cm^{-3} density. The variation of the temperature with the intensity was less than 15%. Although, the measured plasma density is much higher than the quarter critical density (4×10^{20} cm^{-3}) a similar temperature is assumed there, because their spatial distance is approximately 10 μm and the plasma temperature varies more slowly than the density [111].

5.2 $3\omega_0/2$ signal dependence on the scale length

The $3\omega_0/2$ signal dependence on the main pulse-prepulse delay, i.e. on the scale length (L) at the quarter critical density of the preplasma, was measured in order to determine the maximum $3\omega_0/2$ yield. The electron density scale lengths for the various main pulse

prepulse delays in Figure 5.3 were calculated by the 1D MEDUSA code [112]. A program has been written as a part of this work, which allowed a fast evaluation of the MEDUSA results and has also been applied to other works [113, 114, 115]. The simulations were compared to experimental results obtained under similar conditions [116] and the results indicate that the one-dimensional code simulating the plasma expansion is appropriate. For all delays applied the scale length is smaller than 7 μm. The plasma radiation was
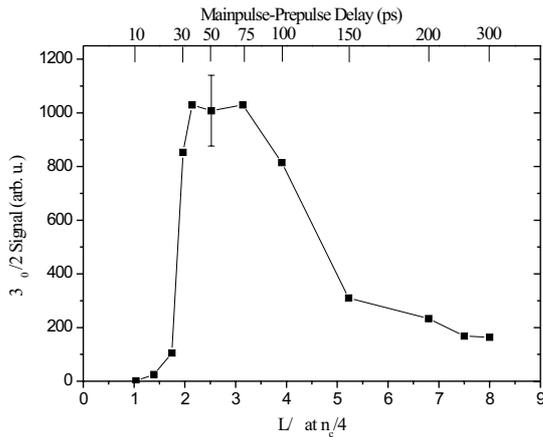
Figure 5.3: Change of the $3\omega_0/2$ signal with the scale length at I=7$\times10^{16}$ W/cm^2 for an observation angle of -15°.

directed through a vacuum window, spectrally filtered with care and the three-halves harmonic content was measured with a photodiode in -15° observation angle. The intensity on target was $(7 \pm 3) \times 10^{16}$ W/cm^2. The result is shown in Fig. 5.3. First, the signal increases rapidly with delay, reaches a maximum at around 50 ps, and decreases again after 100 ps. A similar behavior is observed in other directions ($-24°$, $-67°$). Only in 0° direction a deviation is found, here, the rapid increase is followed by a slow growth and no pronounced maximum is observed (Fig. 5.4). A threshold intensity of 7×10^{16} W/cm^2 is obtained from Fig. 5.3 at $L/\lambda \sim 1 - 1.25$ normalized scale length.
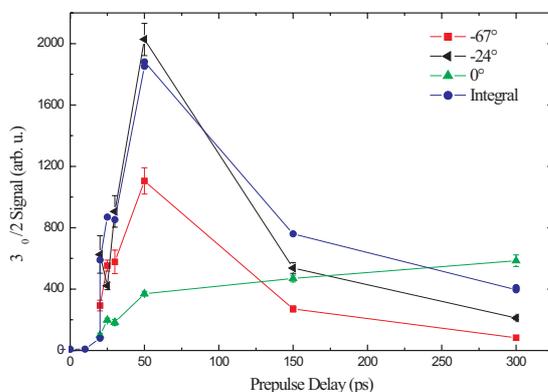
Figure 5.4: Change of the $3\omega_0/2$ signal with the delay between the main pulse and the prepulse at I=7$\times 10^{16}$ W/cm^2 for observation angles of $-67°$, $-24°$, 0° and the integral of the angle distributions from $-90°$ to $10°$.

Previous investigations have shown that the $3\omega_0/2$ photons are produced in a nonlinear

interaction between a fundamental laser photon and a plasmon, where the plasmon was generated by TPD [103], as was suggested originally by Barr [94, 95]. The spatial region along the density gradient where $3\omega_0/2$ radiation is generated, i.e. the *active region*, depends on the electron plasma temperature [117]. For the present experimental conditions a plasma temperature of about 1 keV and an active region from approximately $0.2n_c$ to $0.25n_c$ is estimated. An increasing signal is expected with increasing scale length as the inhomogeneous part in the growth rate decreases in Eqs. 3.23 and 3.25, but the change in the measured signal between $L/\lambda = 1$ and 2 is more dramatic than predicted by the exponentiated maximum growth rate multiplied with the pulse duration as the interaction time. Another discrepancy is found by calculating the threshold intensity at a given short scale length. $7 - 9 \times 10^{15}$ W/cm^2 is obtained from Eq. 3.26. Almost one order of magnitude smaller than the experimental value so it is concluded that other effects start to play a more dominant role. The measured signal cannot be explained even if saturation effects and the start of absorption mechanisms at ultra short scale length are taken into account. Although, the plasmon propagation reduces the signal at small scale length more than by longer ones due to the already discussed propagation away from the large growth rate regions in the k space, so drastic change in the signal as measured is not expected from this effect.

One possible explanation is based on the fact that no $3\omega_0/2$ radiation is generated as long as the active region is smaller than the wavelength of the plasmons. The plasmon wavelength for the present conditions is between 500 nm and 1 μm. This wavelength is estimated from the length of plasmon wavevector for plasma waves that have a significant growth rate and can generate $3\omega_0/2$. For the present conditions $k \sim 1 - 2\ k_0$ is found, where k_0 is the wavevector of the incident laser at the quarter critical density. Once the active region becomes comparable to the wavelength of a plasmon the exponential growth of the instability leads to a detectable signal level. This supports the well known experimental observations that the $3\omega_0/2$ light is a sign for a preplasma. Furthermore, the previous explanation implies that the presence of $3\omega_0/2$ radiation in high intensity experiments indicates a preplasma with a scale length of about λ or higher. Accordingly, the three-halves harmonic, which is optically very easily detected by typical laser wavelengths, can be used as a simple preplasma diagnostic tool. As the scale length increases other effects, such as the change of the plasma geometry and saturation of the growth rate, become important. It will be shown that $3\omega_0/2$ generation involving the incident and the reflected laser beams has a higher efficiency than that involving only the incident beam. The decreasing overlap between the incident and reflected laser beams is responsible for the decrease in the $3\omega_0/2$ signal with the scale length.

5.3 $3\omega_0/2$ **angular distribution**

5.3.1 Experimental results

To measure the angular distribution of the $3\omega_0/2$ radiation the setup shown in Fig. 5.5 was used. The plasma emission was guided out of the vacuum chamber by three 1 mm thick and 3 m long optical quartz fibers. After proper spectral filtering three photodiodes measured either the $3\omega_0/2$ signal, or the second harmonic signal, or the fundamental light. In the $-15°$ direction the different signals from the plasma were measured directly through a vacuum window.
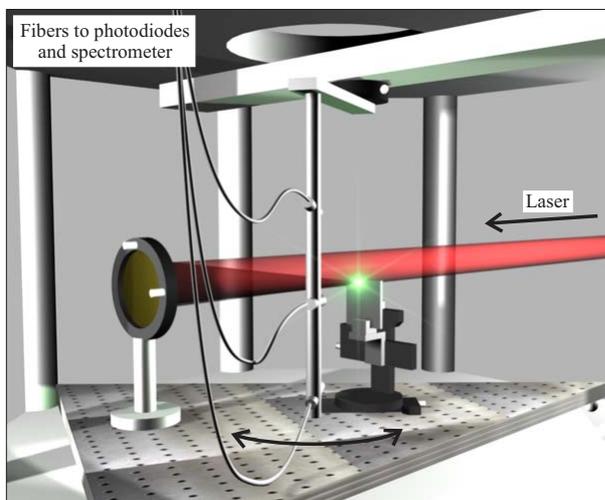
Figure 5.5: Setup of the angle distribution measurement.

The middle fiber was placed in the plane of incidence, its distance from the plasma was 190 mm and it collected light within an angle of $0.3°$. The upper and lower fibers were placed at an angle of $30° \pm 3°$ with respect to the horizontal plane. All data points in the angular distribution measurements were averaged over 10 to 100 laser shots depending on the measurement series, and the error bars denote the calculated statistical errors.

The measured angular distribution of the reflected fundamental laser light in the plane of incidence at an intensity of 6×10^{18} W/cm^2 is shown in Fig. 5.6. The angular spread around the peak at $-45° \pm 1°$ is $16° \pm 1°$ which reflects exactly the divergence of the focused laser beam. There is an important consequence of the tight focussing as discussed earlier, that is, if the target is not in focus the angle of incidence is not a well defined value but varies across the beam in the transverse direction ($45° \pm 8°$). In some cases this will cause a smearing of the measured features.

A typical $3\omega_0/2$ angle distribution for an intensity of 7×10^{16} W/cm^2 is shown in Fig. 5.7. A 20 ps prepulse was applied and the scale length just barely exceeds the threshold. Under
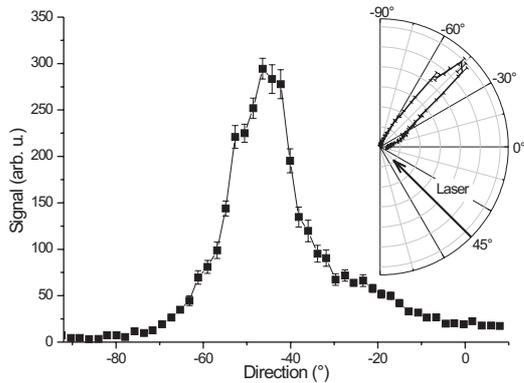
Figure 5.6: Angular distribution of the reflected laser pulse with I=6 × 10^{18} W/cm^2 and 50 ps prepulse. Inset: polar plot with the incident laser direction.

these conditions the $3\omega_0/2$ emission was very weak and showed high fluctuations which is a typical feature of the linear regime close to the threshold (exponential growth). The results show that the signal is peaked around the two angles $-28° \pm 3°$ and $-71° \pm 3°$. The error bars are relatively large due to the large fluctuations close to threshold. Recently, other groups made similar experimental observations of the double-peaked angular distribution [118].
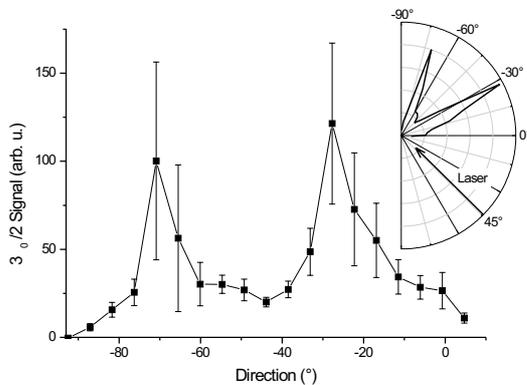
Figure 5.7: $3\omega_0/2$ angular distribution with 20 ps prepulse and 7×10^{16} W/cm^2 intensity. Inset: polar plot with the incident laser direction.

At a delay of 50 ps, where the $3\omega_0/2$ yield is maximal, the angle dependent signal is shown in Fig. 5.8. The intensity was slightly higher, namely 1.3×10^{17} W/cm^2. Again a double-peak distribution is found and the peaks are located at the same values as in Fig. 5.7. Two independent measurements are plotted in Fig. 5.8 to demonstrate that well above the threshold the reproducibility was very good. Fitting the data to two Gauss functions allows to estimate the widths and the relative amplitudes of the two maxima. The first higher peak is at about $-26° \pm 3°$ and has a FWHM of $30°$ and the second peak is at $-67° \pm 3°$ with a FWHM of $15°$. The widths have been deconvoluted with the angular spread of the incident laser beam. The diodes connected to the upper and

lower fibers recorded similar angle distributions as the center diode, but the characteristic peaks were not as pronounced.
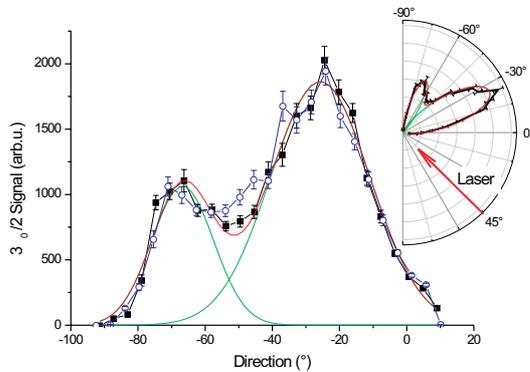
Figure 5.8: Two independently measured $3\omega_0/2$ angle distributions with 50 ps prepulse and 1.3×10^{17} W/cm^2 intensity. The solid lines are Gaussian fits to the peaks. Inset: polar plot with the incident laser direction.

In summary, the $3\omega_0/2$ spectra at low intensities show a very pronounced double-peaked structure. The detailed spectral features depend on the prepulse-main pulse delay, i.e. the scale length. To investigate the previous results in greater detail the intensity and the scale length, i.e. the size of the inhomogeneous plasma were varied.

5.3.2   Angular distribution as a function of the intensity

Fig. 5.9 shows angular distributions for different intensities at a 50 ps prepulse-main pulse delay. The intensity was varied by moving the target along the optical axis as depicted on the right side of Fig. 5.9. Accordingly, the intensity scale has its maximum in the middle of the axis and decreases in both directions, which corresponds to a target position in front of or behind the focus. Note that the scale length increases weakly with the intensity. For the lowest intensities almost no $3\omega_0/2$ emission is detected. At intensities which reach the relativistic level the observed double-peak structure disappears.
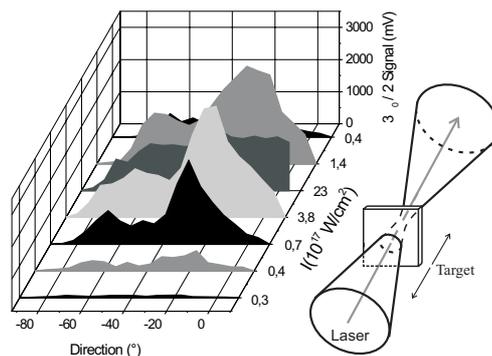
Figure 5.9: $3\omega_0/2$ angular distributions with different intensities and a 50 ps prepulse. The small picture on the right depicts how was the intensity changed. Correspondingly the intensity axis has its maximum in the middle. The double-peaked structure disappears at the highest intensity.

The TPD instability exhibits a threshold intensity at which the growth rate becomes positive and which was discussed in Eq. 3.26. This condition yields a threshold intensity of 6×10^{15} W/cm^2 [67] (assuming $T_e = 1$ keV and $L/\lambda = 1.6$). The measured threshold intensity in Fig. 5.9 is $(2 \pm 1) \times 10^{16}$ W/cm^2, and therefore, about 2 to 3 times higher than the calculated value. Comparing this discrepancy with the previous one, it can be seen that the difference between theory and measurement is smaller at a slightly longer scale length. This supports the statement that the inhomogeneous growth rate loses its validity around $L/\lambda \simeq 1$. The double-peaked structure is observed above the threshold up to an intensity of about 2×10^{18} W/cm^2. At this intensity the scale length is approximately 6 μm and the structure disappears similar to the results shown in Fig. 5.11.

Measurements of the $2\omega_0$ angular distribution show that the second harmonic radiation is also isotropic for scale lengths ~ 7 μm. The results are shown in Fig. 5.10 for an intensity of $(6 \pm 1) \times 10^{18}$ W/cm^2 and a prepulse main pulse delay of 50 ps, 150 ps, and 300 ps, respectively. The $2\omega_0$ signal decreases with increasing scale length. For the highest scale length the second harmonic radiation peaks in the $10° \leftrightarrow 90°$ range direction very similar to the $3\omega_0/2$ results. Therefore, it is assumed that the disappearance of the double-peak structure is a consequence of spatial effects, for example hole boring that affect all radiation and are not specific to the $3\omega_0/2$ radiation.
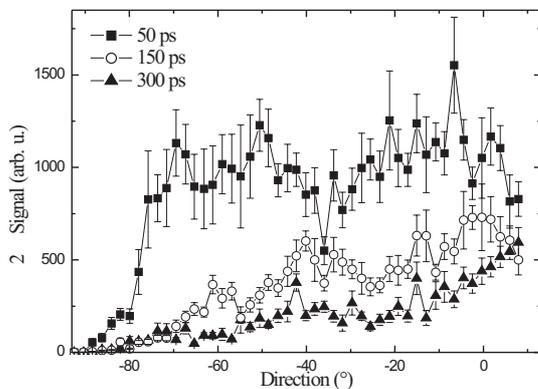
Figure 5.10: $2\omega_0$ angel distributions with an intensity of 6×10^{18} W/cm^2. The curve with the squares represents the measurement with a 50 ps prepulse, the circles a 150 ps prepulse and the triangles a 300 ps prepulse.

5.3.3 Angular distribution for various scale lengths

The angular distributions for different scale lengths at a non-relativistic intensity of $(1.3 \pm 0.5) \times 10^{17}$ W/cm^2 are depicted in Fig. 5.11. The double-peak structure is observed for prepulse-main pulse delays smaller than about 100 ps. This corresponds to the range in Fig. 5.3 where the signal is either growing or constant. At larger delays and consequently at larger scale lengths the peaks disappear, this starts at $L/\lambda \sim 5$. It is important to

note that the three-halves harmonic signal decreases significantly with the change of the angular distribution.
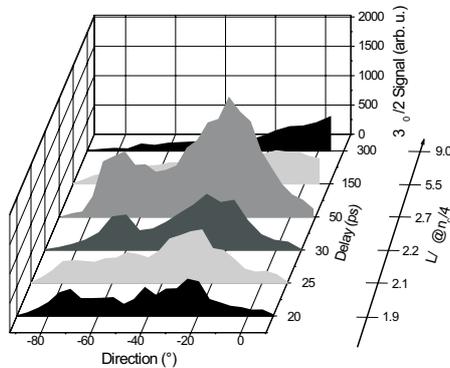

Figure 5.11: $3\omega_0/2$ angular distributions with different main pulse prepulse delays and 1.3×10^{17} W/cm^2 intensity. Increasing signal with double-peaked structure is observed with delays < 100 ps, while the double-peaked structure disappears and the signal decreases for longer delays.

5.4 Discussion of the angular distribution

To calculate the $3\omega_0/2$ scattering angle a k space analysis, introduced in the theory section, was performed. As mentioned above, the most probable $3\omega_0/2$ generation process is the coupling of a laser photon to a plasmon and the electron plasma wave is generated by the TPD. In Fig. 5.12 and Fig. 5.13 the k_x-axis is parallel to the direction of the density gradient as earlier.

For a given electron plasma temperature and electron density the tip of the plasmon wavevector generated by TPD is located on a circle, Eq. 3.33. The radius of the TPD circle depends strongly on the electron density and the wavevectors of plasma waves generated through TPD lie on the larger red dashed circle in Fig. 5.12 at approximately $0.2n_c$ (at 1 keV), on the middle dashed-dotted circle at $0.23n_c$ and on the smaller red solid circle at slightly less than $0.25n_c$. The $3\omega_0/2$ photon is born on the green 'radiation circle', which is described by Eq. 3.35. The 'radiation circle' hardly changes in the considered electron density range. There are two intersections between the 'radiation circle' and the TPD circle for densities between $0.2n_c$ and $0.25n_c$ which actually determine the emission directions of the $3\omega_0/2$ photons (see the $0.23n_c$ curve in Fig. 5.12). These wavevectors belong to plasmons that can generate $3\omega_0/2$ without propagation. The thin dotted lines are the axes of the new coordinate system at the quarter critical density for an angle of incidence of 45° in which the light wave vector has only one component (x'). This is the natural coordinate system of the $3\omega_0/2$ generation process. At an intensity of 10^{17} W/cm^2 the Landau damping (Eq. 3.39) is equal to the maximum of the homogeneous

growth rate $(k_o v_{\text{osc}}/4)$ on the thin clover-leaf-shaped curve. Electron plasma waves with wavevectors outside of this curve have negative growth rate, i.e. are not amplified by the instability. Inside the curve the Landau damping rate decreases rapidly, so it is negligible there. Consequently, Landau damping is not important for the present conditions. The rough estimation of Landau damping at 1 keV temperature gives a criterion for undamped plasma waves $\widetilde{k}_e < 3.4$ in good agreement with the previous curve. The collisional damping estimated from Eq. 3.38 is much smaller than the homogeneous growth rate, so it will be neglected. This analysis has shown that three-halves harmonic can be generated by TPD plasmons without propagation in the $0.2n_c$ - $0.25n_c$ density range. However, $3\omega_0/2$ will not be generated everywhere in the k space where it is predicted by the previous analysis, because the analysis does not deliver information about the growth rate and hence the amplitude of the plasma waves.
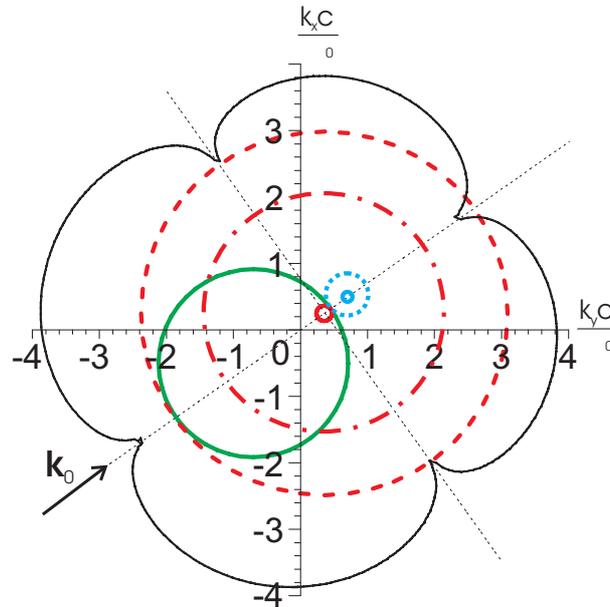
Figure 5.12: k space analysis of the instabilities. The thin dotted axes are the axes of a new coordinate system at the quarter critical adapted for the case of 45° incidence angle. Note that due to refraction the laser wave vector at $n_c/4$ ($\mathbf{k}_0$) is inclined by an angle of 55° with respect to the k_x-axis, which is parallel with the electron density gradient. The Landau damping is equal to the homogeneous growth rate on the thin clover-leaf-shaped curve at 10^{17} W/cm². Plasma waves with wave vectors on the thick green 'radiation circle' can generate $3\omega_0/2$ with the incident laser. The thick red curves are TPD circles for three electron densities. The small solid circle is for an electron density of about $0.25n_c$, the middle dashed-dotted circle for $0.23n_c$ while the larger dashed circle about $0.2n_c$ at 1 keV. The light blue curves are SRS generated plasma waves at $0.245n_c$ (smaller) and $0.2n_c$ (larger).

To account for the plasma wave amplitude and to complete theoretical description the growth rate is included. In Fig. 5.13 two 'radiation circles' are shown. While on the green solid circle a $3\omega_0/2$ photon is generated by coupling an incident photon and a plasmon, on the dashed circle a photon reflected from the half critical density is coupled to a plasmon. A large reflection is estimated, therefore the reflected light will contribute substantially to the $3\omega_0/2$ production. A significant amplitude of the plasma wave is expected in the k space, where the temporal growth rate is maximal. The red curves are the calculated maximum growth rate hyperbolas Eq. 3.37. The $3\omega_0/2$ radiation is predominately emitted into the directions given by the intersections of the maximum growth rate hyperbolas and the 'radiation circles'. The black intersections yield a maximum between $-20°$ and $-37°$ where refraction has been taken into account. The dark yellow intersection indicates a maximum between $55°$ and $71°$. Both predictions agree very well with the observed angular dependence (see Fig. 5.7, 5.8, 5.9, and 5.11). The $3\omega_0/2$ is *directly generated* with two incident photons at the lower black intersection point ($k_x c/\omega_0 = -1.8; k_y c/\omega_0 = 0$), while it is *indirectly generated* with an incident and a reflected photon at the upper black intersection ($-0.7; 0.1$) and at the dark yellow intersection ($0.2 - 1.2; 0.6 - 0.7$). The gray intersections generate back reflected light but no measurement was performed in this direction.

SRS may in principle also generate $3\omega_0/2$ radiation. SRS can generate plasmons at the quarter critical density and these plasmons have about the same wave vector as the incident photons. After coupling to an incident laser photon the wavevector of the generated radiation is $2k_0$, but the $3\omega_0/2$ has a wavevector of $\sqrt{8/3}k_0 \approx 1.63k_0$ at this density, Fig. 5.14 (a,b). Under these conditions the coupling process is not possible. However, coupling is possible in oblique incidence ($45°$ as in the experiment) between the plasmon and a reflected photon as shown in Fig. 5.14 (c,d). The generated $3\omega_0/2$ photon will have a wavevector perpendicular to the density gradient and will leave the plasma at $-71°$ due to refraction which is the direction of the second measured peak. The results of a more detailed analysis, leading to Eq. 3.34, are shown in Fig. 5.12 and 5.13. The smaller light blue 'circle' denotes plasmons generated by SRS at $0.245n_c$ and the larger light blue dashed curve at $0.2n_c$. The smaller curve indicates indirect, while the larger one direct and indirect $3\omega_0/2$ generation. The SRS growth rate reaches its maximum at a density around the quarter critical density Eq. 3.29. Taking the TPD and SRS maximal homogeneous growth rates as a measure of the generated plasma wave amplitudes. Near to the $n_c/4$ both of them reach a value of about $k_0 v_{\text{osc}}/4$. Thus, it is not possible to decide whether TPD or SRS is responsible for $3\omega_0/2$ production. The momentum conservation is the reason why $3\omega_0/2$ was always created by TPD plasma waves in the long pulse experiments. An angle of incidence of $45°$ and a very short scale
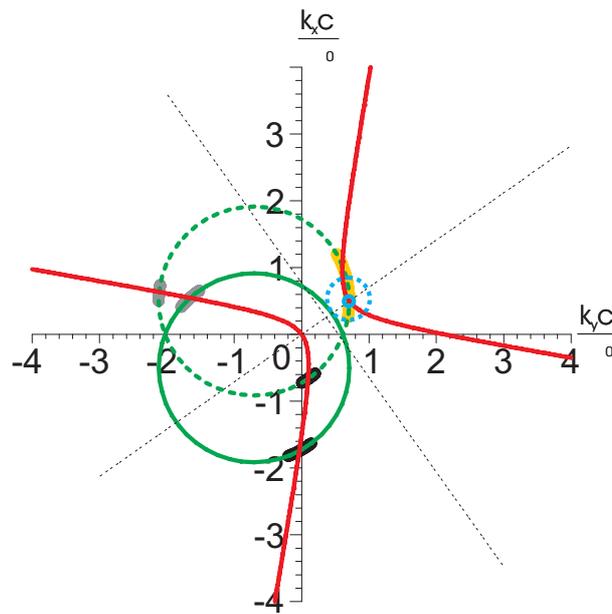
Figure 5.13: k space analysis of the $3\omega_0/2$ generation. The thin dotted axes are the axes of the new coordinate system at the quarter critical in the case of 45° incidence angle. The green thick solid circle is the 'radiation circle' for the coupling of an incident laser photon with a plasmon, while the green thick dashed circle is for the coupling of a laser photon reflected from $n_c/2$ with a plasmon. Along the red thick hyperbola is the growth rate maximal for a homogeneous plasma. The arcs are the intersections between the 'radiation circles' and the hyperbola, representing plasma waves that dominates in the $3\omega_0/2$ production. The light blue curves are SRS generated plasma waves at $0.245n_c$ (smaller) and $0.2n_c$ (larger).

length are required to use SRS plasmons for $3\omega_0/2$ production, which is not the case for long pulses. A possible alternative experiment to generate three-halves harmonic by SRS is a cylindrical or spherical plasma with a maximal density lower than n_c and two laser pulses from different directions with an angle of 70° between them. Although it remains a challenge to distinguish between SRS and TPD generated light. This distinction may be accomplished for example by scanning the plasmon k space with Thomson scattering or by spectral measurements.
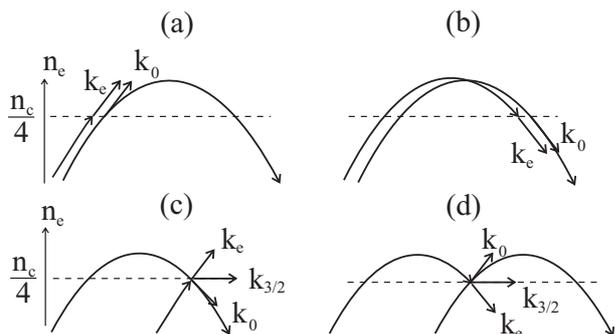
Figure 5.14: Coupling geometry of a SRS generated plasmon (wave vector k_e) and a fundamental laser photon (wave vector k_0) to form a $3\omega_0/2$-photon. In (a,b) a collinear coupling is shown, while in (c,d) k_e and k_0 are inclined by a certain angle.

Several factors will modify the previous discussion, such as (1) the plasma inhomogeneity, (2) the high plasma temperature, (3) the validity of plasma wave dispersion relation, (4) the high intensity, (5) the saturation of the instability, and (6) the plasmon propagation.

(1) In an inhomogeneous plasma the maximum growth rate is along the hyperbolas as indicated in Fig. 5.13, but the value is decreased corresponding to Eq. 3.25. Therefore, the TPD does not grow if the plasmon's wavevector is located directly near the axis of the adapted coordinate system (dotted lines in Fig. 5.12 and Fig. 5.13) which is parallel to $\mathbf{k}_0$. However, propagation compensates for that effect.

(2) The higher the plasma temperature the larger is the density range where TPD takes place, and the approximation that the decay takes place exactly at the quarter critical becomes void [117]. The weight of the k^2 term in the plasma wave dispersion relation grows, which leads to the next point, its validity.

(3) It should be noted that the TPD can occur with a reduced gain *nonresonantly* if only the energy and momentum conservation is fulfilled but not the dispersion relation [117]. That is, TPD can generate plasmons at a given density and temperature whose wavevectors are not located on the TPD circle in our analysis. This effect modifies the calculated spectrum of the three-halves harmonic radiation also along the 'radiation circles', which is estimated from this analysis. Nevertheless, the maximal growth is expected along the hyperbolas shown in Fig. 5.13.

(4) Above 10^{16} W/cm^2 the dispersion relation is not always satisfied and at relativistic intensities above 10^{18} W/cm^2 new nonlinear processes start to play a more and more dominant role [80, 81]. Second order stimulated Raman harmonic generation at the quarter critical leads directly to $3\omega_0/2$ and plasmon production. Two laser photons are simultaneously absorbed and a $3\omega_0/2$ photon and a plasmon are generated. Third order stimulated electromagnetic harmonic generation may create two $3\omega_0/2$ photons from three absorbed laser photons. These nonlinear processes are not important in our measurements, as the intensity was mostly under 10^{18} W/cm^2, but above this intensity they could contribute to the signal.

(5) Areas in k space with maximal growth determine the emission direction of the $3\omega_0/2$ generation. It is expected that this is slightly modified by saturation because areas with smaller growth rates generate proportionally more $3\omega_0/2$ with than without saturation. An increase in the width of both peaks in the angular distribution is observed with higher laser intensity (Figs. 5.7, 5.8, 5.9), which may originate from saturation.

(6) The propagation did not play an important role in the long pulse regime, because

collisional damping of plasma waves made the propagation length and thus the change in wavevector negligible. On the other hand, a short propagation distance leads to a large density and wavevector change in the short scale length experiments. Hence, the propagation of plasma waves is an important issue that may influence significantly the plasmon amplitude in the k space. The propagation in the k space is a translation of the plasmon wavevector opposite to the direction of the density gradient (in -x direction). During the pulse duration the change in the x component of the normalized wavevector is between 1 and 2 depending on the scale length ($L/\lambda \sim$ 5.5 - 2) starting from an original wavevector of 1, Eq. 3.36. This effect will elongate the maximum growth region into the -x direction in the k space. Even if the instability growth rate at the lower arc of the black circle in Fig. 5.13 is very low $3\omega_0/2$ generation may be possible due to plasmon propagation. At the other arm of the hyperbola the propagation mixes the TPD and SRS generated plasma waves. An originally by TPD produced wave will be amplified as it propagates and as its wavevector approaches $\mathbf{k}_0$ SRS will be the dominant amplification process. Due to the 45° angle of incidence the plasma waves propagate on one arm of the hyperbola and are exposed to the maximal growth continuously during the laser pulse.

These effects will not change the predicted angular distribution but they will affect the relative amplitudes and the spectral characteristics as a function of the observation angle. The possibility that the reflected fundamental will drive an instability is not discussed above, but again this will not change the angular distribution. The $3\omega_0/2$ generated in this way will propagate in the direction of the previous peaks [1].

Some effects will change the plasma geometry. These are (1) the hole boring, (2) other ponderomotive effects, and (3) the horizontal focus shift.

(1) The light pressure at the turning point pushes the inhomogeneous plasma towards the higher density region. This hole boring effect can lead to ultrahigh plasma acceleration [119, 120] and change the angular distribution of the fundamental [42, 121], which affects the distribution of the measured harmonics. The depth of the hole and the subsequent defocusing are estimated and the results indicate that both mechanisms have no measurable effect on the angular distribution of reflected fundamental light due to the short pulse duration [50, 121]. For the highest intensities, the angular broadening reaches the angular width caused by diffraction at the end of the laser pulse. This is supported by the angular distribution measurement of the fundamental with an intensity of 6×10^{18} W/cm^2 plotted in Fig. 5.6, where the horizontal angular width is determined by the focusing.

---

[1]Furthermore, it should be noted that resonance absorption is maximal for three-halves harmonic radiation propagating at an angle of 20° into the target. Therefore the TPD induced by the reflected light that generates $3\omega_0/2$ in this direction, can be neglected.

(2) The ponderomotive force changes the electron density not only at the reflection point but also below that density due to the generated standing wave. This in turn influences the scale length at the quarter critical density [122]. The radial ponderomotive force leads to channel formation by pushing electrons away from the middle of the beam. The developed space charge pulls on the ions. These effects are connected to ion motions and require a much longer time scale than the applied 100 fs or need a much longer plasma than the generated one in the experiments.

(3) The incident and reflected beams do not always spatially overlap at the quarter critical density. A horizontal focus shift due to the oblique incidence prevents the beams from overlapping (Fig. 5.15). Here, an exponential plasma density profile is assumed $(n_0 \times \exp(-x/L))$ with a scale length L and a beam diameter D. The horizontal focus shift is approximately $3.5 \times L$. The Rayleigh range is larger than the path length in the plasma from $n_c/4$ to $n_c/2$ and back so a constant beam diameter was used. The two peaks in the $3\omega_0/2$ angular distribution are originating from regions in the k space, where incident and reflected beams coincide, i.e. along the dashed circle in Fig. 5.13. This overlap and the dashed circle in Fig. 5.13 and so the direct $3\omega_0/2$ generation is prevented in a 'long' scale length, which is achieved in the experiments (Fig. 5.9 and 5.11). The horizontal shift might also explain why for scale lengths longer than 4λ the $3\omega_0/2$-yield is decreasing and the angular characteristic completely changes.
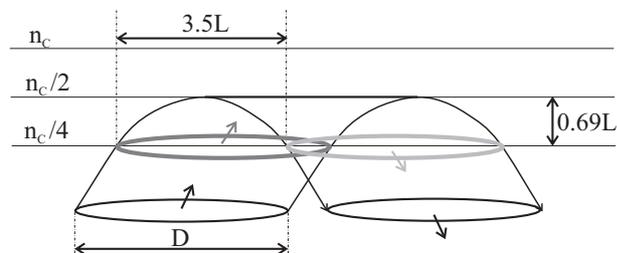
Figure 5.15: Horizontal focus shift in the case of 45° incidence angle and an exponential plasma density profile with scale length L and beam diameter D.

The $-25°$ peak is larger than the other peak in $-70°$ direction. There are two reasons for this. First, both direct and indirect $3\omega_0/2$ generation mechanisms are important in $-25°$ and only indirect process takes place in $-70°$. Second, the reflected light has smaller intensity due to resonance absorption, which decreases the efficiency of the indirect process.

The observed decrease in the $2\omega_0$ signal with growing scale length can be explained assuming that the second harmonic is produced at the critical density. The laser light tunnels from the reflection point at $n_c/2$ to n_c, where the $2\omega_0$ is generated. The tunneling distance between $n_c/2$ and n_c increases with the scale length and therefore the fundamental and the $2\omega_0$ intensity are decreasing.

5.5   Spectral measurements

Very detailed spectral measurements were performed. It is very difficult to calculate the spectrum for a given geometry, but it looks realistic to compare the main features as carrier wavelength and bandwidth as a function of the scattering angle with the theoretical predictions. Therefore the spectra of the fundamental and the three-halves harmonic radiation were measured in various directions.

5.5.1   Experimental results

Fig. 5.16 shows the spectrum of the incident fundamental (thin red curve) and the spectrum of the reflected laser light measured at an intensity of 7×10^{16} W/cm^2 and a 50 ps prepulse in $-12°$ direction. The spectrum measured through the fiber and averaged over 25 shots (thick black line) is slightly blue shifted by 2 nm, which was the typical error by the spectral measurements, and the bandwidth is 16 nm. The spectrum through the window and averaged over 5 shots (dashed thin blue line) is almost identical with a blue shift of 2 nm and a bandwidth of 19 nm, indicating that nonlinear effects in the fiber are negligible. The results show that the laser spectrum does not change drastically upon reflection, that is, the spectrum is neither wavelength shifted nor substantially broadened. Thus, the $3\omega_0/2$ spectrum is generated from the original laser spectrum and not a shifted or broadened one, at least for intensities up to about 10^{17} W/cm^2. Similar observations were made in $-45°$ and $-70°$ directions. In $-45°$ a much higher signal was detected, as expected from the angular distribution.
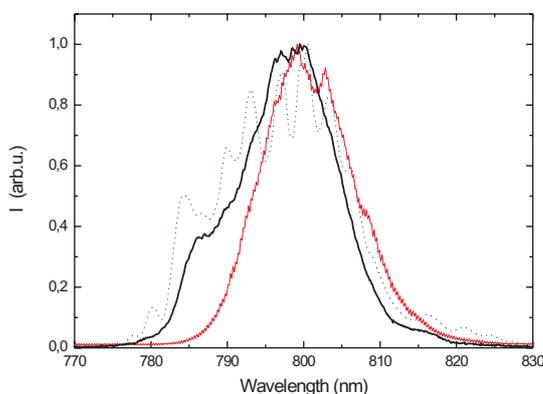
Figure 5.16: The spectrum of the incident and in the -12° reflected laser light for a laser intensity of 7×10^{16} W/cm^2. The thin red curve is the incident spectrum, the thick black curve is the reflected spectrum measured through a glass fiber, averaged over 25 shots and the dashed thin blue curve is the reflected spectrum when the scattered light propagated only through a 1 cm glass window, averaged over 5 shots.

The $3\omega_0/2$ spectra were averaged over at least 200 shots. The results at an intensity of 7×10^{16} W/cm^2 and a 50 ps prepulse are shown in Fig. 5.17 as a function of the scattering angle. The spectrum in the $-12°$ direction is blue shifted by approximately

12 nm and has an unexpectedly large 40 nm bandwidth. In $-45°$ and $-70°$ directions a smaller bandwidth of 18 nm is recorded and the spectra are red shifted by 2 nm and 5 nm, respectively. Obviously, the red shift increases with the observation angle.
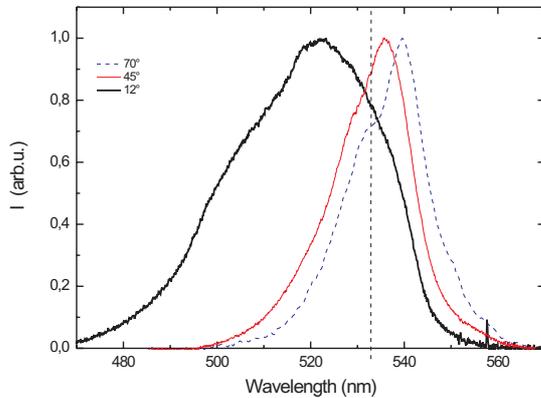

Figure 5.17: The spectrum of the three-halves harmonic radiation with a laser intensity of 7×10^{16} W/cm^2 in -12° (thick solid black line), in -45° (thin solid red line) and in -70° (thin dashed blue line). The dashed vertical line marks the exact $3\omega_0/2$ wavelength. All curves are normalized to its maximum value for better comparison. The strongest emission was found to be in -12° in agreement with the previous measurements.

At higher intensities, i.e. 4×10^{17} W/cm^2, but otherwise identical conditions the $3\omega_0/2$ spectra are shown in Fig. 5.18. Similar to lower intensities the red shift increases with the observation angle, i.e. the shifts are -11 nm, -1 nm, and 15 nm in $-12°$, $-45°$, and $-70°$ directions, respectively. However, for all angles the bandwidth is broadened to (46 ± 1) nm.
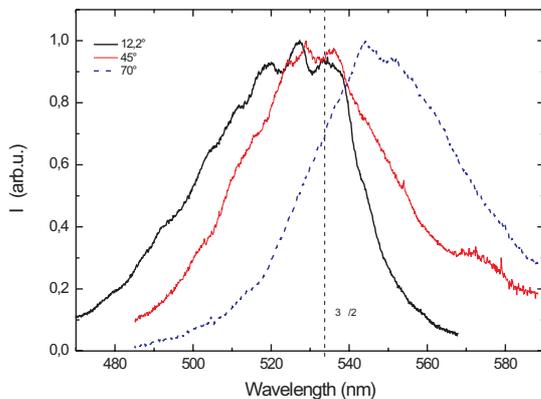
Figure 5.18: The spectrum of the three-halves harmonic radiation with a laser intensity of 4×10^{17} W/cm^2 in -12° (thick solid black line), in -45° (thin solid red line) and in -70° (thick dashed blue line). The dashed vertical line marks the exact $3\omega_0/2$ wavelength. All curves are normalized.

In Fig. 5.19 the measured wavelength shifts are plotted as a function of the angle for different intensities and prepulse main pulse delays. The black straight line is a guide to the eye. Practically no intensity dependence of the wavelength shift was observed and the measured shifts depend weakly on the scale length. The FWHM spectral bandwidth of the $3\omega_0/2$ radiation is shown in Fig. 5.20. Here, a clear intensity dependence is observable. Broader spectra are recorded at higher intensities which indicated a highly saturated instability for long pulses [104, 123] in all directions. A summary of the spectral measurements is shown in Fig. 5.21.
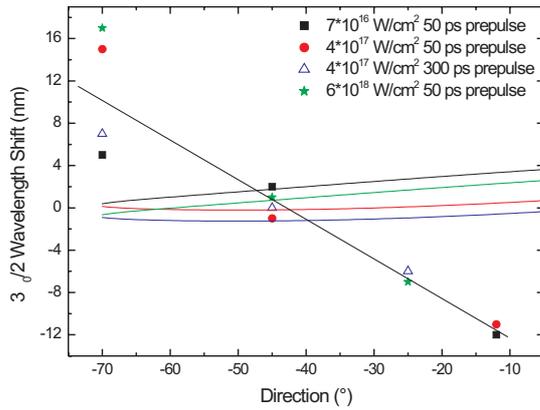
Figure 5.19: Spectral shift of the three-halves harmonic radiation with different laser intensities and a 50 ps prepulse (and 300 ps prepulse with 4×10^{17} W/cm^2 intensity). The black straight line is a guide to the eyes. The estimated wavelength shifts along the 'radiation circles' with 45° angle of incidence and 1 keV electron temperature are also plotted (details are in the text).
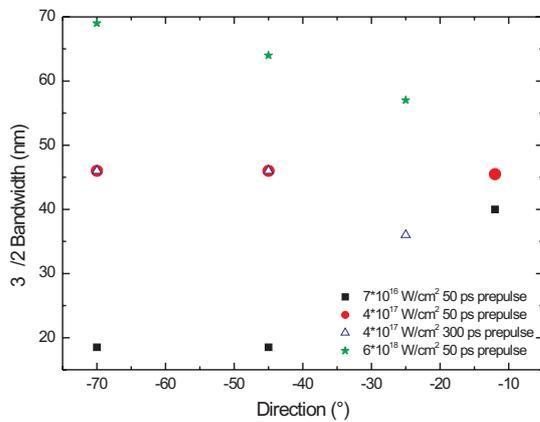

Figure 5.20: FWHM bandwidth of the three-halves harmonic spectrum with different laser intensities and a 50 ps prepulse (and 300 ps prepulse with 4×10^{17} W/cm^2 intensity).
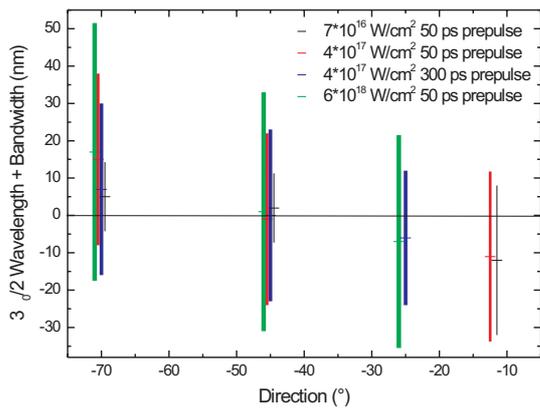
Figure 5.21: Summary of the three-halves harmonic spectral measurements with different laser intensities and scale lengths. The middle wavelength and the FWHM range is plotted for the measured spectra.

5.5.2 Discussion

The observed emissions from the plasma with increasing intensity and 800 nm wavelength can be explained qualitatively. Only second harmonic blue light is generated bellow the threshold of the instabilities. When the intensity reaches the TPD threshold more

and more green $3\omega_0/2$ light is produced. This threshold was $\sim 10^{16}$ W/cm^2 in the experiments. Just above the threshold green is observed in specific directions, while in others the plasma emits blue light. This picture changes with growing intensity or a large preplasma and green becomes the dominant radiation from the laser-plasma interaction. As the laser intensity increases the bandwidth of the $3\omega_0/2$ radiation broadens and at around 4×10^{17} W/cm^2 and above it appears to be white. This is the reason for the different colors from the plasma with different intensities, which certainly depends on the laser wavelength.

Spectral changes may be estimated quantitatively from the k-space analysis. In the case of resonant instabilities the energy of a TPD plasmon as a function of the wavevector can be calculated and so the carrier wavelength of the $3\omega_0/2$ spectrum is simply obtained. The spectral shift of the $3\omega_0/2$ radiation originating from the TPD plasmon shift as a function of the plasmon wavevector,

$$\Delta\lambda = 3.9 \times 10^{-3} T_{\text{keV}} \lambda_{3/2} \left(\frac{\mathbf{k}_0 c}{\omega_0} \frac{\mathbf{k}c}{\omega_0} - \frac{3}{8} \right) \tag{5.1}$$

where $\mathbf{k}_0$ is the wavevector of the laser at $n_c/4$, T_{keV} is the electron temperature in keV, and $\lambda_{3/2}$ is the unshifted $3\omega_0/2$-wavelength. Expressing the plasmon wavevector as a function of the scattering angle of the three-halves harmonic radiation the expected spectral shift from the most simple model (unsaturated, resonant TPD instability neglecting plasmon propagation) can be determined. The spectral shift from this analysis (see Fig. 5.19) is a decreasing red shift with increasing angle reaching a blue shift in the $-70°$ direction in contrast to the measurements. In Fig. 5.19 the thin black solid line represents the calculated wavelength shift for the lower part of the 'radiation circle' with an incident photon (green solid line in Fig. 5.13) and the thin red solid line for the upper part of the 'radiation circle'. The green and blue lines are calculated for the the other 'radiation circle' (dashed green line in Fig. 5.13) where a $3\omega_0/2$ photon is generated by a reflected laser photon and a plasmon. Completing this model with plasmon propagation yields a small $(2 - 3$ nm$)$ extension of the spectra in the blue, which can also not explain the results. The maximal Doppler shift, was estimated above, is much smaller than the observed shifts and bandwidths. Obviously, the theoretical predictions with TPD, plasmon propagation and Doppler shift cannot explain the observed spectral shifts and it is concluded that other wavelength shifting mechanisms are dominant, such as saturation (which influenced the spectra essentially in the long pulse regime) or the validity of the dispersion relation (nonresonant process). Similar broad, intensity dependent spectral bandwidth was noticed already in SRS reflectivity measurements without interpretation

[33], others attributed this feature to strongly coupled SRS [32], which means that the temporal growth rate exceeds the plasma frequency. Although strong coupling cannot take place in the described experiments due to the high plasma density at which three-halves harmonic is produced. The spectrum in $-70°$ with 7×10^{16} W/cm² and 4×10^{17} W/cm² and 50 ps prepulse is almost only red shifted as expected from SRS. In the other cases in $-70°$ the focus shift diminish the SRS generated $3\omega_0/2$ signal.
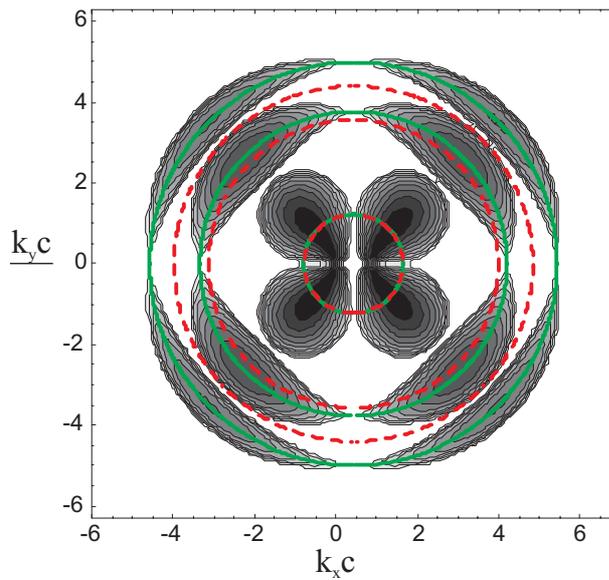
Figure 5.22: Growth rate obtained by solving Eq. 3.16 with 1 keV temperature, 7×10^{16} W/cm² perpendicular incidence and $n_e/n_c = 0.24$ plasma density for the innermost, 0.17 for the middle and 0.1 for the outermost curve. The red dashed circles are the TPD circles calculated using Eq. 3.33 and the green solid circles are the exact TPD circles.

To account for the nonresonant process the TPD instability dispersion relation (Eq. 3.16) must be solved for the complex ω. This equation is valid in homogeneous plasmas, therefore a simplified geometry with perpendicular incidence can be used. The effect of inhomogeneity is negligible much above threshold, which was the case during the spectral measurements. There are various parameters as the laser intensity, the plasma temperature, the plasmon wavevector and the plasma density in this equation. The homogeneous growth rate is plotted in Fig. 5.22 obtained from Eq. 3.16 using 1 keV temperature, 7×10^{16} W/cm² intensity and three different electron density values ($n_e/n_c = 0.24; 0.17; 0.1$). The conservation laws for TPD prescribe a circle for the plasmon wavevector at a given electron density (red dashed circles in Fig. 5.22 calculated from Eq. 3.33) as was discussed in Sec. 3.6. The width is in this case determined by the laser bandwidth. The green solid curves are the exact TPD circles. It can be seen in Fig. 5.22 that the growth rate is maximal along these circles, but does not vanish in their vicinity where the instability takes place nonresonantly (the plasmons do not satisfy their dispersion relation). The growth rate as a function of the plasmon frequency from this model is shown in Fig. 5.23 for 2×10^{16} W/cm² (left) and 10^{18} W/cm² (right) intensities, 1 keV temperature and four different electron densities, although the dispersion relation and therefore this TPD

model looses its validity at low densities so the $n_e/n_c = 0.1$ curves are only for the sake of completeness. The aim of this TPD model is to explain the three-halves harmonic
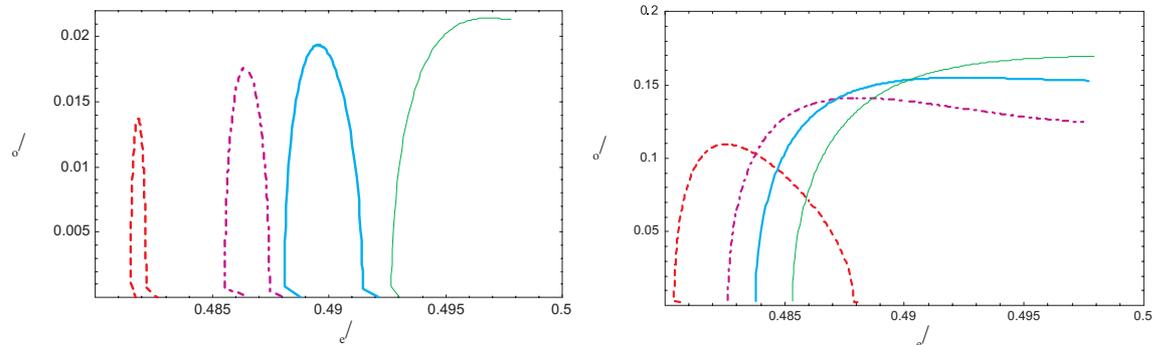

Figure 5.23: The TPD growth rate at an intensity of 2×10^{16} W/cm^2 (left) and 10^{18} W/cm^2 (right), 1 keV temperature and an electron density of $n_e/n_c = 0.1$ red thick dashed line, 0.17 purple dashed-dotted thick line, 0.2 blue solid thick line and 0.245 green solid thin line.

spectrum in $-25°$ direction. The intensity, plasma density and temperature are constant in the calculations, and the plasmon wavevector is running along the maximum growth rate hyperbola from the origin to the lower thick black arc in Fig. 5.13. This corresponds to the plasmon propagation similarly to the experiment. The abrupt cutoff is caused by the limit in the plasmon wavevector as it starts in the origin and runs in the negative direction. Temporal effects will smooth it. The measured $3\omega_0/2$ corresponds to the calculated curves between 0.2 and $0.25n_c$ and therefore has a spectra from 0.488 to 0.498 at 2×10^{16} W/cm^2 intensity and from 0.484 to 0.498 at 10^{18} W/cm^2. Important consequences from this calculation are that the growth rate grows with the root of the intensity, the growth decreases strongly with the density and the bandwidth of the radiation changes weakly with the intensity.

Nonresonant SRS could explain the spectra in $-70°$ direction, therefore calculations were made using Eq. 3.28 with only the down shifted D_{1-} part and 1 keV temperature. The coupling of TPD and SRS is not included in these calculations. The results are plotted in Fig. 5.24 applying 2×10^{16} W/cm^2 (left) and 10^{18} W/cm^2 (right) intensity and four different electron densities. Here k runs parallel with the laser wavevector during the calculations. There are typically two curves at a given density. The larger corresponds to back and the smaller to forward scattering. In the vicinity of the quarter critical density the two curves become connected and the growth rate for forward and back scattering becomes comparable. Only at about $n_c/4$ can produces SRS plasmons that can generate $3\omega_0/2$. The plasmons are red shifted and the width of the normalized growth rate curve equals approximately the maximum of the normalized growth rate (see Fig. 5.24), $\Delta\omega_e \approx \gamma_0$. The growth rate increases as the root of the intensity, but also does
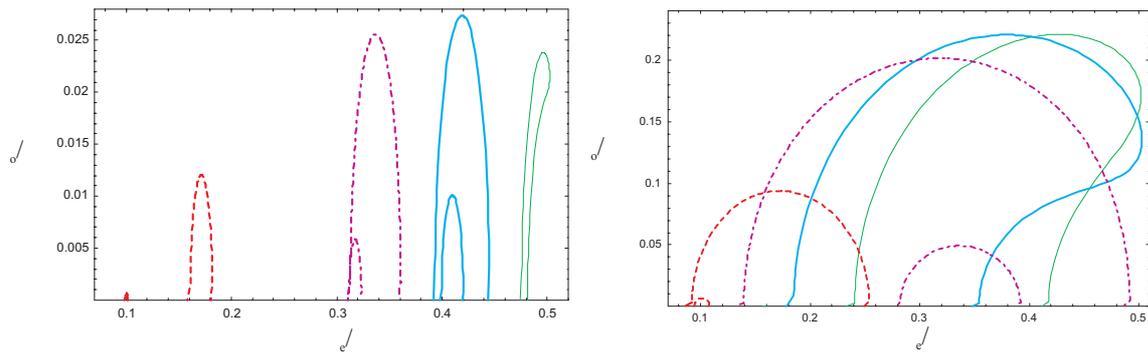
Figure 5.24: The SRS growth rate at an intensity of 2×10^{16} W/cm^2 (left) and 10^{18} W/cm^2 (right) for an electron density of $n_e/n_c = 0.01$ red thick dashed line, 0.1 purple dashed-dotted thick line, 0.17 blue solid thick line and 0.245 green solid thin line.

the bandwidth of the plasmons, which is a substantial difference to the TPD results.

The main conclusion of the nonsaturated instability growth rate calculations is that TPD generates plasmons with an intensity independent bandwidth in contrary to SRS, which generates strongly intensity dependent plasmon bandwidth. The bandwidth and the shifts of $3\,\omega_0/2$ radiation are only in qualitative agreement with the measured results. The inclusion of the saturation mechanism is expected to account more accurately for the spectral results. The shifts and bandwidth from SRS are reasonable for example: a bandwidth of $\Delta\lambda_{3/2} \simeq 14$ nm, 33 nm and 60 nm is obtained at an intensity of 7×10^{16} W/cm^2, 4×10^{17} W/cm^2 and 1.4×10^{18} W/cm^2 neglecting the laser bandwidth.

These results confirm qualitatively that SRS is responsible for $3\,\omega_0/2$ radiation in -70° direction (up to approx. -45°) and TPD for the -25° direction.

Chapter 6

Polarization and growth rate of $3\omega_0/2$

In this chapter experimental results about various properties of the $3\omega_0/2$ radiation is presented. Steep plasmas were used in the measurements similar to those used in the previous chapter. The measured properties complete the picture about instabilities obtained in the last chapter. The temporal characterization of the three-halves harmonic radiation is in the center of the investigations. Two independent measurement series were performed yielding similar experimental observations. The large amount of glass in the path of the harmonic beam influenced slightly the first results, therefore a control measurement was made with carefully chosen conditions.

The generation mechanisms are identified in Chap. 5, but there is almost no information about the saturation mechanism and whether the saturation is reached or not. It is expected that saturation appears in these experiments, but there is no clear evidence for it. Another open question is the importance of instabilities generated by the reflected laser pulse. It was neglected in the previous analysis without direct evidence. The results of this chapter try to answer these questions based on mainly experimental observations and not theoretical models, because there is no theory on this field and the long pulse models are not applicable.

There are several temporal investigations of the three-halves harmonic radiation in the long pulse regime. Although, the temporal resolution (20-40 ps) is generally not enough to resolve the short linear regime (10 ps) [69, 73, 91]. Therefore, in these measurements only the saturation regime was observed, which is completely different from the saturation in the femtosecond range. Meyer and Houtman used a 2 ns CO_2 laser and measured temporally the exponential growth with a streak camera having 2 ps resolution. They observed the growth rate as a function of the plasmon wavevector and got an astonishingly good fit with Simon's theory [67].

Experimental observations as the reflectivity of the aluminum plasma at the fundamental wavelength, the polarization properties and intensity dependence of the $3\omega_0/2$ will be reviewed at first. Then follows the presentation of the detailed pulse duration measurements. A short discussion closes this chapter.

6.1 Setup and plasma reflectivity

The applied laser parameters in the present experiments are the same as in Chap. 5 described in Sec. 5.1, therefore only the differences will be discussed here. An expansion of the beam diameter in the laser allowed a better focusability leading to a focal FWHM diameter of 2.3 μm and a Rayleigh range of about 15 μm during the second measurement. The energy on target was slightly less approx. 100-110 mJ so the average intensity was 6×10^{18} W/cm^2 also. The experimental setup is shown in Fig. 6.1. An incidence angle of 45° and -25° angle of observation were used for the three-halves harmonic measurements. The plasma radiation was collected with a second off-axis parabola mirror to avoid the
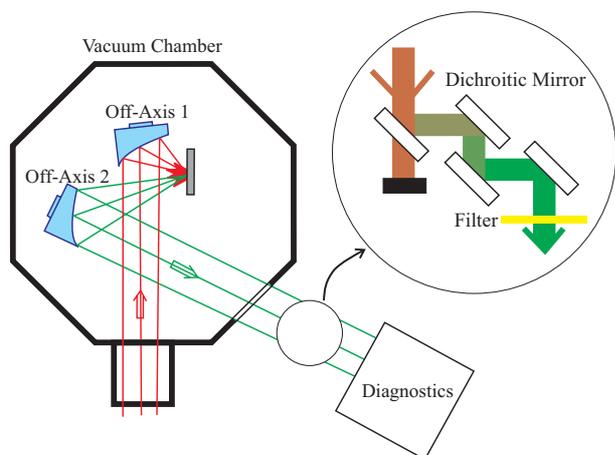

Figure 6.1: Setup of the autocorrelation measurements.

stretching in the lens and lead through a 3 mm / 1 mm thick BK7 window to the diagnostics (first / second experimental series). The fundamental and the second harmonic radiations must be filtered very accurately for the autocorrelation measurements, which was accomplished by 4 dichroic mirrors and a thin color filter in the first experimental series and with 6 dichroic mirrors in the second series. Applied diagnostics were linear polarizer with photodiodes, absolutely calibrated diodes or an SHG autocorrelator.

To clear the role of the reflected fundamental beam in the experiments the reflectivity of the plasma was measured. First the incidence laser energy in front of the target was obtained and than the reflected energy from the target as a function of the target focal position using 45° angle of incidence. The energy detector directed to the target provided

wrong values if directly exposed to Debris. To avoid this influence it was covered by a foil in the reflected energy measurements. To avoid undoubtedly the effect of Debris a reference measurement was made by inserting a second off-axis parabola mirror in the chamber and leading the light behind the target to the energy meter. The reflectivity defined as the reflected energy divided by the incident energy is shown as a function of the intensity in Fig. 6.2. As the reference curve does not deviate significantly from the
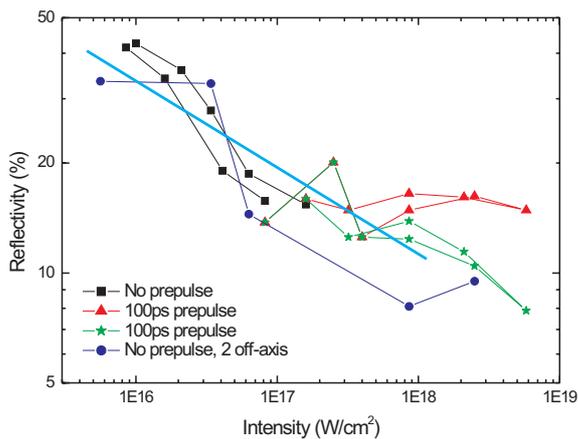
Figure 6.2: Reflectivity of Al plasma generated with and without a 100 ps prepulse as a function of the intensity. A shielded energy detector was placed in front of the target to measure the reflected laser energy. A reference measurement was made using a second off-axis parabola mirror and the energy detector placed behind the target. The light blue line is a guide to the eyes.

normal curve it is concluded that the influence of Debris is negligible with the shielded energy meter. The reflectivity determined without the prepulse is also similar to the results with a 100 ps prepulse showing a relative small effect of the larger preplasma in the absorption. The reflectivity is 35–40% at 10^{16} W/cm^2, 15–20% at 10^{17} W/cm^2 and only 10% at around 10^{18} W/cm^2 intensity. The most absorption is expected to take place at the reflection point therefore the intensity is so low at the quarter critical density that the generation of instabilities can be neglected near the incident beam. This justifies the assumption in the previous chapter that the reflected light produces negligible plasma wave amplitude.

6.2 Intensity dependence of the three-halves harmonic radiation

The first determined property of the three-halves harmonic radiation is the polarization degree. It was obtained by placing a linear polarizer foil in the path of the carefully filtered beam and measuring the transmitted signal with a photodiode. Although, the intensity suppression ratio of these polarizer films is only 10^{-2} it is sufficient for the presented experiments. A test measurement was made with a linearly polarized He-Ne laser as

shown in Fig. 6.3. The polarization degree (P) is defined as
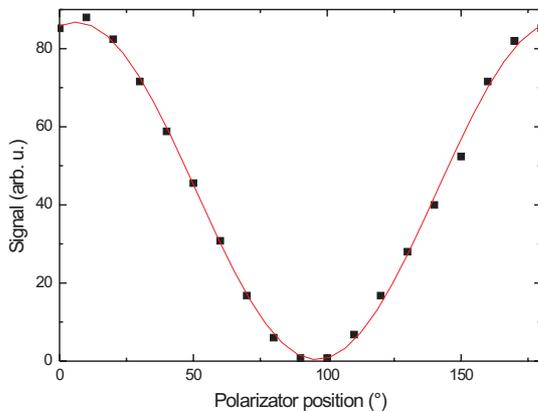
Figure 6.3: Polarization degree of a He-Ne laser. The measured signal through a linear polarizer as a function of the polarizer position. The red line is a fit yielding a polarization degree of $0.99 + 0.01 - 0.02$.

$$P = \frac{I_{\max} - I_{\min}}{I_{\max} + I_{\min}} \qquad (6.1)$$

where $I_{\max}$ and $I_{\min}$ are the maximal and minimal photodiode signals behind the polarizer as the polarizer is rotated by 180°. A completely linear polarized light has a polarization degree of 1 and an un- or circularly polarized has 0. Fitting a sine function with background onto the signal vs. polarizer position curve a polarization degree of $0.99 + 0.01 - 0.02$ is obtained for the He-Ne laser as expected. This provides 1–2% error of the method.

The $3\omega_0/2$ signal behind a polarizer as a function of the polarizer position is in Fig.6.4. The two independent curves indicate a partially polarized radiation [1]. The polarization degree is 0.29 ± 0.07 for the blue squares and 0.36 ± 0.03 for the red circles, i.e. 1/3 in average. In Fig. 6.4 the right picture is a polarplot of the results and the direction of the partial polarization is approximately perpendicular to the laser polarization (the green arrow in the figure). The partial polarization of the $3\omega_0/2$ radiation excludes the generation process involving only longitudinal plasma waves, i.e. three plasmon coupling [95]. Further work is needed for a better understanding this polarization degree.

In the following the $3\omega_0/2$ dependence on the laser intensity is in the center of the investigations to obtain information about the saturation behavior. The intensity was changed by two different methods (a) by varying the energy of the laser and (b) by changing the focal position of the target. In Fig. 6.5 the $3\omega_0/2$ energy is plotted as a function of the intensity from the second measurement series. The intensity was changed by controlling the incident laser energy. Small intensity steps have been used close to

---

[1]Although, this light can also be elliptically polarized taking into account the generation mechanism partial polarization is much more probable.
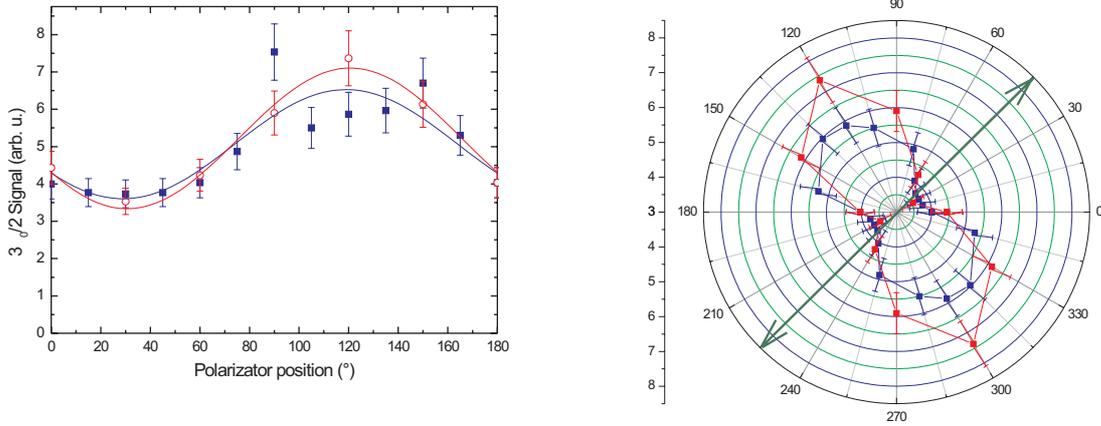
Figure 6.4: (left) Two independent measurements of the polarization degree of the $3\omega_0/2$ radiation. The measured signal through a linear polarizer as a function of the polarizer position. The solid lines are fits yielding a polarization degree of 0.29 ± 0.07 for the blue squares and 0.36 ± 0.03 for the red circles. (right) The results in a polar coordinate system. The green arrow shows the direction of the laser polarization.

threshold to explore the linear regime and the beginning of saturation. The signals were taken in three directions using a 100 ps prepulse and three photodiodes and compared in one point with an absolute calibrated photodiode. The blue curve is a guide to the eyes. There is no significant difference between the directions. All show a rapid increase
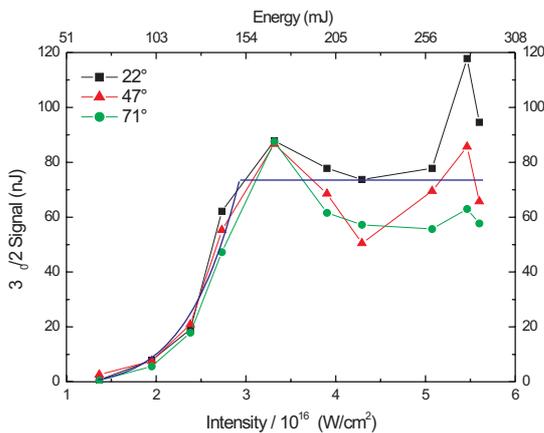

Figure 6.5: $3\omega_0/2$ energy as a function of the laser intensity with a 100 ps prepulse in different directions. The intensity was changed by varying the laser energy in front of the compressor as shown on the upper scale. The blue curve is a guide to the eyes.

of the three-halves harmonic and after that a saturated regime with practically constant signal. The next figure (Fig. 6.6) is a logarithmic plot of the previous results showing an exponential growth in the beginning and a constant later. In this figure new result are also presented taken without introduced prepulse. Nevertheless, 'internal' prepulses are present (Fig. 5.1). Laser characteristics such as the 'internal' prepulse structure has changed slightly from experiment to experiment and the beam diameter was improved,

therefore care must be taken by comparing the results with them in the previous chapter. It is expected that these 'internal' prepulses generate a preplasma with a scale length reaching the value of λ. As expected the signals without prepulse starts to grow at higher laser intensities. The signals in -47° direction have a larger background due to the reflected laser radiation. Although the beginning of the exponential growth is not measured, it can be seen that the amplification is minimum a factor of 300, i.e. an e-folding of 6 before saturation is reached.
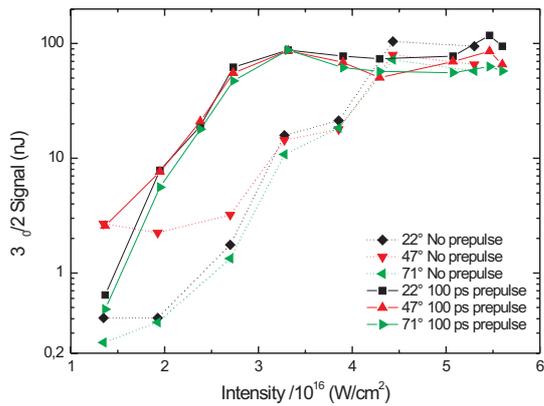

Figure 6.6: Logarithm of the $3\omega_0/2$ energy as a function of the laser intensity with and without a 100 ps prepulse in different directions. The intensity was changed by varying the laser energy.

In Fig. 6.7 the $3\omega_0/2$ and the x-ray signals are plotted as a function of the focal position taken in the first experimental series. The x-ray signal, which was taken with a GaAsP Schottky diode sensitive around 1 keV energy, is an increasing function of the laser intensity [124]. Therefore, the peak in the x-ray yield marks the position of the focus. As can be seen the $3\omega_0/2$ yield has a maximum and then decreases again as the target is shifted into the focus. An important consequence is that the target should not be in the focus for an optimal signal.
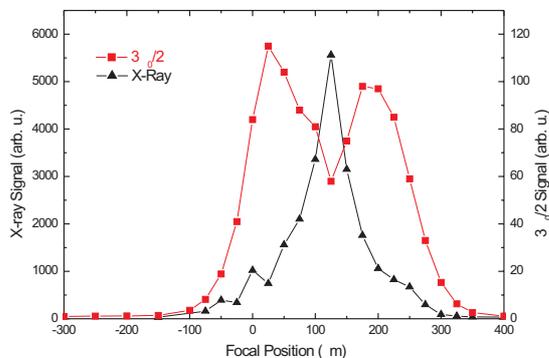

Figure 6.7: $3\omega_0/2$ and x-ray signals as a function of the focal position.

Similar behavior was observed during the second series. The three-halves harmonic signal as function of the laser intensity changed by shifting the target focal position is

in Fig. 6.8. First an increase of the signal and later a decrease is obtained at about
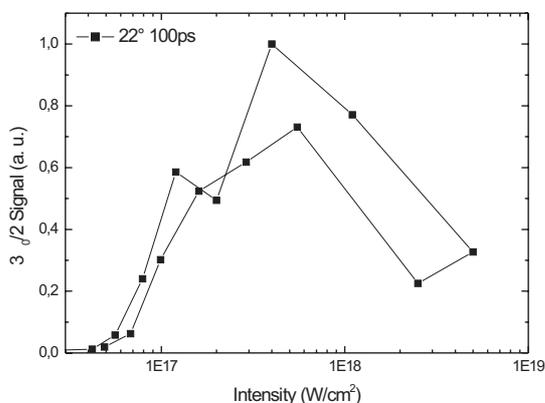
Figure 6.8: $3\omega_0/2$ signal as a function of the intensity with a 100 ps prepulse. The intensity was changed by varying the focal position.

3×10^{17} W/cm^2 intensity. This property is in agreement with the previous results ($3\omega_0/2$ vs. laser energy), because at a given intensity the signal per unit area becomes constant and a better focusing results in a smaller focus, consequently smaller signal.

6.3 Autocorrelation measurements on $3\omega_0/2$

The temporal characterization of the three-halves harmonic radiation will be discussed now. The difficulties are (1) the expected short pulse duration (approx. 100 fs), which makes linear measurement with an ultrafast photodiode invalid and therefore a nonlinear detection must be applied, (2) the large bandwidth (approx. 40 nm), which makes great demands upon the thickness of transmitting optical components and the nonlinear optical crystal, (3) the low pulse energy (approx. 100 nJ), which requires extreme sensitivity of the device, and (4) the large shot-to-shot fluctuation, which is more dramatic in the nonlinear signal used for the pulse duration measurement requiring a large number of points to average over or a discriminator to select incident pulses in a specific energy range. Considering these facts a specially designed multishot intensity SHG autocorrelator (AC) [125, 126] was prepared to measure the $3\omega_0/2$ pulse duration, shown in Fig. 6.9 [2]. The AC can support beams with almost 2 cm width and is equipped with a photomultiplier tube (PMT) to detect the second harmonic signal from the crystal. Therefore the energy sensitivity is very high. The thin BBO crystal and beam splitter support a large bandwidth. An off-axis parabola is used for the focusing to reach a smaller focus spot size

---

[2]Although, a cross correlation between the three-halves harmonic and the laser pulse delivers a signal linearly proportional to the harmonic signal, but the resolution is limited by the laser pulse duration. As the three-halves harmonic pulse can be shorter than the fundamental these type of investigations are limited in resolution.
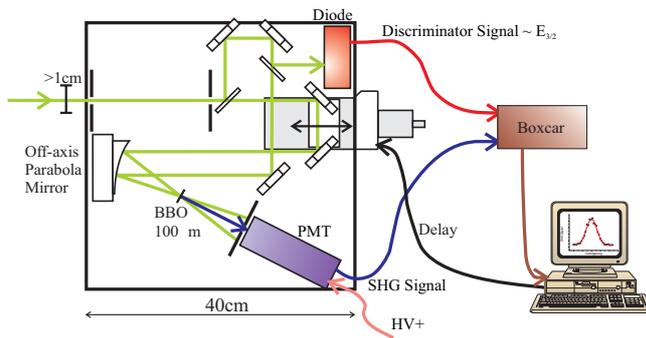
Figure 6.9: Multishot SHG autocorrelator (AC) used in the measurements. Special properties are the large supported beam diameter, the discriminator diode, the high sensitivity due to the photomultiplier tube (PMT) and the large supported bandwidth due to the thin beam splitter and BBO and to the focusing with off-axis parabola mirror.

and so further increase the sensitivity and to avoid material to propagate through. A reference signal can be used for discrimination to decrease the effect of fluctuation. The detector signals were read by a computer with the help of a sample and hold box. The delay stage was computer controlled and so the AC was completely automated to fasten the correlation measurements.

Numerous nonlinear processes take place to obtain an AC signal with the three-halves harmonic radiation. A schematic illustration of these processes and their dependencies can be seen in Fig. 6.10.
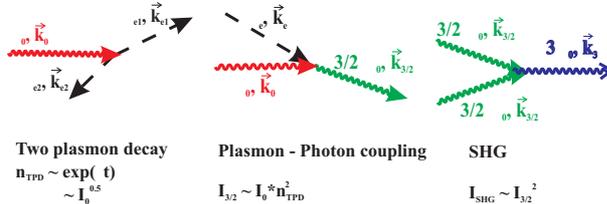

Figure 6.10: A schematic representation of the involved nonlinearities in the three-halves harmonic pulse duration measurements and their dependencies.

The energy sensitivity and the supported bandwidth of the AC were carefully tested with calibrated sources. Fig. 6.11 shows the signal of the AC as a function of the incident laser energy with a 514 nm source. The useful energy range of the device is approximately 1–10 nJ. At lower energies the PMT signal is suppressed by the background noise and at higher energies the PMT saturates. Between these limits the output signal in a log-log plot is fitted with a linear function. The fit delivers a slope of 1.97 ± 0.04 corresponding to the second harmonic generation in the AC. The PMT was operated with 800 V providing a large amplification.

The test of the bandwidth was performed with a 1 kHz broad bandwidth Vitesse oscillator ($\Delta\lambda \approx 31$ nm at 800 nm central wavelength). The crystal and the beam splitter were correspondingly aligned and changed for this wavelength. One representative AC trace in logarithmic scale is in Fig. 6.12. The fit assuming a Sech^2 pulse delivers 92 fs FWHM pulse duration, while a commercially available AC measured (86 ± 1) fs duration.
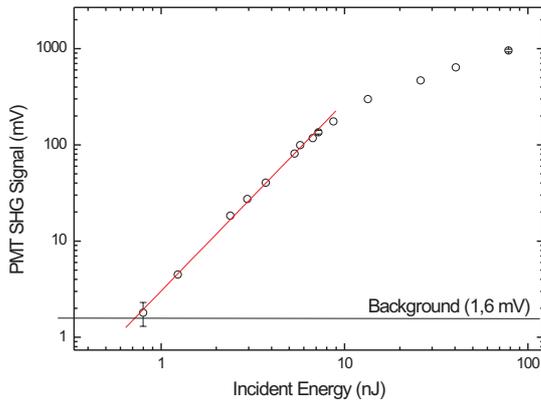
Figure 6.11: Measurement of the useful incident energy range of the multishot SHG autocorrelator at 800 V PMT voltage. The black horizontal line is the background (1.6 mV) and the red curve is a fit with a slope of 1.97 ± 0.04. Typical errors are indicated.

As the pulses were far from transform limited the effect of the 1 mm thick beam splitter and compensation plate can be estimated easily. Measurements introducing extra glass in the beam path and then extrapolation of the effect of the beam splitter yielded a pulse duration of 86–87 fs in perfect agrement with the reference.
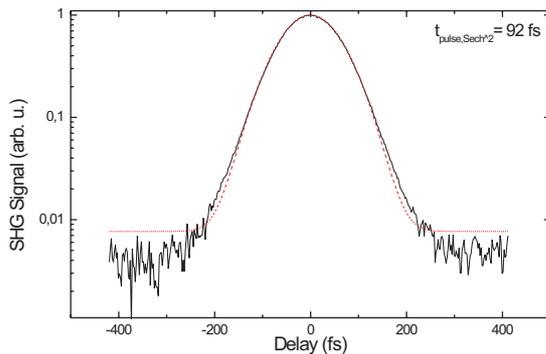

Figure 6.12: Test of the AC supported bandwidth using a Vitesse oscillator.

The test of the discriminator and the sensitivity is in Fig. 6.13. A dye laser with 514 nm wavelength was used for these investigations. A reference AC without discriminator provided more noisy traces with similar pulse duration (typically 593 fs). The measured pulse duration with the discriminator is 586 fs and the autocorrelation trace is unusually smooth from a dye laser. Consequently the correlator works satisfactorily with the discriminator.

The previous tests justify that the AC meets the requirements for measuring the duration of the three-halves harmonic radiation. In both measurement series several AC traces were taken at -20° direction with different conditions. Two of them are shown in Fig. 6.14 using a laser pulse duration of 286 fs. The laser pulse duration and the focal position of the target was changed (typically the target was far from the focus) in both series. The traces are promising taking into account the previous difficulties in
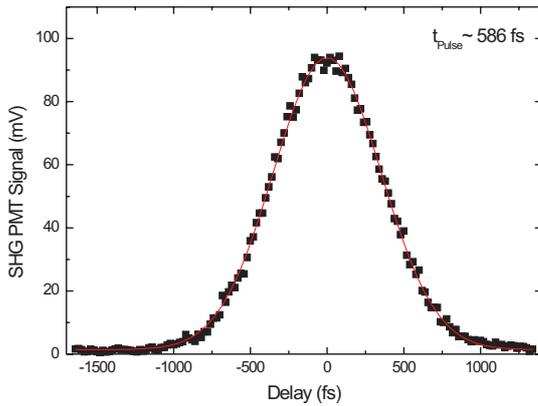
Figure 6.13: Test of the AC discriminator and sensitivity using 514 nm dye laser pulses with 7.7 nJ energy.
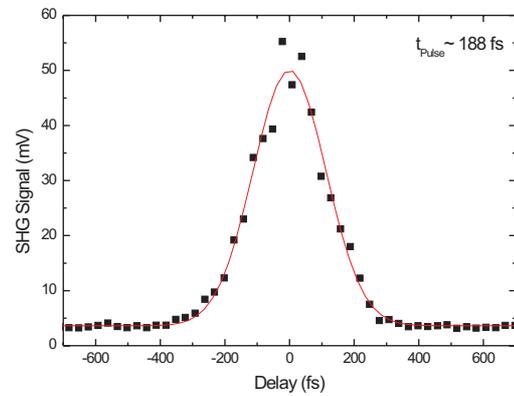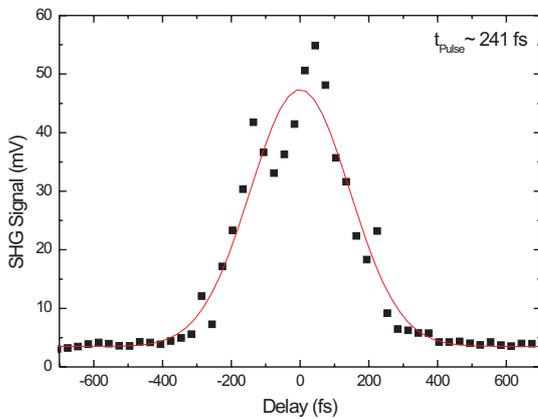

Figure 6.14: $3\omega_0/2$ autocorrelation traces taken without discriminator (left) and with discriminator (right). The incident laser pulse duration is 286 fs. The pulse durations are obtained assuming Gaussian pulseforms.

these experiments. Further analyzing the results it can be noticed that the pulse durations obtained with discriminator are generally shorter than without discriminator (also in Fig. 6.14). Therefore, at first the results without discriminator are presented. The first series $3\omega_0/2$ durations as a function of the incident laser length is shown in Fig. 6.15 and the second series in Fig. 6.16, where the red points are an average over all measurements with a given incident pulse duration and the error represents the standard error. In these figures all points represent an AC measurement. In both experiments the three-halves harmonic pulse duration depends weakly on the incident laser pulse duration, which is an important conclusion. The main difference between the two measurements is the unambiguously longer pulses in the first series. Taking into account the bandwidth of $3\omega_0/2$, the inserted materials into the beam from the target to the BBO crystal in the AC and the group velocity dispersion (GVD) of the materials a pulse elongation of about 100 fs,
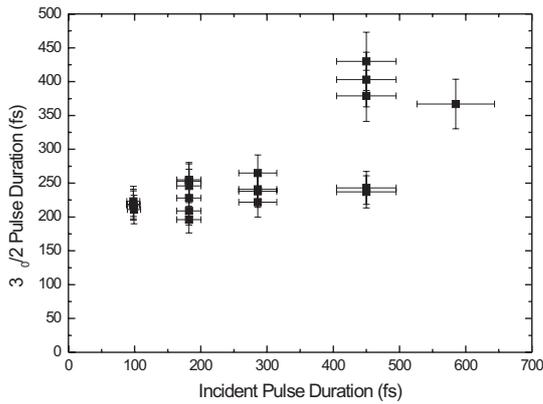
Figure 6.15: Summary of the $3\omega_0/2$ pulse duration measurements with different incident pulse durations during the first measurement series. The plotted results are made without discriminator. The errors are obtained from the fits.

25 fs can be calculated [127] for the first, second series, respectively [3]. Correcting for
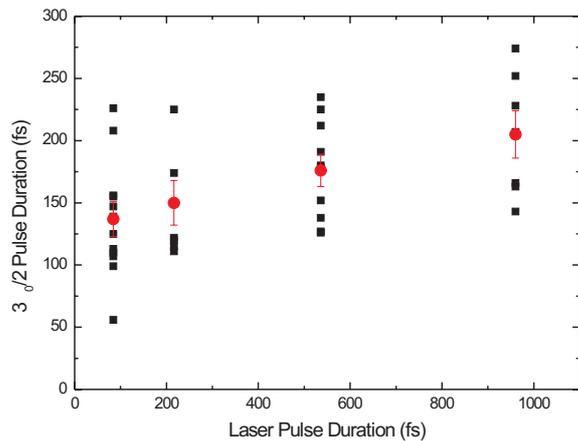

Figure 6.16: Summary of the $3\omega_0/2$ pulse duration measurements with different incident pulse durations during the second measurement series. The red points are an average over all measurements with a given incident pulse duration and the error represents the standard error. The plotted results are made without discriminator.

these GVD effects the two investigation series have similar results.

Results taken with discriminator in the first experiment are plotted in Fig. 6.17. The incident laser pulse duration was 286 fs and the intensity is about 5×10^{16} W/cm^2. The horizontal error bars represent the applied discrimination range, while the vertical errors originate from the Gaussian fit. Two measurements made without discriminator are separated by a thin black vertical line. The signal was very stable and very well reproducible during this measurement. One trace without discriminator was measured in the beginning and the other at the end of this investigation showing almost the same duration. At around 22 mV discriminator signal also two measurements certify the extraordinary reproducible results. In Fig. 6.17 a clear correlation between the $3\omega_0/2$ duration and $3\omega_0/2$ energy can be observed. It must be noted that all laser parameter were kept constant.

---

[3]The $3\omega_0/2$ pulses are not transform limited, which would mean a sub-30-fs length. Assuming a simply chirped pulse, i.e. only quadratic phase modulation, the elongation is not pulse duration dependent.

Therefore the longer the pulse duration, i.e. the time of the growth, the higher the energy. Based on the knowledge about instabilities and the results in this figure an exponential dependency is expected. In Fig. 6.18 the $3\omega_0/2$ intensity, i.e. the discriminator signal
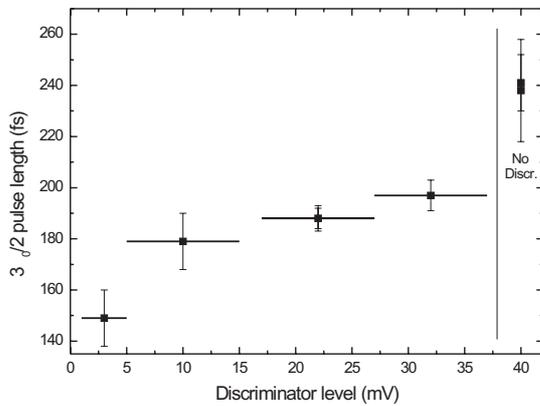

Figure 6.17: $3\omega_0/2$ pulse duration measurements with discriminator plotted as a function of the energy of the three-halves harmonic radiation. The horizontal error bars represent the applied discrimination range, while the vertical errors originate from the Gaussian fit. The thin black vertical line separates two measurements made without discriminator.

divided by the length of the pulse, is plotted as a function of the pulse duration. An exponential fit is also shown in the figure with an obtained growth time $[t_g = (2\gamma)^{-1}]$ of (22 ± 2) fs. Assuming linear regime, the growth rate can be calculated from Eq. 3.25 and yields $t_g =33$ fs at an intensity of 10^{16} W/cm^2, and 5 fs at 10^{17} W/cm^2 using $T_e=1$ keV and $L/\lambda=2$. In the second series similar observations were made with discriminator, although
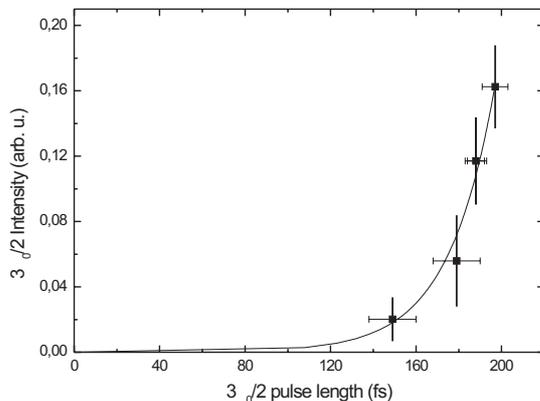
Figure 6.18: Intensity of the $3\omega_0/2$ radiation (the discriminator signal divided by the pulse duration) as a function of its pulse duration from Fig. 6.17. An exponential fit is also shown with 22 fs growth time. The vertical error bars represent the applied discrimination range, while the horizontal errors originate from the Gaussian fit.

the results were not as reproducible as the previous ones.

It should be noted that the $3\omega_0/2$ radiation is generated in a time interval when the laser intensity is higher than the threshold intensity for the instability. This interaction time can be much longer than the laser pulse duration, depending on the laser intensity. The observed results are a good basic for a novel model of saturation. Two main observed properties from various results are an exponential growth and a strong saturation that stops the rapid growth. As can be seen from Fig. 6.5 the energy of the $3\omega_0/2$ signal stays

approximately constant after saturation takes place. This can be explained when the signal grows exponentially until saturation and then simply disappears due to a saturation mechanism, which is shown in Fig. 6.19. The model predicts a similar temporal structure
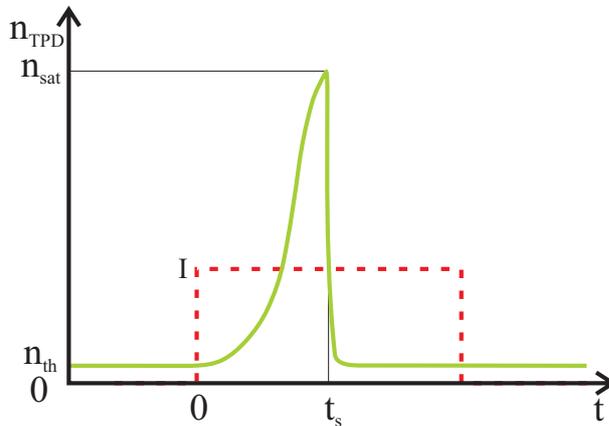

Figure 6.19: Suggested model of plasma wave saturation. The electron plasma wave amplitude (n_{TPD}) and the laser intensity (I) as a function of time. The time t_s marks the point where saturation (n_{sat}) is reached from the initial thermal noise (n_{th}) and τ is the pulse duration.

for the three-halves harmonic signal as for the plasma wave with a pulse duration ($t_{3/2}$) proportional to $(2\gamma)^{-1}$. Therefore the three-halves harmonic pulse duration will slightly increase with the incident laser length (τ) according to $t_{3/2} \sim \tau^{1/2}$, as observed in the experiments (Fig. 6.16). The $3\omega_0/2$ energy in the linear regime will increase exponentially as the intensity increases independently whether the intensity is changed by the laser energy or by the focusing.

This saturation behavior implies a decrease in the $3\omega_0/2$ signal vs. target focal position (Fig. 6.7) as already discussed due to the decrease of the spot size. It needs further experimental and numerical investigations to estimate the role of ponderomotive force that compresses the plasma and decreases the scale length, and whether this saturation can be the wavebreaking process.

The pulse duration with discriminator is generally shorter than without discriminator. It can be expected with exponentially growing signals. There are $3\omega_0/2$ pulses with longer duration and much larger energy according to Fig. 6.17. The difference in the second harmonic signal of the autocorrelator is even larger due to the nonlinearity. Therefore the average of the second harmonic over many shots is dominated by the largest pulses with slightly longer duration, similarly to statistics with an exponential distribution function. As the correlation without discriminator contains every shot, the duration of these intensive pulses is generally obtained. The application of the discriminator avoids this problem and the measurement gives the duration of the smaller pulses with shorter pulse duration.

Chapter 7

Summary

In this thesis, the first detailed investigations have been made on three-halves harmonic radiation generated in femtosecond-laser-produced plasmas. Several important properties of the parametric instabilities stimulated Raman scattering (SRS) and two-plasmon decay (TPD) in this regime have been deduced from the results with the help of theoretical models.

In the interaction of ultrahigh intensity Titanium:sapphire femtosecond laser with solid targets, a strong green light emission is regularly observed. This radiation is generally attributed to collective plasma effects and in particular to an emission at three-halves harmonic of the fundamental frequency ($3\omega_0/2$), which has previously been investigated only with nanosecond lasers. The purpose of this work is to systematically study the $3\omega_0/2$ emission from femtosecond-laser-produced plasmas, with the ultimate aim of identifying possible applications of this radiation source.

To this end, the work has been organised into 3 parts, each broadly representing a separate experimental campaign.

The first experiment was performed in long scale length plasmas similar to those occuring in the inertial confinement fusion context. An interferometric measurement revealed an electron density scale length of about 100 μm and suggested that ionization defocusing played an important role. It was confirmed with spectral measurements that the observed green light from the plasma was indeed $3\omega_0/2$ radiation. The energy-dependence of the three-halves harmonic emission on the laser pulse duration was then determined, and interpreted with the help of a model, which included the TPD instability and the coupling between a TPD plasmon and a laser photon. Very good agreement was found between the model and the measurements, from which one could infer two things: i) that

the laser intensity was about 10^{16} W/cm^2 in the plasma and ii) that the instability was dominated by the exponential growth, in complete contrast to the saturation-dominated ns laser regime.

An upgraded laser with shorter pulse duration and better focusability, i.e. higher intensity up to 6×10^{18} W/cm^2 was then used in a second series of experiments. Suppression of the prepulses led to a much shorter and controllable scale length in the λ–10λ range. Angularly and spectrally resolved measurements were made to identify the $3\omega_0/2$-generation process within this high-intensity regime. In a certain parameter range, a characteristic double-peaked angular distribution was obtained using 45° incidence angle. A detailed k-space analysis shows that the first peak at 25° is generated by the coupling of a TPD produced plasmon with a laser photon. A SRS-based plasma wave amplification is responsible for the second peak at 70° direction, although TPD also contributes to the amplification process. These results suggest that three-halves harmonic radiation was obtained from SRS the first time in this experiment, a feat only made possible with fs lasers and steep density profiles. Detailed spectral measurements supported the picture with the two generation mechanisms. Although the instability presumably reached saturation, these results could also be explained well with the linear theory. A simple argument was used to show that a longer laser pulse duration leads to a more dominant saturation. Furthermore, it was experimentally shown and explained that the $3\omega_0/2$ can be generated only in an inhomogeneous plasma with scale length of about 1 μm or longer. Therefore the readily observed three-halves harmonic radiation can be exploited as a reliable pre-plasma diagnostic.

In a third series of measurements, the saturation mechanism of the parametric instability was investigated. In particular, the variation of the $3\omega_0/2$ signal on the laser intensity was determined by varying the laser energy or the target focal position. These results indicate two distinct regimes in the development of the signal. The first regime is an exponential growth of the signal with the laser intensity. Above a given intensity the second regime is reached, which exhibits a constant or even decreasing $3\omega_0/2$ signal with increasing laser intensity. The explanation requires a new model for the plasma wave saturation. Careful and detailed pulse duration measurements were performed on the three-halves harmonic radiation. A special autocorrelator was built and tested for these investigations. The results indicate a weak $3\omega_0/2$ pulse duration dependence on the laser pulse duration and an exponential growth. A new model is suggested for the temporal development and saturation of the three-halves harmonic emission in the fs regime that accounts for the measured properties, although further investigation is needed to identify the saturation mechanism.

Bibliography

[1] G. A. Mourou, C. P. J. Barty, and M. D. Perry. *Ultrahigh-intensity lasers: physics of the extreme on a tabletop.* Physics Today p. 22 (1998).

[2] D. Strickland and G. Mourou. *Compression of amplified chirped optical pulses.* Opt. Commun. **56**, 219 (1985).

[3] C. Ziener. *Aufbau eines 12 Terawatt Titan:Saphir-Lasers zur effizienten Erzeugung charakteristischer Röntgenstrahlung.* Ph.D. thesis, Friedrich-Schiller-Universität Jena (2001).

[4] D. Umstadter. *Review of physics and applications of relativistic plasmas driven by ultraintense lasers.* Phys. Plasmas **8**, 1774 (2001).

[5] P. Gibbon and E. Förster. *Short-pulse laser-plasma interactions.* Plasma Phys. Contr. F. **38**, 769 (1996).

[6] E. Esarey, P. Sprangle, J. Krall, and A. Ting. *Overview of plasma-based accelerator concepts.* IEEE Trans. Plasma Sci. **24**, 252 (1996).

[7] T. Tajima and J. M. Dawson. *Laser electron accelerator.* Phys. Rev. Lett. **43**, 267 (1979).

[8] C. Gahn, G. D. Tsakiris, A. Pukhov, J. M. ter Vehn, G. Pretzler, P. Thirolf, D. Habs, and K. J. Witte. *Multi-MeV electron beam generation by direct laser acceleration in high-density plasma channels.* Phys. Rev. Lett. **83**, 4772 (1999).

[9] V. Malka, S. Fritzler, E. Lefebvre, M.-M. Aleonard, F. Burgy, J.-P. Chambaret, J.-F. Chemin, K. Krushelnick, G. Malka, S. P. D. Mangles, Z. Najmudin, M. Pittman, J.-P. Rousseau, J.-N. Scheurer, B. Walton, and A. E. Dangor. *Electron acceleration by a wake field forced by an intense ultrashort laser pulse.* Science **298**, 1596 (2002).

[10] H. Schwoerer, P. Gibbon, S. Düsterer, R. Behrens, C. Ziener, C. Reich, and R. Sauerbrey. *MeV x rays and photoneutrons from femtosecond laser-produced plasmas.* Phys. Rev. Lett. **86**, 2317 (2001).

[11] K. Krushelnick, E. L. Clark, Z. Najmudin, M. Salvati, M. I. K. Santala, M. Tatarakis, A. E. Dangor, V. Malka, D. Neely, R. Allott, and C. Danson. *Mult-MeV ion production from high-intensity laser interactions with underdense plasmas.* Phys. Rev. Lett. **83**, 737 (1999).

[12] A. Pukhov. *Three-dimensional simulations of ion acceleration from a foil irradiated by a short-pulse laser.* Phys. Rev. Lett. **86**, 3562 (2001).

[13] M. Hegelich, S. Karsch, G. Pretzler, D. Habs, K. Witte, W. Guenther, M. Allen, A. Blazevic, J. Fuchs, J. C. Gauthier, M. Geissel, P. Audebert, T. Cowan, and M. Roth. *MeV ion jets from short-pulse-laser interaction with thin foils.* Phys. Rev. Lett. **89**, 085002 (2002).

[14] U. Teubner, G. Pretzler, T. Schlegel, K. Eidmann, E. Förster, and K. Witte. *Anomalies in high-order harmonic generation at relativistic intensities.* Phys. Rev. A **67**, 013816 (2003).

[15] S. Düesterer, H. Schwoerer, W. Ziegler, C. Ziener, and R. Sauerbrey. *Optimization of EUV radiation yield from laser-produced plasma.* Appl. Phys. B **73**, 693 (2001).

[16] S. Düsterer, H. Schwoerer, W. Ziegler, D. Slazmann, and R. Sauerbrey. *Effects of a prepulse on laser-induced EUV radiation conversion efficiency.* Appl. Phys. B **76**, 17 (2003).

[17] T. Feurer, A. Morak, I. Uschmann, C. Ziener, H. Schwoerer, C. Reich, P. Gibbon, E. Förster, R. Sauerbrey, K. Ortner, and C. R. Becker. *Femtosecond silicon kα pulses from laser-produced plasmas.* Phys. Rev. E **65**, 016412 (2001).

[18] F. Ewald, H. Schwoerer, and R. Sauerbrey. *Kα-radiation from relativistic laser-produced plasmas.* Europhys. Lett. **60**, 710 (2002).

[19] J. J. Carroll, D. G. Richmond, T. W. Sinor, K. N. Taylor, C. Hong, J. D. Standifird, C. B. Collins, N. Huxel, P. von Neumann-Cosel, and A. Richter. *Absolute measurement of spatial and spectral characteristics of bremsstrahlung using the photoexcitation of nuclear isomers.* Rev. Sci. Instrum. **64**, 2298 (1993).

[20] H. Schwoerer, F. Ewald, R. Sauerbrey, J. Galy, J. Magill, V. Rondinella, R. Schenkel, and T. Butz. *Fission of actinides using a tabletop laser.* Europhys. Lett. **61**, 47 (2003).

[21] J. M. ter Vehn, S. Atzeni, and R. Ramis. *Inertial confinement fusion.* Europhys. News **29**, 202 (1998).

[22] M. Tabak, J. Hammer, M. E. Glinsky, W. L. Kruer, S. C. Wilks, J. Woodworth, E. M. Campbell, M. D. Perry, and R. J. Mason. *Ignition and high gain with ultrapowerful lasers.* Phys. Plasmas **1**, 1626 (1994).

[23] J. M. ter Vehn, A. Pukhov, and S. Atzeni. *The fast ignitor.* Europhys. News **29**, 219 (1998).

[24] S. Hain and P. Mulser. *Fast ignition without hole boring.* Phys. Rev. Lett. **86**, 1015 (2001).

[25] W. L. Kruer. *The physics of laser plasma interactions* (Addison-Wesley, New York, 1988).

[26] H. A. Baldis, E. M. Campbell, and W. L. Kruer. *Handbook of plasma physics*, vol. 3, chap. 9, p. 397 (Elsevier Science, New York, 1991).

[27] N. A. Ebrahim, H. A. Baldis, C. Joshi, and R. Benesch. *Hot electron generation by the two-plasmon decay instability in the laser-plasma interaction at* $10.6 \ \mu m$. Phys. Rev. Lett. **45**, 1179 (1980).

[28] J. Meyer and Y. Zhu. *Measurement of two plasmon decay instability development in k space of a laser produced plasma and its relation to 3/2-harmonic generation.* Phys. Rev. Lett. **71**, 2915 (1993).

[29] P. E. Young, B. F. Lasinski, W. L. Kruer, E. A. Williams, K. G. Estabrook, E. M. Campbell, R. P. Drake, and H. A. Baldis. *Simultaneous spectrally and spatially resolved measurements of* $3\omega_0/2$ *emission from laser-produced plasmas.* Phys. Rev. Lett. **61**, 2766 (1988).

[30] B. B. Afeyan and E. A. Williams. *A variational approach to parametric instabilities in inhomogeneous plasmas III: Two-plasmon decay.* Phys. Plasmas **4**, 3827 (1997).

[31] D. A. Russell and D. F. DuBois. $\frac{3}{2}\omega_0$ *radiation from the laser-driven two-plasmon decay instability in an inhomogeneous plasma*. Phys. Rev. Lett. **86**, 428 (2001).

[32] C. B. Darrow, C. Coverdale, M. D. Perry, W. B. Mori, C. Clayton, K. Marsh, and C. Joshi. *Strongly coupled stimulated raman backscatter from subpicosecond laser-plasma interactions*. Phys. Rev. Lett. **69**, 442 (1992).

[33] C. Rousseau, G. Malka, J. L. Miquel, F. Amiranoff, S. D. Baton, and P. Mounaix. *Experimental validation of the linear theory of stimulated raman scattering driven by a 500-fs laser pulse in a preformed underdense plasma*. Phys. Rev. Lett. **74**, 4655 (1995).

[34] J. D. Kmetec, C. L. Gordon, III, J. J. Macklin, B. E. Lemoff, G. S. Brown, and S. E. Harris. *MeV x-ray generation with a femtosecond laser*. Phys. Rev. Lett. **68**, 1527 (1992).

[35] K. Sokolowski-Tinten, J. Bialkowski, M. Boing, A. Cavalleri, and D. von der Linde. *Thermal and nonthermal melting of gallium arsenide after femtosecond laser excitation*. Phys. Rev. B **58**, R11805 (1998).

[36] T. Brabec and F. Krausz. *Intense few-cycle laser fields: Frontiers of nonlinear optics*. Rev. Mod. Phys. **72**, 545 (2000).

[37] R. Dendy, ed. *Plasma physics An introductory course* (Cambridge University Press, New York, 1999).

[38] R. J. Goldston and P. H. Rutherford. *Introduction to plasma physics* (Institute of Physics, London, 1995).

[39] L. D. Landau, E. M. Lifshitz, and L. P. Pitaevskii. *Course of theoretical physics: physical kinetics*, vol. X (Pergamon Press, 1981).

[40] D. Bohm and E. P. Gross. *Theory of plasma oscillations. A. Origin of medium-like behaviour*. Phys. Rev. **75**, 1851 (1949).

[41] X. Liu and D. Umstadter. *Competition between ponderomotive and thermal forces in short-scale-length laser plasmas*. Phys. Rev. Lett. **69**, 1935 (1992).

[42] S. C. Wilks, W. L. Kruer, M. Tabak, and A. B. Langdon. *Absorption of ultra-intense laser pulses*. Phys. Rev. Lett. **69**, 1383 (1992).

[43] D. S. Montgomery, R. J. Focia, H. A. Rose, D. A. Russell, J. A. Cobble, J. C. Fernández, and R. P. Johnson. *Observation of stimulated electron-acoustic-wave scattering*. Phys. Rev. Lett. **87**, 155001 (2001).

[44] B. E. A. Saleh and M. C. Teich. *Fundamentals of photonics* (Wiley-Interscience, New York, 1991).

[45] T. Auguste, P. Monot, L.-A. Lompré, G. Mainfray, and C. Manus. *Defocusing effects of a picosecond terawatt laser pulse in an underdense plasma*. Opt. Commun. **89**, 145 (1992).

[46] E. E. Fill. *Focusing limits of ultrashort laser pulses: analytical theory*. J. Opt. Soc. Am. B **11**, 2241 (1994).

[47] G.-Z. Sun, E. Ott, Y. C. Lee, and P. Guzdar. *Self-focusing of short intense pulses in plasmas*. Phys. Fluids **30**, 526 (1987).

[48] S. P. L. Blanc and R. Sauerbrey. *Spectral, temporal, and spatial characteristics of plasma-induced spectral blue shifting and its application to femtosecond pulse measurement.* JOSA B **13**, 72 (1996).

[49] P. Mulser. *Handbook of plasma physics*, vol. 3, chap. 10, p. 435 (Elsevier Science, New York, 1991).

[50] M. Zepf, M. Castro-Colin, D. Chambers, S. G. Preston, J. S. Wark, J. Zhang, C. N. Danson, D. Neely, P. A. Norreys, A. E. Dangor, A. Dyson, P. Lee, A. P. Fews, P. Gibbon, S. Moustaizis, and M. H. Key. *Measurement of the hole boring velocity from doppler shifted harmonic emission from solid targets.* Phys. Plasmas **3**, 3242 (1996).

[51] V. L. Ginzburg. *The propagation of elctromagnetic waves in plasmas* (Pergamon, New York, 1964).

[52] P. Gibbon. *private communication.*

[53] M. Born and E. Wolf. *Principles of optics* (Cambridge University Press, Cambridge, 1999).

[54] F. A. Bibi and J.-P. Matte. *Enhanced electron-ion energy exchange due to a super-gaussian electron velocity distribution function.* Phys. Plas. **10**, 1120 (2003).

[55] L. Chen. *Waves and instabilities in plasmas* (World Scientific, Singapore, 1987).

[56] F. Brunel. *Not-so-resonant, resonant absorption.* Phys. Rev. Lett. **59**, 52 (1987).

[57] P. Gibbon and A. R. Bell. *Collisionless absorption in sharp-edged plasmas.* Phys. Rev. Lett. **68**, 1535 (1992).

[58] H. Ruhl, A. Macchi, P. Mulser, F. Cornolti, and S. Hain. *Collective dynamics and enhancement of absorption in deformed targets.* Phys. Rev. Lett. **82**, 2095 (1999).

[59] A. Pukhov and J. M. ter Vehn. *Laser wake field acceleration: the highly non-linear broken-wave regime.* Appl. Phys. B **74**, 355 (2002).

[60] A. Bergmann and P. Mulser. *Breaking of resonantly excited electron plasma waves.* Phys. Rev. E **47**, 3585 (1993).

[61] P. K. Kaw, W. L. Kruer, C. S. Liu, and K. Nishikawa. *Advances in plasma physics*, vol. 6 (John Wiley & Sons, New York, 1976).

[62] M. V. Goldman. *Parametric plasmon-photon interactions.* Ann. Phys. **38**, 117 (1966).

[63] H. Figueroa, C. Joshi, H. Azechi, N. A. Ebrahim, and K. Estabrook. *Stimulated raman scattering, two-plasmon decay, and hot electron generation from underdense plasmas at 0.35 μm.* Phys. Fluids **27**, 1887 (1984).

[64] F. C. Young, M. J. Herbst, C. K. Manka, S. P. Obenschain, and J. H. Gardner. *Increased hot-electron production at quarter-critical density in long-scale-length laser-plasma interactions.* Phys. Rev. Lett. **54**, 2509 (1985).

[65] C. S. Liu and M. N. Rosenbluth. *Parametric decay of electromagnetic waves into two plasmons and its consequences.* Phys. Fluids **19**, 967 (1976).

[66] B. F. Lasinski and A. B. Langdon. *Linear theory of the $2\omega_{pe}$ instability in inhomogeneous plasmas.* in Laser Program Annual Report, Lawrence Livermore National Laboratory UCRL-50021-77 pp. 4–49 (1977).

[67] A. Simon, R. W. Short, E. A. Williams, and T. Dewandre. *On the inhomogeneous two-plasmon instability.* Phys. Fluids **26**, 3107 (1983).

[68] H. A. Baldis and C. J. Walsh. *Growth and saturation of the two-plasmon decay instability.* Phys. Fluids **26**, 1364 (1983).

[69] H. A. Baldis and C. J. Walsh. *Experimental observations of nonlinear saturation of the two-plasmon decay instability.* Phys. Rev. Lett. **47**, 1658 (1981).

[70] D. R. Dimitrijević and M. S. Jovanović. *Nonlinear features of two-plasmon decay in a long-scale-length plasma.* Phys. Rev. E **66**, 056408 (2002).

[71] A. B. Langdon, B. F. Lasinski, and W. L. Kruer. *Nonlinear saturation and recurrence of the two-plasmon decay instability.* Phys. Rev. Lett. **43**, 133 (1979).

[72] H. A. Baldis, J. C. Samson, and P. B. Corkum. *Two-plasmon decay and profile modification produced by 10.6-μm radiation at quarter-critical density.* Phys. Rev. Lett. **41**, 1719 (1978).

[73] D. W. Phillion, E. M. Campbell, K. G. Estabrook, G. E. Phillips, and F. Ze. *High-energy electron production by the raman and $2\omega_{pe}$ instabilities in a 1.064-μm-laser-produced underdense plasma.* Phys. Rev. Lett. **49**, 1405 (1982).

[74] R. P. Drake, R. E. Turner, B. F. Lasinski, E. A. Williams, K. Estabrook, W. L. Kruer, and E. M. C. T. W. Johnston. *X-ray emission caused by raman scattering in long-scale-length plasmas.* Phys. Rev. A **40**, 3219 (1989).

[75] J. F. Drake, P. K. Kaw, Y. C. Lee, G. Schmidt, C. S. Liu, and M. N. Rosenbluth. *Parametric instabilities of electromagnetic waves in plasmas.* Phys. Fluids **17**, 778 (1974).

[76] D. W. Forslund, J. M. Kindel, and E. L. Lindman. *Theory of stimulated scattering processes in laser-irradiated plasmas.* Phys. Fluids **18**, 1002 (1975).

[77] B. B. Afeyan and E. A. Williams. *A variational approach to parametric instabilities in inhomogeneous plasmas II: Stimulated Raman scattering.* Phys. Plasmas **4**, 3803 (1997).

[78] G. McIntosh, H. Houtman, and J. Meyer. *Measurement of growth rates and temporal behavior of stimulated raman scattering in a CO_2-laser-produced plasma.* Phys. Rev. Lett. **57**, 337 (1986).

[79] B. B. Afeyan and E. A. Williams. *A variational approach to parametric instabilities in inhomogeneous plasmas IV: The mixed polarization high-frequency instability.* Phys. Plasmas **4**, 3845 (1997).

[80] H. C. Barr, P. Mason, and D. M. Parr. *Electron parametric instabilities of relativistically intense laser light in under and overdense plasma.* Phys. Plasmas **7**, 2604 (2000).

[81] B. Quesnel, P. Mora, J. C. Adam, A. Heron, and G. Laval. *Electron parametric instabilities of ultraintense laser pulses propagating in plasmas of arbitrary density.* Phys. Plasmas **4**, 3358 (1997).

[82] J. Meyer and Y. Zhu. *Experimental study of the relation between the absolute-stimulated-raman and two-plasmon-decay instabilities.* Phys. Rev. Lett. **64**, 2651 (1990).

[83] S. D. Baton, C. Rousseaux, P. Mounaix, C. Labaune, B. L. Fontaine, D. Pesme, N. Renard, S. Gary, M. Louis-Jacquet, and H. A. Baldis. *Stimulated brillouin scattering with a 1 ps laser pulse in a preformed underdense plasma.* Phys. Rev. E **49**, R3602 (1994).

[84] A. Giulietti. *private communication.*

[85] P. E. Young, E. A. Williams, and K. G. Estabrook. *Observation of transition to strongly coupled stimulated brillouin scattering in laser-plasma interactions.* Phys. Rev. Lett. **73**, 2051 (1994).

[86] S. J. Karttunen. *Ion fluctuation effects on the two-plasmon decay and stimulated raman scattering.* Phys. Rev. A **23**, 2006 (1981).

[87] J. Meyer. *Mode coupling of the two-plasmon decay instability to ion-acoustic waves and the effect on (3/2)-harmonic emission.* Phys. Fluids B **4**, 2934 (1992).

[88] S. Depierreux, C. Labaune, J. Fuchs, D. Pesme, V. T. Tikhonchuk, and H. A. Baldis. *Langmuir decay instability cascade in laser-plasma experiments.* Phys. Rev. Lett. **89**, 045001 (2002).

[89] K. L. Baker, K. G. Estabrook, R. P. Drake, and B. B. Afeyan. *Alternative mechanism for $\omega_0/2$ emission in laser-produced plasmas.* Phys. Rev. Lett. **86**, 3787 (2001).

[90] A. Hasegawa. *Decay of a plasmon into two electromagnetic waves.* Phys. Rev. Lett. **32**, 817 (1974).

[91] P. D. Carter, S. M. L. Sim, H. C. Barr, and R. G. Evans. *Time-resolved observations of the three-halves harmonic spectrum from laser-produced plasmas.* Phys. Rev. Lett. **44**, 1407 (1980).

[92] V. Aboites, T. P. Hughes, E. McGoldrick, S. M. L. Sim, S. J. Karttunen, and R. G. Evans. *$3\omega_0/2$ harmonic emission from thin foils.* Phys. Fluids **28**, 2555 (1985).

[93] J. Meyer, Y. Zhu, and F. L. Curzon. *Investigation of $(3/2)\omega_0$ emission from an underdense CO_2-laser-irradiated plasma.* Phys. Fluids B **1**, 650 (1989).

[94] H. C. Barr. *Emission at $3\omega_0/2$ through two-plasmon decay.* Tech. Rep. 8.3.3, RAL Report (1979).

[95] H. C. Barr. *Harmonic emission from the quarter critical density surface of laser-produced plasmas.* In M. Q. Tran and R. J. Verbeck, eds., *Proceedings of the 1984 International Conference on Plasma Physics*, p. 641 (Ecole Polytechnique, Lausanne, 1984).

[96] L. V. Powers and R. J. Schroeder. *Time-resolved 3/2 ω_0 spectrum from spherical laser-produced plasmas.* Phys. Rev. A **29**, 2298 (1984).

[97] R. E. Turner, D. W. Phillion, B. F. Lasinski, and E. M. Campbell. *Half- and three-halves harmonic measurements from laser-produced plasmas.* Phys. Fluids **27**, 511 (1984).

[98] W. Seka, B. B. Afeyan, R. Boni, L. M. Goldman, R. W. Short, K. Tanaka, and T. W. Johnston. *Diagnostic value of odd-integer half-harmonic emission from laser-produced plasmas.* Phys. Fluids **28**, 2570 (1985).

[99] D. F. DuBois, D. A. Russell, and H. A. Rose. *Saturation spectra of the two-plasmon decay instability.* Phys. Rev. Lett. **74**, 3983 (1995).

[100] S. Jackel, J. Albritton, and E. Goldman. *Critical-density scale-length measurements in laser-produced plasmas.* Phys. Rev. Lett. **35**, 514 (1975).

[101] S. Jackel, B. Perry, and M. Lubin. *Dynamics of laser-produced plasmas through time-resolved observations of the $2\omega_0$ and $3/2\,\omega_0$ harmonic light emissions.* Phys. Rev. Lett. **37**, 95 (1976).

[102] J. Meyer and H. Houtman. *Measurement of growth rates, saturation, and decay of two-plasmon decay waves in a CO_2-laser-irradiated palsma.* Phys. Rev. Lett. **53**, 1344 (1984).

[103] L. Veisz, W. Theobald, T. Feurer, H. Schillinger, P. Gibbon, R. Sauerbrey, and M. S. Jovanović. *Three-halves harmonic emission from femtosecond laser produced plasmas.* Phys. Plasmas **9**, 3197 (2002).

[104] B. K. Sinha, S. R. Kumbhare, and G. P. Gupta. *Experimental investigation of saturation and convection of two-plasmon decay instability in laser-produced plasmas.* Phys. Rev. A **41**, 3294 (1990).

[105] I. B. Földes, J. S. Bakos, G. Veres, Z. Bakonyi, T. Nagy, and S. Szatmári. *Harmonic generation in a UV laser plasma.* IEEE Journal of Selected Topics in Quantum Electronics **2**, 776 (1996).

[106] K.-U. Amthor. *Plasmadiagnose in Experimenten zur Wechselwirkung intensiver Laserimpulse mit Materie.* Master's thesis, Friedrich-Schiller-University, Jena (2002).

[107] M. Hipp and P. Reiterer. *User manual for IDEA 1.00: Software for interferometrical data evaluation.* http://optics.tu-graz.ac.at Institut für Experimental Physik, Technische Universität Graz (1999).

[108] L. Veisz, W. Theobald, T. Feurer, H. Schwoerer, and R. Sauerbrey. *Three-halves harmonic emission from femtosecond laser produced plasmas with steep density gradients* (2003). Submitted.

[109] C. Ziener, G. Stobrawa, H. Schwoerer, I. Uschmann, and R. Sauerbrey. *Novel device for the generation of controlled prepulses in a ti:sapphire laser amplifier chain.* Rev. Sci. Inst. **71**, 3313 (2000).

[110] I. Uschmann, P. Gibbon, D. Klöpfel, T. Feurer, E. Förster, P. Audebert, J.-P. Geindre, J.-C. Gauthier, A. Rousse, and C. Rischel. *X-ray emission produced by hot electrons from fs-laser produced plasma – diagnostic and application.* Laser Part. Beams **17**, 671 (1999).

[111] O. Peyrusse. *A model for the simulation of nonequilibrium line transfer in laboratory plasmas.* Phys. Fluids B **4**, 2007 (1992).

[112] J. P. Christiansen, D. E. T. F. Ashby, and K. V. Roberts. *MEDUSA a one-dimensional laser fusion code.* Computer Phys. Comm. **7**, 271 (1974).

[113] S. Düsterer. *Laser-plasma interaction in droplet-targets.* Ph.D. thesis, Friedrich-Schiller-University (2002).

[114] C. Reich. *Optimization of femtosecond laser plasma K_α sources.* Ph.D. thesis, Friedrich-Schiller-University (2002).

[115] R. Behrens. *30-Kanal-Spektrometer zur Messung von gepulster Elektronen- und Photonenstrahlung.* Ph.D. thesis, Friedrich-Schiller-Univetsity (2003).

[116] S. Bastiani, P. Audebert, J. P. Geindre, T. Schlegel, J. C. Gauthier, C. Quoix, G. Hamoniaux, G. Grillon, and A. Antonetti. *Hot-electron distribution functions in a subpicosecond laser interaction with solid targets of varying initial gradient scale length.* Phys. Rev. E **60**, 3439 (1999).

[117] A. C. Machacek and J. S. Wark. *A versatile matrix-based solution for the two plasmon decay instability.* Phys. Plasmas **8**, 704 (2001).

[118] A. Tarasevitch and D. von der Linde. *private communication.*

[119] R. Sauerbrey. *Acceleration in femtosecond laser-produced plasmas.* Phys. Plasmas **3**, 4712 (1996).

[120] R. J. Kingham, P. Gibbon, W. Theobald, L. Veisz, and R. Sauerbrey. *Phase modulation of intense ultrashort laser pulses reflected from steep, dense plasmas.* Phys. Rev. Lett. **86**, 810 (2001).

[121] T. Feurer, W. Theobald, R. Sauerbrey, I. Uschmann, D. Altenbernd, U. Teubner, P. Gibbon, E. Förster, G. Malka, and J. L. Miquel. *Onset of diffuse reflectivity and fast electrons flux inhibition in 528-nm-laser-solid interactions at ultrahigh intensity.* Phys. Rev. E **56**, 4608 (1997).

[122] D. T. Attwood, D. W. Sweeney, J. M. Auerbach, and P. H. Y. Lee. *Interferometric conformation of radiation-pressure effects in laser-plasma interactions.* Phys. Rev. Lett. **40**, 184 (1978).

[123] B. K. Sinha. *Observation of two-plasmon decay instability saturation domain in laser-plasma experiments.* Opt. Commun. **73**, 51 (1989).

[124] M. Schnürer, P. V. Nickles, M. P. Kalachnikov, W. Sander, R. Nolte, P. Ambrosi, J. L. Miquel, A. Dulieu, and A. Jolas. *Characteristics of hard x-ray emission from subpicosecond laser-produced plasmas.* J. Appl. Phys. **80**, 5604 (1996).

[125] T. Feurer and R. Sauerbrey. *Characterization of Short Laser Pulses* (Academic Press, 1997).

[126] C. Rulliere. *Femtosecond Laser Pulses* (Springer, 1998).

[127] B. Schmidt, M. Hacker, G. Stobrawa, and T. Feurer. *LAB2 – a virtual femtosecond laser lab.* Http://www.lab2.de.

Zusammenfassung

Lasererzeugte Plasmen, die in der Wechselwirkung von ultrahochintensiven Laserpulsen mit Festkörpertargets entstehen, haben viele Anwendungsgebiete wie Teilchenbeschleunigung, Erzeugung elektromagnetischer Strahlung bei ungewöhnlicher Wellenlänge bis hin zur Trägheitsfusion. Die meisten dieser Anwendungen sind durch parametrische Instabilitäten in Plasmen beeinflusst, deshalb wurden sie mit langen Laserpulsen (> 100 ps) detailliert untersucht. Relevante Instabilitäten sind die stimulierte Raman- / Brillouin-Streuung, wobei die Laserstrahlung in eine Elektronenplasmawelle / ionakustische Welle und in eine gestreute elektromagnetische Welle zerfällt. Der Zwei-Plasmonen-Zerfall, die dritte relevante Instabilität, erzeugt zwei Elektronenplasmawellen – auch Plasmonen genannt. Mit der Einführung der chirped pulse amplification Technik ist es möglich geworden, ultrahochintensive Laserpulse mit Pulsdauer im femtosekunden Bereich zu generieren. Weil die stimulierte Raman-Streuung die Elektronenbeschleunigung in Plasmen beeinflusst, wurde sie in diesem Zeitbereich erneut untersucht. Der Zwei-Plasmonen-Zerfall trat dabei in den Hintergrund, obwohl er in den meisten Experimenten als helles aus dem Plasma austretendes Licht in Erscheinung tritt. Bei der Verwendung eines Titan:Saphir Lasers bei einer Wellenlänge von 800 nm und niedrigeren Intensitäten entsteht in dem Plasma blaues Licht – die zweite Harmonische der Fundamentalen. Dagegen bei höheren Intensitäten wird die Emission grün und bei maximalen Intensitäten wird weißes Licht erzeugt. Diese Strahlung - so wird angenommen - besitzt die 1,5 fache Frequenz der Fundamentalen ($3\,\omega_0/2$) und entsteht durch Plasmainstabilitäten.

In dieser Arbeit wurde erstmalig die $3\,\omega_0/2$ Strahlung, die aus femtosekunden lasererzeugten Plasmen emittiert wird, systematisch untersucht. Das Ziel dieser Arbeit war die Erzeugung, Charakterisierung und Beschreibung der $3\,\omega_0/2$ Strahlung. Weiterhin sollten daraus Informationen über parametrischen Instabilitäten gewonnen werden und mögliche Anwendungen dieser Strahlung gesucht werden. Die Experimente wurden mit dem Jenaer 12 TW Titan:Saphir Laser gemacht, wobei nur eine Leistung von 3 TW benutzt wurde.

In dem ersten Teil der Arbeit wurden Plasmen mit langen Skalenlängen zur Erzeugung von $3\,\omega_0/2$ benutzt. Eine Skalenlänge von ca. 100 μm wurde aus interferometrischen Messungen erhalten. Ionisations-Defokussierung limitierte die Laserintensität im Plasma auf ca. 10^{16} W/cm^2. Spektrale Messungen bewiesen, dass das vom Plasma emittierte sichtbare Licht hauptsächlich aus $3\,\omega_0/2$ Strahlung besteht. Die Energie dieser Emission als Funktion der Laserpulsdauer wurde gemessen. Ein Modell, das den Zwei-Plasmonen-Zerfall und die Kopplung der aus dem Zerfall entstandenen Plasmonen mit den Laserphotonen bein-

haltet, wurde zur Interpretation der Ergebnisse benutzt. Dabei zeigte sich eine sehr gute Übereinstimmung zwischen dem Experiment und dem Modell. Das Modell zeigte, dass sich die Instabilität im linearen Regime befand, d.h. während der Wechselwirkung stieg die Plasmonenamplitude exponentiell an. Bei nanosekunden Laser Experimenten verhält sich die Instabilität ganz anders.

Im zweiten Teil der Arbeit wurde ein weiterentwickelter Laser und Intensitäten bis zu 6×10^{18} W/cm² verwendet. Die Unterdrückung der Vorpulse führte zu deutlich kleineren und kontrollierbaren Skalenlängen zwischen λ und $10\,\lambda$. Um den Erzeugungsmachanismus für die $3\omega_0/2$ Strahlung bei den neuen Laser- und Plasmaparameter identifizieren zu können, wurden winkel- und spektralaufgelöste Messungen durchgeführt. Die Messung ergab zwei Maxima in der Winkelverteilung in einem bestimmten Parameterbereich. Eine detailierte k-Raum Analyse zeigte, dass das erste Maximum in 25° Richtung durch Zwei-Plasmonen-Zerfall erzeugte Plasmonen entsteht, analog zu den früheren Ergebnissen. Für den zweiten Peak in 70° Richtung ist eine Plasmawellenverstärkung basierend auf stimulierte Raman-Streuung verantwortlich. $3\omega_0/2$ Licht wurde zum ersten Mal durch stimulierter Raman-Streuung erzeugt. Dies ist nur mit femtosekunden Laser in steilen Elektronendichteprofilen möglich. Detaillierte spektrale Messungen unterstützen das Modell mit zwei Erzeugungsmechanismen. Eine qualitative Erklärung für die breiten Spektren wurde erhalten. Obwohl Sättigung bei diesem Experiment vermutlich auftrat, lassen sich die Ergebnisse gut mit der linearen Theorie verstehen. Mit einfacher Argumentation wurde gezeigt, dass die Sättigung deutlich dominanter bei nanosekunden als bei femtosekunden Laser ist.

Es wurde experimentell und theoretisch gezeigt, dass $3\omega_0/2$ Strahlung nur in inhomogenen Plasmen mit einer Skalenlänge von ca. $1\,\mu$m oder länger erzeugt werden kann. Aufgrund dieser Eigenschaft kann die $3\omega_0/2$ Emission als eine einfache Plasmadiagnostik benutzt werden.

Im dritten Teil der Arbeit wurde der Sättigungsmechanismus der parametrischen Instabilitäten untersucht. Unter anderen wurde die Abhängigkeit der $3\omega_0/2$ Energie von der Laserintensität bestimmt. Die Intensität wurde durch die Laserenergie und die fokale Position des Targets variiert. Diese Ergebnisse zeigen zwei getrennte Bereiche in der Signalentwicklung. In dem ersten Bereich wächst das Signal exponentiell mit der Intensität an. Ab einer bestimmten Laserintensität (zweiter Bereich) bleibt das Signal konstant oder nimmt sogar ab. Nur unter Verwendung eines neuen Modells können diese Beobachtungen erklärt werden. Genaue und sorgfältige Messungen der Pulsdauer der $3\omega_0/2$ Strahlung wurden durchgeführt. Für diesen Zweck wurde ein spezieller Autokorrelator aufgebaut und gründlich getestet. Die Ergebnisse zeigen eine schwache Abhängigkeit der

$3\,\omega_0/2$ Pulsdauer von der Laserpulsdauer und ein exponentielles Anwachsen der $3\,\omega_0/2$ Energie als Funktion der $3\,\omega_0/2$ Pulsdauer. Ein neues Modell bezüglich der Sättigung, basierend auf den oben genannten Beobachtungen, wurde vorgeschlagen. Mit diesem Modell können die experimentellen Ergebnisse erklärt werden, aber weitere Untersuchungen sind erforderlich, um den Sättigungsmechanismus genauer identifizieren zu können.

Danksagung

Hiermit möchte ich mich bei allen bedanken, die dieser Arbeit ermöglicht haben, insbesondere bei :

- Herrn Prof. Dr. Roland Sauerbrey, meinem Doktorvater, für die vielfältige Unterstützung dieser Arbeit und für viele gute Ratschläge und nützliche Disskussionen

- Prof. Dr. Georg Pretzler und Prof. Dr. Peter Mulser für die Begutachtung dieser Arbeit

- Dr. Thomas Feurer für die Zusammenarbeit und seine unermüdlichen Hilfe, Unterstützung und Freundschaft

- Dr. Helmut Schillinger und Dr. Wolfgang Theobald für die Hilfe und die Anleitung meiner Arbeit

- Dr. Paul Gibbon für die Zusammenarbeit, die vielen fruchtbaren Disskussionen, seine Hilfe mit dem MEDUSA Simulationskode und die Korrektur dieser Arbeit

- Dr. Heinrich Schwoerer für das Leiten der erfolgreichen Laserweiterentwicklung

- Falk Ronneberger, Wolfgang Ziegler und Burgard Beleites für ihre Hilfe bei zahlreichen technischen Problemen und sorgfältige Wartung des Labors

- Dr. Robert Kingham, Dr. Ingo Uschmann und Dr. Oldrich Renner für die erfolgreiche Zusammenarbeit

- Dr. Tamás Rozgonyi für die vielen nützlichen Disskussionen und seine Freundschaft

- Martin Hacker, Gregor Stobrawa, Ralf Netz, Dr. Stefan Düsterer und Andreas Morak für die interessanten wissenschaftlichen Disskussionen

- Kay-Uwe Amthor, Jörg Schreiber, Volker Ulrich, Tibor Wittmann für ihre Hilfe bei den Messungen

- Dr. Stefan Niedermeier, Dr. Christian Ziener und anderen Diplomanden und Doktoranden für die Laserwartung und Weiterentwicklung

- Frau Rauschelbach, Frau Koß, Frau Hein und Frau Triebel, die guten Seelen im Sekreteriat für die lokere und freundliche Atmosphäre

- Meinen Eltern und meiner Schwester für die lange Ausdauer und Unterstützung

Lebenslauf

Persönliche Angaben:

Name	:	László Veisz
Geburtsdatum	:	20. März 1974
Geburtsort	:	Budapest, Ungarn
Adresse	:	Laaer-berg Str. 28 / Stiege II., Wo. 532, 1100 Wien, Österreich
E-mail	:	laszlo.veisz@tuwien.ac.at
Staatsangehörigkeit	:	ungarisch
Familienstand	:	ledig
Zur Zeit angestellt	:	als wissenschaftlicher Mitarbeiter am Institut für Photonik TU Wien, Gusshausstr. 27/387, 1040 Wien, Österreich

Ausbildung und Forschungstätigkeit:

Sept. 1980 - Sept. 1988	:	Grundschule in Budapest
Sept. 1988 - Juni 1992	:	Budai Nagy Antal Gymnasium in Budapest
Juni 1992	:	Abschluß mit Abitur
Sept. 1992 - Juni 1997	:	Studium der Physik an der Loránd Eötvös Universität, Budapest
Juni 1997	:	Abschluß mit Diplom. Thema: Ultrahigh intensity lasers and the interaction of the generated laser pulses with matter
Juli 1996 - Aug. 1996	:	6 Wochen Forschungsarbeit am Institut für Materialphysik Universität Wien; Thema: Investigation of C_{60} crystals with atomic force microscope
Okt. 1996 - März 1997	:	6 Monate Forschungsarbeit am Institut für Optik und Quantenelektronik, PAF, FSU Jena; Thema: Interaction of ultrahigh intensity laser pulses with matter
Febr. 1998 - April 2003	:	Promotionsarbeit am Institut für Optik und Quantenelektronik, PAF, FSU Jena; Thema: Investigation of parametric instabilities in femtosecond laser-produced plasmas
April 2003-	:	angestellt als wissenschaftlicher Mitarbeiter am Institut für Photonik, TU Wien

Jena, den 03. July 2003

Ehrenwörtliche Erklärung

Ich erklre hiermit ehrenwörtlich, daß ich die vorliegende Arbeit selbständig, ohne unzulässige Hilfe Dritter und ohne Benutzung anderer als der angegebenen Hilfsmittel und Literatur angefertigt habe. Die aus anderen Quellen direkt oder indirekt übernommenen Daten und Konzepte sind unter Angabe der Quelle gekennzeichnet.

Weitere Personen waren an der inhaltlich-materiellen Erstellung der vorliegenden Arbeit nicht beteiligt. Insbesondere habe ich hierfür nicht die entgeltliche Hilfe von Vermittlungs- bzw. Beratungsdiensten (Promotionsberater oder andere Personen) in Anspruch genommen. Niemand hat von mir unmittelbar oder mittelbar geldwerte Leistungen für Arbeiten erhalten, die im Zusammenhang mit dem Inhalt der vorgelegten Dissertation stehen.

Die Arbeit wurde bisher weder im In- noch im Ausland in gleicher oder ähnlicher Form einer anderen Prüfungsbehörde vorgelegt.

Die geltende Promotionsordnung der Physikalisch-Astronomischen Fakultät ist mir bekannt.

Ich versichere ehrenwörtlich, daß ich nach bestem Wissen die reine Wahrheit gesagt und nichts verschwiegen habe.

Jena, den 03. July 2003